

NUMERICAL INVESTIGATION OF SURFACE SLIP ON TURBULENCE PROPAGATION
AROUND THE TIP SECTION OF NREL 5MW OFFSHORE WIND TURBINE

by

Emmanuel Quayson-Sackey

Submitted in partial fulfilment of the requirements
for the degree of Master of Applied Science

at

Dalhousie University

Halifax, Nova Scotia

July 2025

Dalhousie University is located in Mi'kma'ki, the
ancestral and unceded territory of the Mi'kmaq.

We are all Treaty people.

© Copyright by Emmanuel Quayson-Sackey, 2025

DEDICATION PAGE

I would like to dedicate this thesis to my father, Alex Quayson-Sackey, my mother, Ekua Amina, and my dear sister, Theodora Quayson. Their constant moral, emotional, and financial support has been invaluable throughout this journey. Their encouragement and inspiration have fueled my perseverance, especially during challenging moments.

TABLE OF CONTENTS

LIST OF TABLES	v
LIST OF FIGURES	vi
ABSTRACT	ix
LIST OF ABBREVIATIONS AND SYMBOLS USED	x
ACKNOWLEDGEMENTS	xiii
CHAPTER 1 INTRODUCTION	1
1.1 Background and motivation.....	1
1.2 Research objectives.....	7
1.3 Thesis Outline	7
CHAPTER 2 LITERATURE REVIEW	9
2.1 Anti-icing and de-icing techniques	9
2.1.1 Passive ice mitigation technique.....	10
2.2 Active ice mitigation techniques.....	28
2.2.1 Thermal ice mitigation technique	28
2.3 Effect of surface slip on flow dynamics	42
2.4 Summary and conclusion of literature	45
CHAPTER 3 METHODOLOGY	47
3.1 Numerical setup	47
3.1.1 Governing equations and numerical algorithm.....	47

3.1.2 Computational domain, grid generation and boundary conditions	49
3.1.3 Numerical settings	51
3.2 Mesh Independence study and Validation	52
CHAPTER 4 RESULTS AND DISCUSSIONS	55
4.1 Instantaneous flow fields	55
4.2 Mean flow field.....	56
4.2.1 Mean flow contours	56
4.2.2 Variation in time-averaged wake velocity characteristics	58
4.3 Power spectral density analysis on the separated shear layer	60
4.4 Proper orthogonal decomposition.....	64
CHAPTER 5 CONCLUSIONS AND FUTURE WORK.....	77
5.1 Recommendations for future studies	78
REFERENCES.....	80
APPENDIX A: AIRFOIL COORDINATES	93
APPENDIX B: SLIP UDF CODE	95

LIST OF TABLES

Table 2.1. Experimental studies on superhydrophobic coated blade surfaces with key parameters useful for comparisons.....	22
Table 2.2: Standard slip lengths obtained from experiments (Zhu et al. (2024))	25
Table 2.3. Summary of numerical techniques used to model superhydrophobic coatings on surfaces with key parameters useful for comparisons.	26
Table 2.4. Summary of literature under electrical resistance anti-icing and de-icing for onshore and offshore wind turbines.	33
Table 2.5. Performance comparison of wind turbines using hot air anti-icing/de-icing.....	36
Table 3.1. Mesh sensitivity analysis	53
Table 4.1. Convergence test.....	66
Table 4.2. Summary of wavelengths for the different cases.....	70

LIST OF FIGURES

Figure 1.1. Schematic diagram of an offshore wind turbine blade during atmospheric icing (Modified from Yang et al. (2022)).	2
Figure 1.2. A schematic of (a) rime, and (b) glaze ice formation.	5
Figure 2.1. The roadmap for anti-icing and de-icing techniques.	9
Figure 2.2. Diagram showing (a) spraying of high temperature chemicals on aircraft wing before takeoff and (b) spraying of high temperature chemicals on an aircraft after landing (Fu et al., 2024).	11
Figure 2.3. Droplet contact angle measurements on surfaces with different treatments.	15
Figure 2.4. Theoretical wetting models (a) Young's state (b) Wenzel's state (c) Cassie-Baxter state.	15
Figure 2.5. Flow over a superhydrophobic coated surface indicating the microscopic slip length (Modified from Park et al. (2021)).	26
Figure 2.6. Schematic diagram illustrating the setup of an electrical resistance utilized for de-icing technique (Modified from Madi et al. (2019)).	31
Figure 2.7. Schematic diagram illustrating (a) the setup of a hot air ice mitigation method (modified from Madi et al. (2019)). (b) Ice formation at the trailing edge caused by runback formation (c) External hot air method (Chi et al., 2024).	37
Figure 2.8. (a) MIDAS-Waveguide integration within CFRP-leading edge section (b) A thermal IR-image of the microwave heated airfoil (Feher et al., 2008).	38
Figure 2.9. Flexible rubber boot de-icing technique (modified from Madi et al. (2019)).	41
Figure 2.10. Schematic diagram of experimental setup showing the simulated ice block, nozzle geometry and water pump (Arhin, 2023).	42
Figure 3.1. Schematic of the NREL 5-MW offshore wind turbine blade showing the distribution of airfoil profiles along the span.	50
Figure 3.2. Schematic diagram of the (a-b) computational domain with their respective boundary conditions and (c) mesh distribution around the airfoil model.	51

Figure 3.3. (a) Distribution of mean pressure coefficient on the upper and lower surface of NACA 64-618 at $\alpha = 0^\circ$ for the four meshes (b-c) Comparison of mean pressure and lift coefficient of the present study with experimental data for no-slip boundary condition..... 54

Figure 4.1. Contours of instantaneous vorticity for (a) no-slip (b) $L_s = 100 \mu\text{m}$ (c) $L_s = 140 \mu\text{m}$ (d) $L_s = 185 \mu\text{m}$ (e) $L_s = 400 \mu\text{m}$ 55

Figure 4.2. Contours of mean streamwise velocities for (a) no-slip (b) $L_s = 100 \mu\text{m}$ (c) $L_s = 140 \mu\text{m}$ (d) $L_s = 185 \mu\text{m}$ (e) $L_s = 400 \mu\text{m}$. The location (green '+' symbol) and magnitudes of peak values are also indicated. 57

Figure 4.3. Velocity profiles downstream the trailing edge of the airfoil for (a) all conditions (b) no-slip (c) $L_s = 100 \mu\text{m}$ (d) $L_s = 140 \mu\text{m}$ (e) $L_s = 185 \mu\text{m}$ (f) $L_s = 400 \mu\text{m}$. The centerline profiles were extracted at $y/c = 0.02$ and spans $x/c \in [0.96, 2.00]$ 60

Figure 4.4. Schematic of probe locations for extracting instantaneous streamwise velocity signals. 61

Figure 4.5. Power spectral density of streamwise instantaneous velocity signal measured along the separated shear layer for the no-slip baseline case at the selected probe locations. 63

Figure 4.6. Comparison of the spectral characteristics of the streamwise instantaneous velocity along the separated shear layer between the no-slip baseline and varying slip conditions at the selected probe locations. 64

Figure 4.7. Fractional mode energy distribution for (a) first 20 modes and (b) cumulative energy distributions for baseline no-slip, $L_s = 100 \mu\text{m}$, $L_s = 140 \mu\text{m}$ and $L_s = 185 \mu\text{m}$, $L_s = 400 \mu\text{m}$ 66

Figure 4.8. Contours of first four POD modes ($\Phi^u_{(j)}$) obtained from the streamwise velocity fluctuations for the baseline no-slip case. 68

Figure 4.9. Contours of first four POD modes ($\Phi_{(j)}$) obtained from the streamwise velocity fluctuations for $L_s = 100 \mu\text{m}$ 68

Figure 4.10. Contours of first four POD modes ($\Phi_{(j)}$) obtained from the streamwise velocity fluctuations for $L_s = 140 \mu\text{m}$ 69

Figure 4.11. Contours of first four POD modes ($\Phi_{(j)}$) obtained from the streamwise velocity fluctuations for $L_s = 185 \mu\text{m}$ 69

Figure 4.12. Contours of first four POD modes ($\Phi_{(j)}$) obtained from the streamwise velocity fluctuations for $L_s = 400 \mu\text{m}$ 70

Figure 4.13. Time series history, frequency spectra and phase portrait of the temporal coefficients $(a_{(j)}(t))$ for baseline no-slip case.....	71
Figure 4.14. Time series history, frequency spectra and phase portrait of the temporal coefficients $(a_{(j)}(t))$ for $L_s = 100 \mu\text{m}$	73
Figure 4.15. Time series history, frequency spectra and phase portrait of the temporal coefficients $(a_{(j)}(t))$ $L_s = 140 \mu\text{m}$	74
Figure 4.16. Time series history, frequency spectra and phase portrait of the temporal coefficients $(a_{(j)}(t))$ $L_s = 185 \mu\text{m}$	75
Figure 4.17. Time series history, frequency spectra and phase portrait of the temporal coefficients $(a_{(j)}(t))$ for $L_s = 400 \mu\text{m}$	76

ABSTRACT

This study investigates the effect of surface slip on the unsteady vortex dynamics around NACA 64-618 (National Advisory Committee for Aeronautics) airfoil using unsteady Reynolds averaged Navier-Stokes simulation. The Reynolds number, based on the chord length and freestream velocity was 1.3×10^6 and at an angle of attack of 12° . A Navier-slip boundary condition, modeled to mimic a superhydrophobic coating, was implemented on the walls of the airfoil to assess its impact on turbulent flow dynamics. Four slip lengths ($L_s = 100 \mu\text{m}$, $L_s = 140 \mu\text{m}$, $L_s = 185 \mu\text{m}$, $L_s = 400 \mu\text{m}$) in addition to the base no-slip condition were examined. The effect of slip on flow characteristics were analyzed using the instantaneous and mean velocity fields. The spatio-temporal dynamics and the interactions between the small-scale Kelvin-Helmholtz vortices and the energetic large-scale von-Karman vortices are examined using frequency spectra and the proper orthogonal decomposition (POD). The results from the slip cases were compared to a baseline no-slip case under identical conditions. The mean flow topology revealed distinct separation bubbles at the trailing edge in the baseline no-slip case. Regardless of the slip length considered, suppression of the separation bubble was observed, resulting in greater acceleration of the flow in the wake region.

Also, instantaneous flow visualization showed that the shear-layer instability was enhanced causing an early vortex roll-up in the wake when the slip was imposed. Frequency analysis conducted along the separated shear layer further revealed the migration of dominant frequencies to lower frequency range especially for $L_s = 400 \mu\text{m}$ indicating the occurrence of small-scale vortex pairing. Based on the results from the POD analysis, it can be concluded that slip significantly increases the turbulent kinetic energy in the wake and concentrates this energy within the identified mode pairs.

LIST OF ABBREVIATIONS AND SYMBOLS USED

Nomenclature

c	Chord length [m]
C_d	Drag coefficient [-]
C_l	Lift coefficient [-]
C_f	Skin friction coefficient [-]
C_p	Pressure coefficient [-]
L_s	Slip length [m]
N	Number of snapshots [-]
Re	Reynolds number [-]
St	Strouhal number [-]
U_s	Slip velocity [m/s]
U_e	Freestream velocity [m/s]
U_{max}	Maximum streamwise mean velocity [m/s]
u	Mean streamwise velocity [m/s]
u'	Streamwise fluctuating velocity [m/s]
y^+	Dimensionless wall distance [-]
t	Time [s]

Greek symbols

α	Angle of attack [°]
κ	Von Karman constant [-]
μ_{air}	Dynamic viscosity of air [Pa/s]
ρ_{air}	Density of air [kg/m ³]
τ_w	Wall shear stress [Pa]
ω_z	Instantaneous spanwise vorticity [s ⁻¹]
λ	Local wavelength [m]
Φ_n	Spatial POD mode [-]

List of Abbreviations

DES	Detached eddy simulation
DNS	Direct numerical simulation
KH	Kelvin-Helmholtz
LBM	Lattice Boltzmann Method
LE	Leading edge
LES	Large eddy simulation
NACA	National Advisory Committee for Aeronautics
NREL	National renewable energy laboratory
RANS	Reynolds averaged Navier-Stokes

OWT	Offshore wind turbine
PIV	Particle image velocimetry
PMMA	Polymethyl methacrylate
POD	Proper orthogonal decomposition
PSD	Power spectral density
RANS	Reynolds Averaged Navier Stokes
SHC	Superhydrophobic coating
SHS	Superhydrophobic surface
TE	Trailing edge
TEM	Transmission electron microscope
UDF	User-defined function
URANS	Unsteady Reynolds Averaged Navier Stokes
WTB	Wind turbine blade

Subscripts

$\Phi_{(j)}$	j -th POD mode
$a_{(j)}$	j -th POD mode coefficient

ACKNOWLEDGEMENTS

I would like to thank the Almighty God for giving me this opportunity to complete this chapter of my life. I would also like to express my sincere gratitude to my supervisor, Professor Baafour Nyantekyi-Kwakye for his continual support, guidance, patience, encouragement and constructive criticism to ensure a distinctive quality work.

I would like to express my gratitude to my examining committee members, Professor Mohammad Saeedi, and Professor Adam Donaldson for their excellent suggestion and comments on my research. I am also grateful for the financial support from Natural Sciences and Engineering Research Council of Canada, Oceans Frontier Institute and Dalhousie University.

Special thanks to my graduate friends, particularly Mohammed Khalid Hossen, Saroj Gautam, Eugene Kankam, Eric and Abiola Akinnibosun for his constructive criticism and reviews. I cannot overlook the support, cooperation and advice of John Vanluxemborg, James McIntosh, Patrick Tabiri, Joseph Ampaw, Dylan Logan, Eric Boudreau and Emmanuel Arhin Jnr.

I appreciate the prayers and support from my sister, Theodora Quayson as well as my parents, Alex Quayson-Sackey and Ekua Amina.

CHAPTER 1 INTRODUCTION

1.1 Background and motivation

Climate change has been a major global concern over the past decade. In the wake of the adverse environmental impacts of burning fossil-based fuels, more attention has shifted to renewable energy resources for energy production (Fronk et al., 2010; Mokhatab, 2007). For this reason, several countries in the Arctic region including Canada, Sweden, Norway, and Denmark, have sought to utilize wind energy technologies as an energy generation source due to the high atmospheric wind potential and air density in those locations (Lamraoui et al., 2014). Wind energy is gradually becoming the most harnessed renewable energy resource. The wind energy sector aims to reach 3 terawatts (TW) of installed capacity by 2030, requiring annual installations to increase from 117 gigawatts (GW) in 2023 to 320 GW (Global Wind Energy Council, 2024). Due to the higher wind speeds and more consistent wind patterns found offshore compared to onshore, there has been a growing focus on developing offshore wind farms these days. According to data released by the International Renewable Energy Agency, the global capacity for offshore wind energy experienced a rapid growth reaching an estimated power output of 63 GW by the end of 2022. This marks nearly 20-times growth since 2010, with both Asia and Europe contributing around half of the total capacity installed today (IRENA, 2023; Press et al., 2024). However, the rapid growth of the global offshore wind energy industry has uncovered several challenges, one of the most prominent being the issue of wind turbine blade (WTB) icing in colder climates. Offshore wind turbine (OWT) blades are highly prone to ice accretion at low temperatures during winter months as shown in Fig. 1.1. Blade ice accretion is one of the major problems that negatively affect the aerodynamic performance thus reducing the power output of OWT in cold climates (Fu & Farzaneh, 2010; Homola et al., 2010; Lamraoui et al., 2014; Yang et al., 2022). In relation to its

effect on aerodynamic performance, ice accretion on OWT blades both changes the shape of the blade and increases the surface roughness. The increased surface roughness distorts the streamlined airflow over the blade surface leading to a flow separation near the leading edge of the blade. This separation, embedded with vortical structures, creates intense turbulence that can stall the wind turbine blade. The turbulence in this context reduces the maximum lift coefficient and more significantly, increases drag coefficient. Additionally, the extra mass from ice accumulation on a blade also increases the inertial force acting on the rotor, potentially changing the blade's natural frequency and load. In extreme cases, this may result in resonance, which could cause damage to the wind turbine and lead to operational accidents (Laakso et al., 2010; Lehtomäki et al., 2016; Sunden & Wu, 2015; Yang et al., 2022).

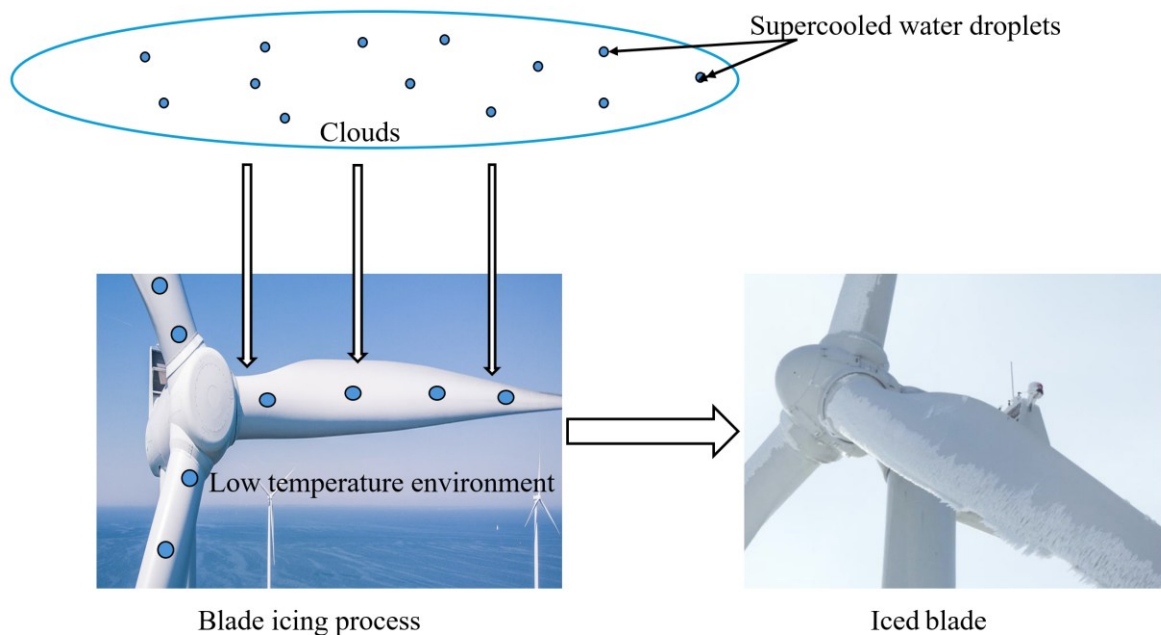


Figure 1.1. Schematic diagram of an OWT blade during atmospheric icing (Modified from Yang et al. (2022)).

These outlined effects of icing on blades stated above are heavily affected by the ice formation type and other environmental factors. Ice forms on turbine blades as a result of surface nucleation, which occurs when supercooled water droplets collide and stick on the walls of the rotating blades in a sub-zero temperature environment (Sunden & Wu, 2015; Yang et al., 2022). Over the years, research on wind turbine icing has identified key factors that promote ice formation, including ambient temperature, wind velocity, mean volume diameter (MVD), liquid water content (LWC), and the geometric size and shape of the blades (Homola et al., 2010; Yang et al., 2022). Unlike onshore wind turbines, icing on OWT occurs under extreme environmental conditions with additional factors at play (Yang et al., 2022). This is because the water droplets which collide with the blades originate mainly from both the condensation of water vapor in the air and from the splashing of salty sea water. This combination increases the LWC offshore as compared to situations experienced onshore. Additionally, the properties of salt content in the water droplets significantly affects freezing point and surface tension, which then alters the freezing process compared to the freshwater droplets encountered onshore (Zhang et al., 2023). The existence of dissolved salts in water droplets lowers its freezing point by disrupting the formation of a solid ice lattice, as the salt solutes interfere with the crystallization process. Also, saltwater droplets exhibit a reduced saturation vapor pressure relative to freshwater droplets due to the Raoult's law effect, further modifying phase change dynamics and enhancing slower ice nucleation. During the freezing process, the non-uniform distribution of solute within the droplet creates localized variations in thermal and solute concentration gradients. When salty water collides with wind turbine blades in offshore conditions, their freezing dynamics as explained above significantly affect uniform ice accretion on their surfaces. The non-ideal freezing conditions may result in heterogeneous ice growth, with regions of high salt concentration

inhibiting freezing and leading to irregular ice structures. These irregularities disrupt the aerodynamic profile of turbine blades, causing increased drag and decreased lift. Additionally, the salt content in freezing saltwater introduces a secondary challenge: corrosion. As ice forms, concentrated brine pockets are left behind due to the exclusion of salts from the forming ice lattice. Over time, these brine pockets can melt or be redistributed across the blade surfaces, depositing corrosive salts onto turbine blades. These deposits promote pitting and material degradation, thereby reducing the structural integrity and lifespan of the turbine.

Based on the various factors that influence icing, blade icing can be divided into different types: precipitation icing and in-cloud icing. Precipitation icing occurs when solid or liquid precipitation such as snow, freezing rain or hail collides with the blade surface and freezes, forming ice. In contrast, in-cloud icing occurs when supercooled water droplets within the clouds rapidly freeze upon contact with the blade's surface in a low-temperature environment (Rindeskär, 2010; Ryerson, 2013) . These icing types have been further classified into different categories: rime, glaze, snow and frost. Rime ice develops when supercooled water droplets within stratus clouds rapidly freeze upon contact with the blade's surface in a low-temperature environment. Rime ice has a wide freezing temperature, which can be as low as $-20\text{ }^{\circ}\text{C}$ and normally forms at the leading edge of the blade without melting (Yang et al., 2022). They are normally opaque and white in appearance, with air trapped inside as shown in Fig. 1.2(a). These ice formations are mostly less dense with smaller LWC and MVD making them more readily removable during de-icing processes (Rindeskär, 2010; Ryerson, 2013) .On the other hand, glaze ice is a hard-transparent type of ice that contains fewer air pockets. It forms when supercooled water droplets inside cumulus clouds freeze on the blade surfaces at ambient temperatures usually between $-6\text{ }^{\circ}\text{C}$ to $0\text{ }^{\circ}\text{C}$ according to data provided by Ryerson (2013) and Yang et al. (2022). The supercooled water

As outlined above, the types of ice that form on surfaces can vary significantly depending on the environmental conditions. As a result, selecting an appropriate strategy to address icing issues is crucial and should be tailored to the specific ice characteristics and the mode of ice accretion as discussed earlier. Understanding these factors is essential for implementing effective mitigation measures that optimize performance and minimize the negative impacts of ice accumulation. Hence, there is a pressing need to develop highly efficient mitigation techniques that are capable of addressing these challenges, reducing the adverse effects of ice formation, and enhancing the reliability and efficiency of systems exposed to icing conditions.

Several ice mitigation techniques, including the use of chemical mixtures, electrothermal heating, and mechanical methods, have been employed on wind turbines. However, these methods are often inefficient and costly. In contrast, superhydrophobic coatings (SHC), a form of passive anti-icing, have emerged as a promising solution. These coatings repel water droplets, reduce drag, and offer self-cleaning properties, making them a more efficient and cost-effective approach to mitigating ice accumulation on wind turbines. While SHC have been applied to various surfaces, their application on wind turbines remains in its early stages. Further research is particularly necessary to better understand the fluid flow dynamics over these coatings, which is essential for fully realizing their potential. Such investigations will provide critical insights into the interactions between the coating surface and the surrounding airflow, enabling the optimization of SHC performance in mitigating ice accumulation under varying operational conditions. This highlights the need for the continued development of highly effective mitigation techniques, like SHC, to address these challenges and improve turbine performance under icing conditions.

1.2 Research objectives

The main objective of this research is to numerically investigate the influence of superhydrophobic coatings on the unsteady flow dynamics, spatiotemporal characteristics of the dominant structures in the wake and aerodynamic characteristics around a 2D NACA 64-618 airfoil which represents the tip section of the NREL 5MW OWT blade. It is important to emphasize that droplet dynamics and ice formation processes are explicitly excluded from the scope of this study. Rather, the focus is to assess the effectiveness of different SHC under non-icing conditions, thereby isolating their flow control potential independent of any phase-change phenomena. The significance of this objective is to inform material selection and surface engineering strategies that enhance the operational efficiency and aerodynamic performance of OWT in cold climates. By characterizing the flow control capabilities of these coatings, the study supports data-driven decisions in coating selection for offshore applications. The following are the specific objectives set for this project:

- (i) Evaluate the flow characteristics around the tip section of NREL 5MW OWT blade in its uncoated condition, serving as a baseline for comparing the effects of different SHC.
- (ii) Examine the influence of varying microscopic slip lengths (L_s) and their influence on wake dynamics.
- (iii) Investigate the spatiotemporal characteristics of dominant wake structures, focusing on how SHC impacts turbulence propagation in the wake.

1.3 Thesis Outline

This thesis is divided into five chapters, which are listed in the following order: introduction, literature review, methodology, results and discussions, and conclusions and future works.

- (i) Chapter 1: Introduction

The need for wind energy especially OWT and their significance in this era of renewable energy is discussed. Challenges they face due to the harsh environmental conditions such as icing is also introduced and explanation as to why preventing ice is discussed. The objectives of this study are presented.

(ii) Chapter 2: Literature Review

This section is divided into two parts. The first part focuses on the various anti-icing and de-icing techniques employed on WTB and other surfaces. This review provides a comprehensive feasibility study, evaluating each ice mitigation technique by examining its fundamental principles, advantages, disadvantages, and the potential for successful integration on OWT blades. The second part of the section focuses on the effects of SHC, the technique chosen for this study. It explores how SHC influences the aerodynamics and flow dynamics around different geometries.

(iii) Chapter 3: Numerical setup and procedure

A detailed description of the model development, grid generation, numerical scheme, validation and data analysis methods are also provided in this chapter.

(iv) Chapter 4: Results and discussion

This chapter presents the analysis of the simulation results. The discussion includes a comparison between the no-slip baseline and various slip cases, highlighting key observations related to vortex shedding, wake dynamics, and unsteady flow behavior.

(v) Chapter 5: Conclusion and future works

The conclusion of this study summarizes all aspects considered in the analysis and highlights potential directions for future research.

CHAPTER 2 LITERATURE REVIEW

This chapter provides a comprehensive review of existing anti-icing and de-icing techniques, outlining their operating principles, advantages, and limitations. The second section critically examines prior studies on the effects SHC on flow dynamics to identify existing knowledge gaps and establish the context for the present research.

2.1 Anti-icing and de-icing techniques

In this section, various icing mitigation techniques proposed for wind turbines operating in cold climates are summarized, compared, and analyzed for further improvement and optimization. This section focuses on both new and established techniques utilized for mitigating ice accretion in wind turbine applications, highlighting areas that require further development and their applicability to OWT. In addressing the challenge of blade icing, the implementation of anti-icing and de-icing systems has played an important role in improving the operational efficiency of OWT in low temperature conditions. Anti-icing technique when implemented prevents ice from forming on the blade surface whereas de-icing technique removes ice layer from a surface that has already been formed. These techniques have been subdivided into two main categories: passive and active anti-icing and de-icing as shown in Fig. 2.1.

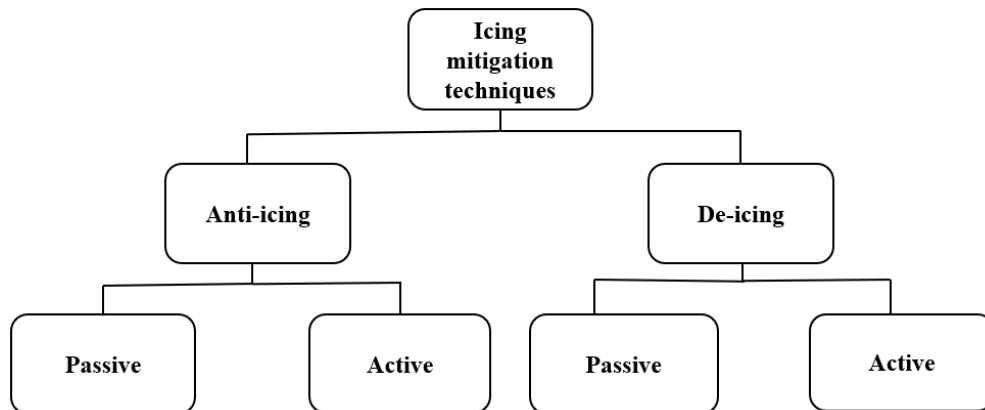


Figure 2.1. The roadmap for anti-icing and de-icing techniques (Quayson-Sackey et al., 2024).

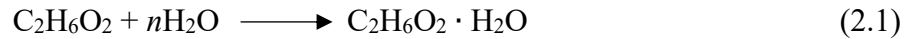
2.1.1 Passive ice mitigation technique

Passive methods take advantage of the physical property of the surface by lowering the ice adhesion strength to prevent ice formation without depending on any source of energy (Dalili et al., 2009; Nine et al., 2023; Wang et al., 2016). The underlying concept of these techniques is to reduce operational costs and prevent blade icing without relying on any specialized energy-consuming mechanism. This method can be used for either anti-icing or de-icing. This section will examine the operational methods and review existing literature on various passive techniques used across different applications and OWTs, as well as their effectiveness for future advancements.

2.1.1.1 Chemical mixtures

Chemical mixtures used for anti-icing are usually produced as anti-freeze solutions. Common antifreeze chemicals such as ethanol, ethylene glycol, and propylene glycol are normally applied on surfaces to prevent ice formation (Jimenez, 2018; Li et al., 2022). These solutions also contain wetting agents, corrosion inhibitors, surfactants, thickeners and other agents that meet specific performance criteria to ensure effective anti-icing (Erdoğan, 2008). Ethanol, for example, is highly miscible with water, which makes it an effective antifreeze agent. It lowers the freezing point of water when mixed by forming hydrogen bonds with water molecules to disrupt the formation of ice crystals. Ethylene glycol ($C_2H_6O_2$) another common antifreeze consists of two hydroxyl (OH) groups attached to a two-carbon chain. This compound is commonly used as a base for automotive antifreeze specifically aircraft anti-icing. When this chemical is mixed with water, it reduces the freezing point of the solution thereby inhibiting ice formation. This disruption increases the amount of energy loss required for the water molecules to arrange themselves into ice. A chemical equation explaining this phenomenon is presented in Eq. (2.1). In aircraft anti-icing systems, ethylene glycol is pumped through weep holes onto the leading edges of the wings,

allowing the chemical to spread across the surface of their wings (Pourbagian & Habashi, 2024). In some cases, these chemicals are often sprayed from a high-pressure jet at a high temperature to either anti-ice or de-ice, as shown in Fig. 2.2 (Fu et al., 2024). Over the years, this process has been accepted and been proven successful in the aerospace industry due to the operational nature of aircrafts.



where n represents the number of water molecules interacting with each ethylene glycol molecule.

In onshore wind turbine applications, these anti-freeze fluids applied on wind turbine blades mixes with the supercooled water droplets to reduce the solution's freezing point and consequently lower the possibility of freezing during the rotation of the blades (Dalili et al., 2009).



Figure 2.2. Diagram showing (a) spraying of high temperature chemicals on aircraft wing before takeoff and (b) spraying of high temperature chemicals on an aircraft after landing (Fu et al., 2024).

This method is categorized as an active anti-icing technique as the use of a pumping system would be required to transport the fluid to the tower's upper section, along with an automatic controller (Fakorede et al., 2016). However, the fluid itself functions as a passive anti-icing

method, demanding no power for blade protection. Nonetheless, these chemicals have some drawbacks (Thomas et al., 1996). They can increase surface roughness, which can adversely affect aerodynamic performance and contribute to environmental pollution. Additionally, the use of these chemicals are only effective for short periods, necessitating frequent replenishment to maintain their protective capabilities (Li et al., 2022). In the case of OWTs, transferring this technology, which has been successfully used in both the aerospace industry and onshore wind turbines presents numerous disadvantages and additional challenges. Due to the unique location and operating conditions of OWTs, a significant portion of these chemicals may be dispersed into the ocean, potentially causing harm to marine life and the surrounding aquatic ecosystem. This environmental concern, combined with the aforementioned drawbacks such as increased surface roughness, limited effectiveness, and the need for frequent replenishment, makes chemical anti-icing a less viable option for OWT applications. The existing literature on this technique highlights that chemical anti-icing applications for wind turbines (onshore and offshore) are generally ineffective under extremely low-temperature conditions (Li et al., 2022).

2.1.1.2 Black paint coating

Black paints, due to their properties absorb all wavelengths of light incident on them. In wind turbine applications, black paint coatings absorb sunlight during daylight and subsequently convert it into thermal energy to warm the surface of the blade above freezing conditions (Maissan, 2001). The generated heat prevents the formation of ice and aids in the melting of ice accreted on the surface of the blade. Due to their high dependence on sunlight for their effectiveness, they are implemented in areas with high solar intensity. After thorough investigations and observations, Laakso et al. (2010), suggested that this method could be suitable for sites where ice formation is not intense. The inconsistent temperature fluctuations (daily and seasonal) associated with black

coatings can subject the blades to thermal cycling which could affect the life span of the wind turbine over extended periods. Overheating of blade surface as a result of high solar absorption can also lead to localized thermal expansion, which will distort the mechanical properties of the composite material used for the OWT blades. However, thermal expansion rate in turbine blades is minimal as it renders it insignificant to affect its mechanical properties. Weis and Maissan (2003) conducted an experiment to compare the root temperatures of a manufacturer's white blade coatings, StaClean white blades and StaClean black blades. It was observed that all three blade coatings showed similar temperature rise during summer and winter depicting an identical solar gain. It was concluded that black coatings do not significantly heat up in windy areas and also overheat in summer periods. As a result of these inconsistencies, black coated blades alone cannot be used to mitigate ice formation when used on OWTs. However, the combination of black paint with superhydrophobic coatings has received numerous attention these days. According to Strobl et al. (2018), black-coated blades combined with ice-phobic coatings can repel water droplets, reduce adhesion strength and delay ice nucleation. Xie et al. (2021) , developed a low cost, high efficiency photothermal superhydrophobic coating by electrodeposition and silanization treatments. The exceptional photothermal performance of the coating, attributed to the black-body properties of carbon materials and its superhydrophobic surface structure, led to an increase in surface temperature up to 90°C. Their findings showed that frozen droplets melted within 100 seconds when exposed to 100 mW/cm² of sunlight. They also conducted a feasibility study on the material's practical application through anti-icing and de-icing experiments on a wind turbine blade, as well as ice/frost melting tests. The results demonstrated superior anti-icing and de-icing properties, attributed to the material's high photothermal conversion and excellent superhydrophobic characteristics. This study highlights the potential of integrating micro-nano

hierarchical structures with solar energy to develop effective photothermal anti-icing materials for real-world use. Therefore, it is imperative for researchers to further explore this area to ensure its adoption for OWT anti-icing application.

2.1.1.3 Superhydrophobic coatings

Inspired by the outstanding water repellent properties of a lotus leaf, extensive research has been conducted to improve superhydrophobic coatings (SHCs) to advance passive anti-icing solutions for OWTs (Latthe et al., 2019; Quéré & Reyssat, 2008; Shirtcliffe et al., 2010; Wang et al., 2016). SHCs, when applied to blade surfaces, effectively prevent accretion by repelling water droplets upon impact, thus ensuring optimal performance of OWT in cold and icy conditions. The SHC achieve this capability through a combination of surface roughness at the nano/microscale level and low surface adhesion strength (Li et al., 2021; Parent & Ilinca, 2011). As a result, water droplets can easily roll off without causing significant wetting to the surface. According to researchers, the wettability on solid surfaces is closely influenced by the surface roughness and water contact angle (Borgioli et al., 2014). As shown in Fig. 2.3, the water droplet contact angle also depends on the surface morphology and surface energy (Oberli et al., 2014). In the case of hydrophilic behavior, surfaces are smooth and exhibit high wettability with a low contact angle ($\theta < 90^\circ$) while hydrophobic surface shows partial wettability with a contact angle ($\theta > 90^\circ$). On the other hand, a superhydrophobic surface also exhibits almost zero wettability with high contact angle ($\theta > 150^\circ$) (Latthe et al., 2019).

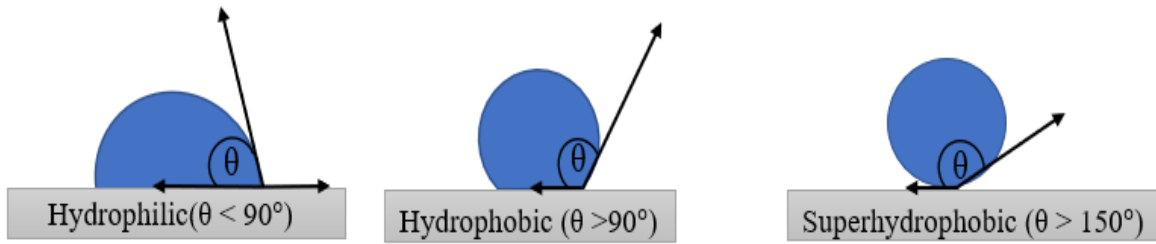


Figure 2.3. Droplet contact angle measurements on surfaces with different treatments.

2.1.1.4 Theoretical Wetting Models and Mechanisms

This section describes the various models used to characterize surface wettability and its influence by surface roughness and surface energy. These models include the Young's model, Wenzel and Cassie-Baxter model.

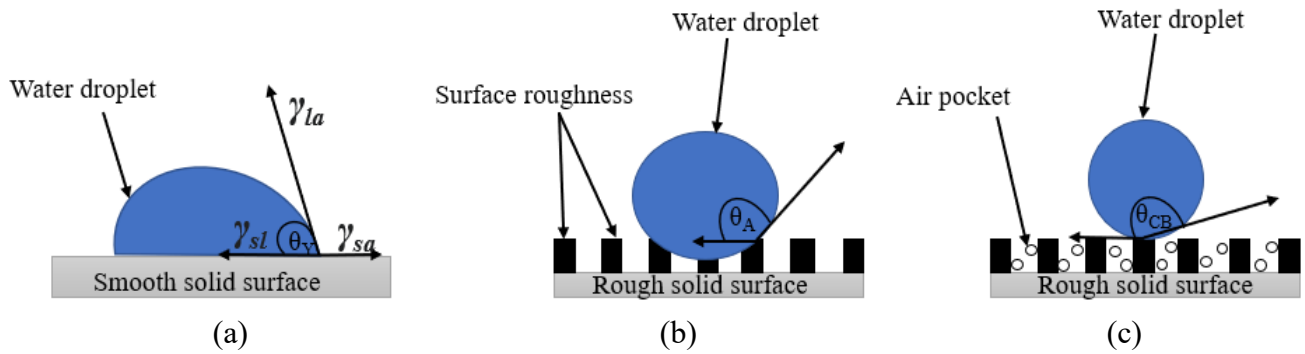


Figure 2.4. Theoretical wetting models (a) Young's state (b) Wenzel's state (c) Cassie-Baxter state.

The Young's equation forms the basis of the wetting process on solid surfaces. This model describes the relationship between water droplet contact angle and interfacial energy (as shown in Fig. 2.4(a)). It is only valid for inelastic, flat, inert, smooth, and chemically homogenous surfaces. According to Young's equation, the contact angle between the liquid and solid surface with relation to interfacial energies is described by Eq. (2.2) (Young, 1805):

$$\gamma_{sa} = \gamma_{sl} + \gamma_{la} \cos \theta_Y \quad (2.2)$$

where θ_Y is the liquid droplet contact angle in ideal state, γ_{sa} is the solid/air interfacial energy, γ_{sl} is the solid/liquid interfacial energy and γ_{la} is the liquid/air interfacial energy.

As the formulation of this equation was based on ideal conditions, it cannot accurately describe real surfaces characterized by non-uniform features. Additionally, the presence of microscopic-level roughness on every surface render Young's equation inadequate for describing wetting processes on real surfaces. Wenzel subsequently deduced an improved model to explain the effect of surface roughness and surface energies on water droplet contact angle (Wenzel, 1936). This model was based on a homogenous wetting regime where water droplets follow the roughness of the surface by permeating into the surface grooves (see Fig. 2.4(b)). The empirical fundamental theory that relates surface roughness and apparent contact angle as presented by Wenzel (1936) is:

$$\cos \theta_A = r \cos \theta_Y \quad (2.3)$$

where θ_A is the apparent contact angle on the rough surface and r is the roughness factor which is defined as the ratio of the actual surface area between the solid and the liquid to the projected surface area. Equation (2.3) clearly describes the effect of surface roughness on different surfaces. It can be deduced that an increase in surface roughness leads to enhanced hydrophobicity while the opposite effect on surface roughness results in increased hydrophilicity with lower contact angles.

While Wenzel's theory is inadequate for describing heterogeneous surface wetting states, Cassie and Baxter introduced a model that clearly explains the behavior of heterogeneous wetting behavior. In Cassie-Baxter's model, air pockets are trapped into the grooves of the micro-nano rough structure, causing the water droplets to suspend their molecules tightly in mid-air without wetting the surface (Cassie & Baxter, 1944) (see Fig. 2.4(c)). This is possible due to the less water

droplet contact area and high contact angle between the solid surface and the water droplets. The Cassie-Baxter equation is shown below (Cassie & Baxter, 1944):

$$\cos \theta_{CB} = \phi(1 + \cos\theta) - 1 \quad (2.4)$$

where θ_{CB} is the apparent contact angle in Cassie Baxter's state (rough surface), θ is the smooth surface contact angle and ϕ is the percentage of solid in contact with the water droplet. As ϕ approaches zero, the contact area between the water droplet and the solid surface decreases resulting in an increase in apparent contact angle (θ_{CB}). This model is normally used to describe superhydrophobic surfaces.

2.1.1.5 Ice mitigation mechanism of superhydrophobic coatings (SHC) in wind turbines

When wind turbine blade surfaces are coated using techniques such as dipping, spraying and etching to become superhydrophobic, they gain properties such as low surface energy, presence of micro-nano particles, drag reduction, and self-cleaning (Kraj & Bibeau, 2010; Nine et al., 2023; Wang et al., 2015). These features enhance the performance of the blades by reducing ice accretion. Although coatings are not capable of keeping the surface completely free of ice, their low installation and operation costs have attracted the focus of researchers in recent years.

Zhu et al. (2020) prepared a mechanochemical robust SHC consisting of polydimethylsiloxane (PDMS) nanoparticles (NPs) and PDMS microparticles (MPs) functional NPs through a combination of thermal treatment and spray treatment. Robust surface roughness produced by the coating showed good qualities for self-cleaning anti-icing applications. Lei et al. (2019) also prepared SiO₂/silicone rubber nanocomposites on a glass substrate by using the simple spray coating method. Water droplet icing behavior and the growth of frost on surfaces at varied surface temperatures were recorded using a common digital camera and a water contact angle meter. Although the coating obtained from this experiment showed surface superhydrophobicity

with a water contact angle of $165.5^\circ \pm 2.7^\circ$ and water sliding angle of $5.3 \pm 2.4^\circ$, its properties could not prevent icing at low temperatures of -12°C and -16°C . The study of Jiang et al. (2018) utilized the photothermal properties of carbon nanotubes (CNTs) to prepare a superhydrophobic SiC/CNTs coating through simple spray coating. Their observations under scanning electron microscope (SEM) revealed that the combination of SiC microstructure and CNTs nanostructure makes the coating surface superhydrophobic and was characterized by a contact angle of 161° and rolling angle of 2° . Due to the high conductivity and photothermal effect of CNTs, the surface temperature of the substrate increased from 30°C to 120°C in 10 s upon near-infrared light irradiation (808 nm) to achieve effective anti-icing and de-icing properties. Additionally, under controlled water condensation conditions, Yin et al. (2011) compared the superhydrophobic behavior of an artificial superhydrophobic surface and a biomimetic lotus leaf surface. Commercial aluminum alloy plates were used to create the artificial superhydrophobic surface. They were spray-coated with epoxy paint, sandblasted with brown emery (60#) under 0.8 MPa pressure, thoroughly cleaned with deionized water in an ultrasonic bath and allowed to dry at room temperature. After the experimental recordings at varied relative humidity (RH), it was observed that an increase in RH above 60% resulted in a gradual decrease in contact angle and increase in rolling angle of the lotus leaf and the artificial superhydrophobic surface. This was due to the condensation of water vapor immersed within the micro-structure causing a transition in the state of water droplets from the Cassie state to the Wenzel state.

To address the issue of water condensation within microstructures and increased frost formation during high humidity conditions, Kim et al. (2012) and Subramanyam et al. (2013) proposed the use of slippery liquid lubricant infused on textured surfaces because of their slip properties. According to the study, infused lubricant into a nanostructured surface chemically

enables the surface to exhibit high affinity to penetrating liquid thereby preventing water condensation and frost formation. From both studies, it was observed that lubricant-infused surfaces decrease ice accretion and adhesion rates contributing to a significant delay in frost formation on the surfaces. Nevertheless, the method employed by the authors mentioned earlier had limitations concerning the gradual reduction of oil on the surface over time. Rykaczewski et al. (2013) suggested the use of liquid reservoirs that allows the replenishment of the lubricant onto the surface to ensure the continuous performance of the surface.

While SHC have proven successful for commercial purposes across various applications such as fouling and corrosion mitigation in heat exchangers, the utilization of these coatings for wind turbine ice mitigation has received limited attention and is currently in the preliminary phase. On superhydrophobic coated wind turbine blade samples, Karmouch and Ross (2010) carried out an experiment to examine water droplet contact angle, contact angle hysteresis (advancing contact angle – receding contact angle), and water droplet sliding angle. Using a spray gun at 40 psi, the SHC was applied to the surface after being prepared by the combination of silica nanoparticles and commercial epoxy paint. The topographical microstructure and the surface roughness of the superhydrophobic surface were observed under SEM (JSM-6300f) and atomic force microscopy (AFM) respectively. Results from the experiment showed that the micro/nanoscale structure of the coating can significantly enhance the water droplet contact angle up to 152° while minimizing contact angle hysteresis to less than 2° . Additionally, the coating facilitated a low sliding angle of approximately 0.5° for water droplets. To build on the work done by Karmouch and Ross (2010), Peng et al. (2012) came up with a simple method for fabricating SHC used in mitigating ice accretion for wind turbine applications. The SHC was prepared by combining a commercial-grade polyvinylidene fluoride (PVDF) with an analytical-grade NH_4HCO_3 powder. The wind turbine

blade samples, coated with PVDF - NH_4HCO_3 were fixed onto the sample stage within a climatic chamber operating at $-10\text{ }^\circ\text{C}$ with a supercooled water sprinkler. The objective of this study was to examine the water droplet contact angle, contact angle hysteresis, and sliding angle under these conditions. Results from their experiment revealed that, water droplet contact angle and sliding angle of the superhydrophobic PVDF coated surface were $156 \pm 1.9^\circ$ and 2° respectively. The superhydrophobic PVDF coating showed excellent anti-icing properties for wind turbine applications.

Most recently, Bao et al. (2021) prepared a ZnO and SiO_2 multi-scale SHC with mechanical flexibility by embedding modified ZnO and SiO_2 nanoparticles in PDMS. The prepared coating showed excellent superhydrophobicity with a higher static water contact angle (153°) and a lower rolling angle (3.3°). The coating was also able to delay ice formation by 1511 s (10.7 times slower than normal freezing time) under conditions of $-10\text{ }^\circ\text{C}$ and 60% RH. Due to the mechanical properties of the SiO_2 and less protrusion distance between the micro-nano particles, the coatings exhibited high mechanical durability after 10 wear tests. Since the preparation process of ZnO and SiO_2 is simple, cost-effective, and adaptable to a variety of substrates, it holds significant potential for applications such as ice mitigation on wind turbine blades. Li et al. (2023) conducted an anti-icing test on a NACA 0018 (airfoil section of a wind turbine blade) to investigate the superhydrophobicity of a coated and an uncoated wind turbine blade surface. This investigation took place in an icing wind tunnel at the Energy Research Laboratory of Northeast Agricultural University. The coating used for this study was biochar/polypyrrole coating obtained through synthesis on the surface of biochar. Surface morphology characterization of this coated surface under SEM showed porous and irregular dents on the surface of the biochar/polypyrrole material. This contributed to the formation of nanostructures depicting excellent superhydrophobicity. The

coated surface was exposed to supercooled water droplets from a sprinkler system with varying MVD and LWC at different wind speed and temperature within the icing tunnel. They measured the water droplet contact angle with an optical contact angle instrument. The static water contact angles were determined to be 151° on biochar/polypyrrole coated surface, 121° on biochar coated surface and 58° on uncoated surface respectively. Ice adhesion strength on these surfaces were also measured. The ice adhesion strength of the uncoated, biochar coated, and biochar/polypyrrole coated surfaces were determined as 184.68 kPa, 105.80 kPa, and 65.03 kPa respectively. The authors concluded that the biochar/polypyrrole coating, characterized by a high contact angle and low ice adhesion strength, indicates a significant capability to reduce ice formation on the blade surface. In extremely harsh icing conditions where blade surface is prone to ice formation, the properties of this coated surface also facilitate easier de-icing, as it requires less external force to remove the ice. To assess the stability of this coating in harsh environments, the authors performed three wear tests. After the test, measurements of the contact angle and ice adhesion strength were taken again to identify any deviations from the initial values. The contact angle of biochar/polypyrrole-coated surface reduced from 151° to 132° signifying a 13.8% reduction rate while the ice adhesion strength and the icing area of the blade surface increased by 5.6% and 9.2% respectively. To confirm the hydrophobicity property of the surface after the wear test, 10 icing tests in the icing tunnel were conducted. Results showed insignificant deviations with initial values before the test due to the robustness nature of the nano/microstructure of the coating.

As shown in Table 2.1, most of the experimental work on SHC for anti-icing has been conducted under controlled conditions with specific humidity, temperature, and icing scenarios. However, OWT are subject to extreme and variable environmental conditions, such as high humidity, saltwater exposure, and severe icing events. The performance of SHC in these marine

environments are not well understood, especially with regards to how salt particles, sea spray, and biofouling might impact the hydrophobicity, surface roughness, and ice adhesion strength over extended periods. Although a lot of research has been done on examining the durability of such surfaces, their ability to maintain their superhydrophobicity in real marine environmental conditions is still a question. A review by Li et al. (2021), suggested the use of suitable binders to improve the mechanical strength of SHC. The authors emphasized the need for further research into binders that would improve adhesion to surfaces, ensuring that the micro-nano particles remain securely attached even under extreme environmental stress. Other aspects that can be investigated to improve their efficiency are the use of phase change materials (PCM) into SHC for OWT applications. The incorporation of PCM can absorb, store, and release thermal energy during phase transitions which makes them ideal for managing temperature fluctuations that might cause mechanical and thermal stresses. Exploring these areas could lead to the development of more durable and effective SHC for OWT.

Table 2.1. Experimental studies on superhydrophobic coated blade surfaces with key parameters useful for comparisons.

References	Coating Preparation technique	Substrate	Type of coating	Surface characterization	Environmental condition	Contact angle	Ice Adhesion strength
Peng et al. (2012)	Simple	WTB	Commercial grade (PVDF) with NH_4HCO_3	SEM	T = -10°C	156 ± 1.9°	---
Karmouch and Ross (2010)	Simple	WTB	Commercial clear silicone resin with	SEM & AFM	---	152°	---
Bao et al. (2021)	Simple	WTB	ZnO and SiO_2	SEM	T = -10°C RH=60%	153°	---

References	Coating Preparation technique	Substrate	Type of coating	Surface characterization	Environmental condition	Contact angle	Ice Adhesion strength
Li et al. (2023)	---	NACA 0018 blade	Biochar/polypyrrole	SEM	T= -20°C	151°	65.03 kPa
Xu et al. (2018)	---	NACA 7715 blade	Silicone-acrylate resin	---	T = -7°C-5°C	156 ± 0.9°	---
Hu et al. (2022)	---	WTB	Fluorocarbon resin and butyl acetate	---	T=-30°C	160.9°	---
Antonini et al. (2011)	Spray and chemical etching	NACA 0021 blade	PMMA & SHS-Teflon	---	T = -17°C	74 ± 1° & 161 ± 2° respectively	---
Lei et al. (2019)	Simple spray	Glass substrate	SiO ₂ /silicone rubber nanocomposites	SEM&TEM	T = -4°C to -16°C	165± 2.7°	---
Ruan et al. (2013)	Electrochemical anodic oxidation & chemical etching	Aluminum alloy plate	FeCl ₃ and HCl as etchants	SEM&AFM	T=-18°C	159.1°	---
Liu et al. (2023)	Hydrothermal & Liquid phase	NACA0018 blade	MoS ₂ /ZnO/PDMS	SEM	T= -10°C	152.1°	78kPa
Du et al. (2023)	Simple spray	Epoxy resin board surface	TiO ₂ /Polyurea	SEM	T= -25°C - 5°C	161.4°	At T=-15°C Sample B= 50.44kPa Sample C= 70.56 kPa Sample D= 75 kPa

Owing to the high costs associated with specialized equipment and materials required for experimental techniques, some researchers have turned to alternative methods such as numerical simulations to model SHC on surfaces. Due to the roughness nanostructure and trapped air in between them, fluid flow on these surfaces exhibits a relative velocity with the surface as illustrated in Fig. 2.5. This surface-flow interaction creates a slippery effect, reducing the skin friction between the fluid and the surface. As applied in numerical simulations, slip condition is normally imposed to mimic surface superhydrophobicity. While it is common to assume zero relative velocity at the surface-fluid flow interfaces for viscous flows, the no-slip condition does not apply when the surface exhibits hydrophobic properties (Rastan et al., 2019). Usually, the Navier's slip boundary condition is mostly applied to simulate the effects of surface superhydrophobicity on the flow field. According to Navier's theory shown in Eq. (2.5), the slip velocity can be related to the strain rate of fluid near the wall and a microscopic parameter called slip length.

$$u_s = L_s \left. \frac{\partial u}{\partial n} \right|_{wall} \quad (2.5)$$

where u_s is the slip velocity, L_s is the slip length and $\frac{\partial u}{\partial n}$ is the wall shear rate. As shown in Fig. 2.5, the slip length is defined as the vertical distance from the solid surface at which the linear extrapolation of the velocity profile tends to zero. For untreated or hydrophilic surfaces, the slip length is typically very small often in the nanometer range making the no-slip condition ($u = 0$) a physically realistic and widely accepted assumption. The slip length value depends on surface roughness and requires experimental determination (Li et al., 2023). Table 2.2 presents the maximum slip lengths obtained from experiments conducted with various materials and surface treatments techniques. In the past decade, numerous numerical research has been conducted to investigate surface slip and superhydrophobicity on both external and internal flows. Table 2.3

provides a summary of the various numerical investigations conducted on superhydrophobic surfaces under both laminar and turbulent conditions available in the literature.

Table 2.2: Standard slip lengths obtained from experiments (Zhu et al. (2024))

References	Experimental methods	Flow conditions	Solid surface	Liquid	Maximum slip length
Byun et al. (2008)	Microchannel	Flowrate 2.4 $\mu\text{L}/\text{min}$	Grooved superhydrophobic PDMS	Deionized water	5.4 μm
Ou et al. (2004)	Microchannel	Laminar flow	Ultrahydrophobic silicon surface	Water	21 μm
Rowin & Ghaemi, (2019)	Channel	$Re = 7000$	Spray coated superhydrophobic surface	Water	96.5 μm
Lee et al. (2008)	Rheometer (Couette flow)	Shear rate 90–130 s^{-1}	Structured silicon coated with Teflon AF solution	Deionized water	93 μm (microposts) 185 μm (microgrates)
Lee & Kim (2009)	Rheometer (Couette flow)	Shear rate 90–130 s^{-1}	Structured silicon treated with 1H, 1H, 2H, 2H-perfluorodecyltrichlorosilane (FDTS)	Deionized water	140 μm (posts) 400 μm (grates)

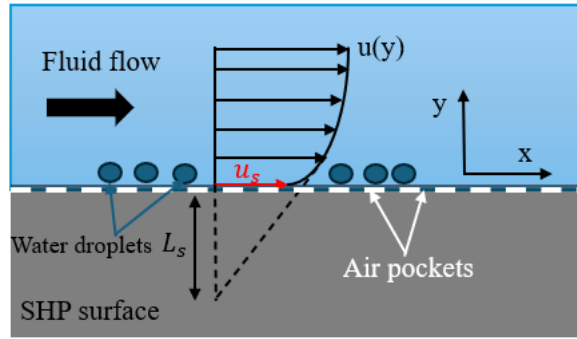


Figure 2.5. Flow over a superhydrophobic coated surface indicating the microscopic slip length (Modified from Park et al. (2021)).

The summary of numerical techniques used to model SHC on surfaces, as outlined in Table 2.3, indicates that most researchers have focused on 2D modeling, including 2D profiles of WTB. While some studies have examined the flow behavior over superhydrophobic surfaces in 2D, the spatio-temporal flow characteristics of coated OWT blades have not been explored in the literature.

Table 2.3. Summary of numerical techniques used to model superhydrophobic coatings on surfaces with key parameters useful for comparisons.

Reference	Flow			Technique	Roughness morphology	Drag reduction
	Type/System	Re_l	Re_t			
Authors	Type/System	Re_l	Re_t	Type	Slip length	Result (%)
Rastan et al. (2019)	NACA 0009	$5,12.5,25 \times 10^6$	---	URANS, SST k- ω model	$L_s = 2, 35$ and $70 \mu m$	47% @ $L_s = 70 \mu m$ & $Re = 5 \times 10^6$
You & Moin, (2007)	Circular Cylinder	300 & 3900	---	DNS & LES	$L_s = 0.02D$, where, $D \sim O(10^2) \mu m$	8% @ $Re = 300$ 27% @ $Re = 3900$
Huang et al. (2018)	Circular Cylinder	60-180	---	Laminar	$L_s = 0.01-0.25$	---
Wang et al. (2018)	NACA 0012	$2,5,10 \times 10^3$	---	LBM	$B = 0.1$	20% @ $Re = 10 \times 10^3$

Reference	Flow			Technique	Roughness morphology	Drag reduction
	Authors	Type/System	Re_l			
Min & Kim, (2004)	Turbulent channel flow	---	180	DNS	$L_s = 0.002, 0.005, 0.01, 0.02$	29%, When L_s was applied in the streamwise direction
Nouri et al. (2013)	Turbulent channel flow	---	180,395,500	LES	$L_s = 2,10 \mu m$	26% @ $L_s = 10 \mu m$ & $Re = 500$
Najafi et al. (2017)	SD7003	$4.5 - 7.5 \times 10^4$	---	---	$L_s = 50 \mu m$	7%
Sotoude Haghghi et al. (2020)	Very low head (VLH) axial hydraulic turbine	---	181.2	SST Turbulence model	$L_s = 50 \mu m$	4% improvement in turbine hydraulic efficiency
Jeffs et al. (2010)	Turbulent micro-channel	$4 \times 10^3 - 10^4$	---	k- ω model	---	Friction factor decreases as apparent slip velocity increases
Gruncell et al. (2013)	Sphere	130	---	Laminar	---	50%
Park et al. (2013)	Turbulent channel flow	---	180,395,590	DNS	Slip length decreased with increase in Re_τ	---
Li et al. (2023)	Mixed flow blood pump	---	---	RNG k- ϵ	$L_s = 0, 10, 20, 50, 100, 200 \mu m$	---
Shahsavari et al. (2023)	SD7003	10^5	---	RANS	$L_s = 0 - 500 \mu m$	---

Reference	Flow			Technique	Roughness morphology	Drag reduction
	Type/System	Re_l	Re_τ			
Authors	Type/System	Re_l	Re_τ	Type	Slip length	Result (%)
Bakhtiari et al. (2023)	SD7037	4×10^4	---	URANS	$L_s = 5, 50, 100, 400 \mu m$	30%
Zhu et al. (2024)	NACA 0012	1×10^6	---	RANS	$L_s = 1 - 500 \mu m$	---

$B = \frac{L_s}{D}$ where B is the relative slip, L_s is the slip length and D is the thickness of the airfoil
 Re_τ : Friction Reynolds number, Re_l : Reynolds number based on the characteristic length

2.2 Active ice mitigation techniques

Active methods normally prevent or remove ice from a surface by using a primary energy source. These techniques are mostly used in the anti-icing or de-icing operations of wind turbines. The current state, application to OWT, and proposed future developments will be examined in this section.

2.2.1 Thermal ice mitigation technique

An alternative approach to prevent or eliminate ice accretion on blade surfaces involves the application of external thermal energy. Active heating strategies for ice removal from wind turbine blades can be further categorized into anti-icing and de-icing. In the case of anti-icing, the blade surface is heated to a temperature above the freezing point of water (0 °C) ensuring that incoming supercooled water droplets do not freeze upon impact. Although this technique can prevent icing on the blade surface, it is cost-ineffective since heat is supplied to the surface throughout the icing event. In contrast, active de-icing strategies are generally used when ice accretion on the blade surface exceeds certain predetermined thresholds, which results in a decrease in power production (Parent & Ilinca, 2011). In this section, a comprehensive review will be conducted to examine the present state-of-the-art working thermal technologies, and their

applications pertaining to OWT. This examination aims to provide a thorough understanding of the existing thermal methodologies used for anti-icing and de-icing.

2.2.1.1 Electrical resistance heating

The electric heating anti-icing and de-icing methods aim to heat the outer surface of wind turbine blades with electric energy to develop a thin layer of water between the blade surface and the accreted ice. This facilitates easy detachment of ice from the surface through the influence of wind, gravity, and centrifugal forces (Battisti et al., 2006). This method is applicable either in anti-icing or de-icing events and consists of electrical heating elements made of metal or carbon fiber material, an energy supply device, and a control system embedded inside the membrane or laminated on the surface (Gao et al., 2021; Petrenko, 2006). To optimize efficiency, multiple heating elements are interconnected in a grid pattern and attached to the leading-edge surface of the blade where icing is predominantly concentrated (Lamraoui et al., 2014; Madi et al., 2019; Parent & Ilinca, 2011) (shown in Fig. 2.6). Given the crucial role of monitoring in this technique, the operational control of the heating system relies significantly on ice detecting devices and the temperature of the blade surface. To prevent fatigue failure due to overheating of the blade, temperature sensors are installed to proactively avert potential damage thereby ensuring the structural integrity and durability of wind turbine blades. As electric heating anti-icing is required to continuously heat the blade surface above the freezing point, more energy is consumed which renders this method not effective for practical applications. In view of that, more attention will be focused on electric resistance de-icing in this section.

In the de-icing mode, the blade surface undergoes intermittent heating, a process that is modulated based on factors such as ice thickness and blade surface temperature. Due to the non-uniform icing rate along the span of the blade, heating elements are mostly segmented into zones distributed from the root to the tip region of the blade (Getz & Palacios, 2021). These partitions

ensure the sufficient power density required by each zone during de-icing to conserve energy. In an event where ice thickness on the blade surface reaches a certain preset threshold as specified by the control system, the heating elements in that zone are triggered and activated. Once initiated, the accreted ice on the surface begins to melt which forms a water film at the interface thereby reducing the ice adhesion strength on the surface for easy removal through aerodynamic shear stress of the wind and gravity (Shu et al., 2017). When this occurs, the control system sends a signal to the heating element to deactivate since parameters such as ice thickness, and blade surface temperature might have reached values below the preset threshold (Sabatier et al., 2016; Shajiee et al., 2013). The time and heat required to de-ice each zone of the blade are controlled and calibrated based on parameters such as blade surface temperature, ice type, ice thickness, thermal properties of the embedded material and the external heat transfer coefficient (Ilinca, 2011; Suke, 2014). This control process of de-icing the blade section by section helps to conserve energy other than de-icing the entire blade simultaneously. In most cases, the tip section and the leading edge of the blade require a high amount of heat to reduce the adhesion strength of ice (Homola et al., 2006). This is because, the tip section of the blade experiences high rates of ice accumulation as a result of its exposure to high relative velocity leading to an increased impact of water droplets on its surface (Shohag et al., 2017). Recently, there have been many research studies focused on exploring the viability of electric resistance de-icing methods (Getz & Palacios, 2021; Li et al., 2024; Mayer et al., 2007; Suke, 2014; Pourbagian & Habashi, 2024). Also, there have been many experimental investigations on the power density required to effectively de-ice the blade surface and specifically identifying critical locations along the blade span that demand a higher heat input for effective de-icing (shown in Table 2.4).

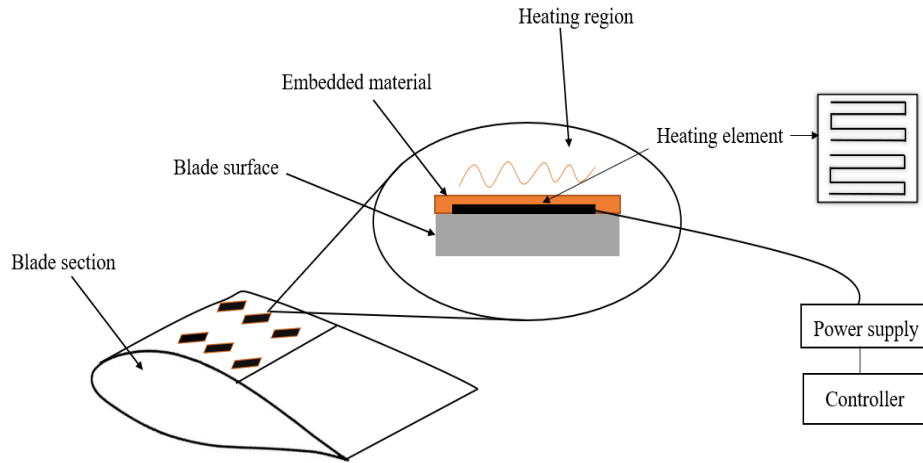


Figure 2.6. Schematic diagram illustrating the setup of an electrical resistance utilized for de-icing technique (Modified from Madi et al. (2019)).

Mayer et al. (2007) conducted an experiment in a refrigerated closed loop wind tunnel test section (0.6 m high, 1.5 m long and 0.5 m wide) to optimize the design and power consumption of an electro-thermal de-icing system for wind turbine blades. The authors considered NACA 63-415 airfoil, a blade cross-section of Vesta 80 1.8 MW turbine as the object under study. Kapton flexible heaters with a wattage density of 10 W/in^2 were installed at the upper and lower outer surfaces of both the leading edge and trailing edge of the blade section. To control the electric power sent to each heating element on the blade, external thermocouples were installed on both the airfoil-heater interfaces and inner surface of the blade section to measure surface temperature. The power consumed and the surface temperature of the system were recorded during different icing conditions (wind velocity and ambient temperatures). Results showed that more heat energy is needed to (a) de-ice the leading edge at the tip rather than the hub, (b) de-ice the trailing edge at the tip rather than the hub, and (c) de-ice the lower surface rather than the upper. They concluded that the power requirement for de-icing increases along the span of the blade taking the hub as a reference. This was due to the increase in relative wind speed, which has an important impact on the airfoil's convective heat transfer. Getz and Palacios (2021) also conducted an experiment on a

scaled partitioned (zone 1, zone 2, zone 3, zone 4) generic 1.5 MW wind turbine blade to investigate the power density required to de-ice the rotor blade section and estimate the minimum ice thickness to overcome ice cohesive forces existing between accreted ice on adjacent board sections or zones of the blade at different icing conditions. The authors reported that 0.385 W/cm^2 of heater power density was required to remove the minimum ice thickness (zone 1: 3.8 mm, zone 2: 4.0 mm, zone 3: 5.0 mm, and zone 4: 7.2 mm) on each zone within a timeframe of 30 seconds. To optimize the efficiency of this technique, they implemented a control system to sequentially activate the heating elements only when the preset minimum ice thicknesses listed above for each respective zone are reached.

To address runback icing on blade surfaces, Li et al. (2024) conducted an experiment in a wind tunnel to investigate the de-icing process on a static heated NACA 0018 blade under various rime icing conditions. Their findings revealed that the total energy consumption during runback water ice melting process decreases as the heat flux increases ultimately resulting in shorter de-icing durations. Although electric resistance de-icing has high thermal efficiency when implemented, they are susceptible to increased blade surface roughness during run-back water effect. This is because, as wind speeds slow down, removing the melted ice through centrifugal and gravity forces becomes difficult consequently leading to refreezing at the trailing edge of the blade. While this process of de-icing has gained popularity in the aerospace industry, there are several research gaps and challenges that need to be addressed for this technique to become more effective, particularly in the context of OWT. One of the primary limitations of electric resistance de-icing is its high energy consumption, especially since the system must intermittently heat the blade surface in response to ice formation. While studies have explored power density requirements, further research is needed to optimize the energy efficiency of this method.

Table 2.4. Summary of literature under electrical resistance anti-icing and de-icing for onshore and offshore wind turbines.

References	Turbine location	Turbine type/Object of study	Method	Heater Area coverage	Time needed to deice (s)
Mayer et al. (2007)	Onshore	Vesta V80/ NACA 63-415	Experiment	LE/TE	---
Getz & Palacios, (2021)	---	Scaled Generic wind turbine/ DU 93-W-210 airfoils	Experiment	Four zones along the span of the blade	30seconds needed to shed minimum ice thickness
Li et al. (2024)	---	NACA 0018	Experiment	Inner region of the hollowed LE	---
Suke (2014)	---	NACA 64(3)-618	Numerical	Outer region of LE	---
LM Wind turbine	Offshore	LM 34.0 P	Prototype (Outside resistive heater)	LE	---
Kelly aerospace	Onshore	KWT 250	Prototype (Outside resistive heater)	LE	---
Siemens	Offshore	SWT-6.0-154	Marketed (Inside resistive heater)	LE	---

One potential solution is to pair OWT with energy storage systems that capture, and store excess energy generated during peak wind hours. This stored energy can then be used to power the de-icing systems when needed. Lithium-ion batteries or more advanced technologies like flow batteries or supercapacitors could be explored to efficiently store energy for long durations and provide quick bursts of power during de-icing. Additionally, developing low-power, high-efficiency heating elements, such as thin-film heaters or graphene-based materials, could

significantly reduce energy consumption. These materials offer excellent thermal conductivity, enabling rapid heating with minimal energy input. Furthermore, advances in electric resistance heating materials, like carbon fiber or metallic elements, could enhance the system's thermal efficiency, allowing turbines to achieve the same de-icing effects while using less power.

2.2.1.2 Hot air heating

For this method, hot air is generated and blown inside the blade through special tubes to prevent or remove ice from its surface (Seifert, 2005). This hot air is transferred from either the root of the blade or the hub to the blade's tip section for even distribution. Once the hot air comes into contact with the blade undersurface, heat is conducted to the ice raising its temperature above melting point. This heat transfer process either causes the accumulated ice on the blade surface to form water film after separating (de-icing) or it acts as a preventive measure inhibiting the formation of ice (anti-icing). The hot air heating system is made up of a blower, heater, and a blade heating control system as shown in Fig. 2.7(a). The hot air generated by the electric heater is transported along the blade by the blower. The blower consists of a centrifugal fan which draws air from the atmosphere at lower temperature and pressure. As a result of the centrifugal action of the rotating fan of the blower and the heat generated by the electric heater due to resistance heating, both the pressure and the temperature of the air increase respectively at its discharge. Normally, the blade's internal domain close to the leading edge is partitioned into two sections. The region closer to the leading edge receives a supply of hot air through convection, as greater heat is required to melt ice at this location, owing to the high intensity of ice formation in that region. After heating the leading edge, the hot air exchanges heat with the cold air from the other duct, heating it to a desired temperature before recirculation through the blower (Ilinca, 2011). Factors that affect the efficiency of this technique are thermal conductivity, wall thickness of the blade material, focusing

on the outer part close to the blade tip rather than the hub portion, the scale size of the blade, and the temperature and volume of hot air (Gantasala et al., 2016; Ilinca, 2011; Li et al., 2019; Suke, 2014). To optimize the performance of this method, a closed system where the working air will be recirculated to the system to reduce power consumption required for heating is recommended compared to an open system. Also, the waste heat produced by the turbine equipment such as the generator, gearbox and the brakes due to frictional and mechanical losses can be used to enhance the system's performance (Xie et al., 2016).

This method has no effect on the environment and is not affected by lightning (Gantasala et al., 2016; Ilinca, 2011). However, this technique may lead to water run-back formation at the trailing edges leading to the formation of ice and subsequently causing blade mass imbalances (shown in Fig. 2.7(b)). This is as a result of low thermal efficiency due to its poor heat distribution along the blade (Madi et al., 2019). Moreover, because the blade tip section requires significant heat transfer and the heating system is located at the hub, there are heat losses during the transfer process rendering it inefficient for large commercial turbines (Ilinca, 2011; Suke, 2014; Xie et al., 2016). Also, due to the high thermal resistance associated with the increased thickness of large turbine blades, more heat energy is needed to be transferred to both the blade surface and the tip (Suke, 2014; Wei et al., 2020). In recent times, modern wind turbine blades are made from fiberglass material which exhibits low thermal conductivity. This property makes it difficult to effectively remove ice by heating the surface from within (Qiu, 2018; Seifert, 2005). This has led to a new research area where scientists investigate hot air technique when applied to the blade externally as shown in Fig. 2.7(c). Chi et al. (2024) investigated a de-icing experimental system on a NACA 0018 iced blade using external hot air method. The authors estimated and analyzed the de-icing time, de-icing area, de-icing rate, and de-icing energy efficiency under various

conditions. Results showed that hot air temperatures and velocities have a significant influence on the de-icing process.

Although this de-icing technique has been commercially applied to onshore wind turbines commercially by manufacturers such as Enercon, Vestas, and Senvion, as shown in Table 2.5, its high energy consumption and the difficulty of implementing this method on modern OWTs still require further research. One promising approach is exploring conducting further studies to optimize the external hot air method, focusing on de-icing efficiency and energy consumption for the blades. Research could investigate how factors such as the size and shape of external air nozzles, temperature of the hot air, standoff distance, and pressure of the hot air affect the distribution and heat transfer to the blade surface. The size and shape of external air nozzles, temperature of hot air, standoff distance and pressure of the hot air influence the distribution and heat transfer to the blade surface. By optimizing these variables, the overall performance of the hot air de-icing system could be significantly enhanced, particularly in harsh offshore environments.

Table 2.5. Performance comparison of wind turbines using hot air anti-icing/de-icing.

Hot air anti-icing/de-icing						
Manufacturer/Turbine model	Protection type	Turbine location	Power rating	Power consumed	Area coverage	Cycle
Enercon/E-82	Anti-icing	Onshore	2.3MW	36.6-86.4kW	All	---
Vestas/V112-3.3MW	De-icing	Onshore	3.3MW	---	1/3 full chord, 2/3 LE of the tip	2hours
Senvion/ MM82	Anti-icing	Onshore	2MW	5 to 20kW	All	---

All: All blade

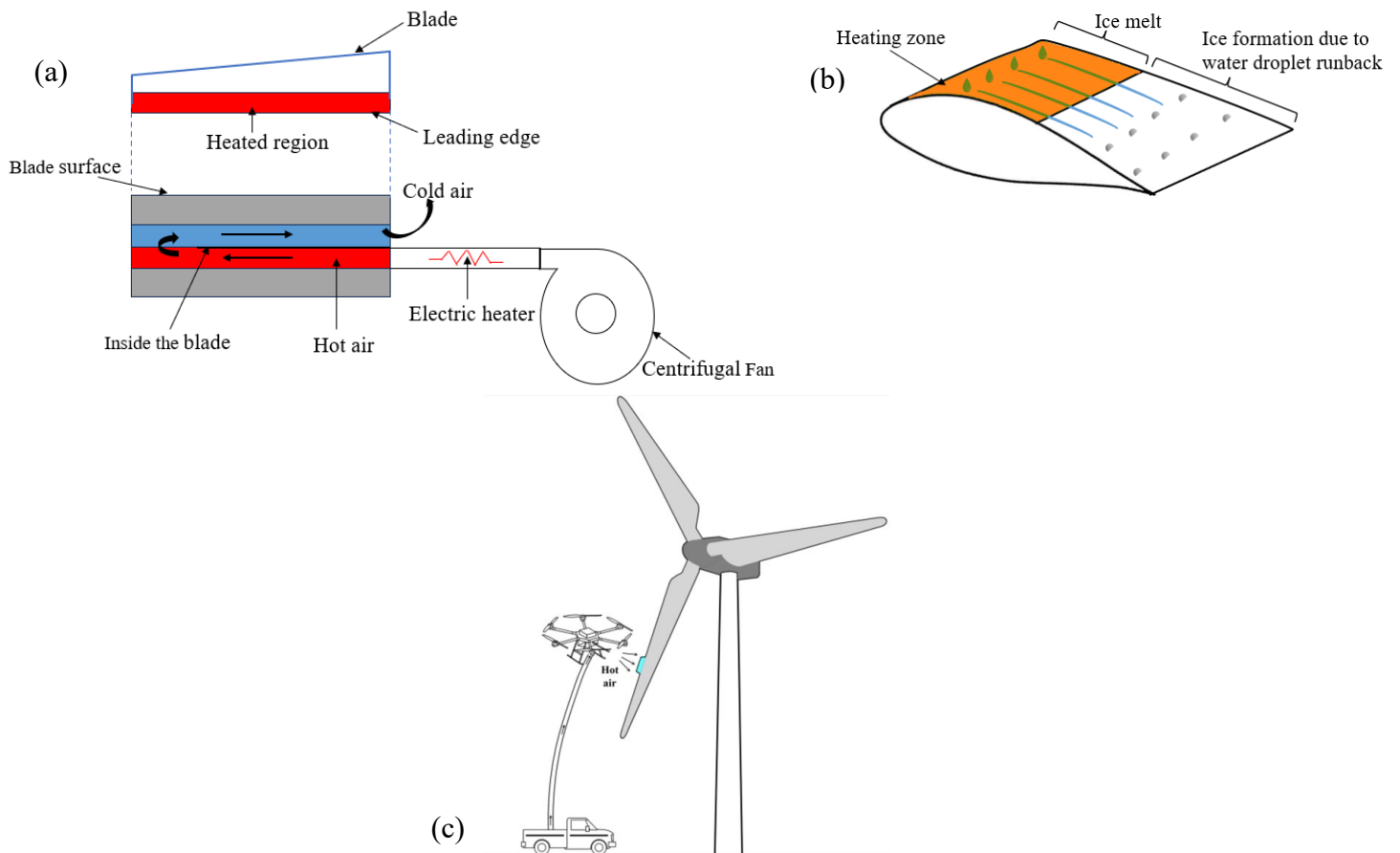


Figure 2.7. Schematic diagram illustrating (a) the setup of a hot air ice mitigation method (modified from Madi et al. (2019)). (b) Ice formation at the trailing edge caused by runback formation (c) External hot air method (Chi et al., 2024).

2.2.1.3 Microwave heating

Ice formation on blade surfaces can also be prevented by using microwave radiation. When supercooled water droplets from the atmosphere collide with blade surfaces, the generated heat from the microwave radiation heats up the droplets reducing the formation on ice (Hansman Jr, 1982; Jasinski et al., 1998). In an event where ice forms on the blade, the heat provided by the microwaves reduces the ice adhesion strength thereby weakening the bonds between the ice structures for easy removal. To enhance effectiveness, the blade surface is normally covered with a dielectric material to increase the reflection of microwave energy on the surface (Ilinca, 2011;

Parent & Ilinca, 2011) . The dielectric material on the surface is purposely designed to generate the necessary amount of thermal energy required to heat up the surface above freezing point (Hansman Jr, 1982) . The effectiveness of this technique mainly depends on the appropriate selection of the microwave frequency and the thickness of the dielectric material above the surface. As applied in the aircraft industry, Feher et al. (2008) in collaboration with Boeing company developed and tested a Microwave De-icing Anti-Icing System (MIDAS) on the leading edge of a 3mm carbon fiber-reinforced plastic airfoil surface (shown in Fig. 2.8). Results showed that the ice accretion on the leading was de-iced within a time frame of 4s at -30°C when the system frequency was operated at 2.45Hz.

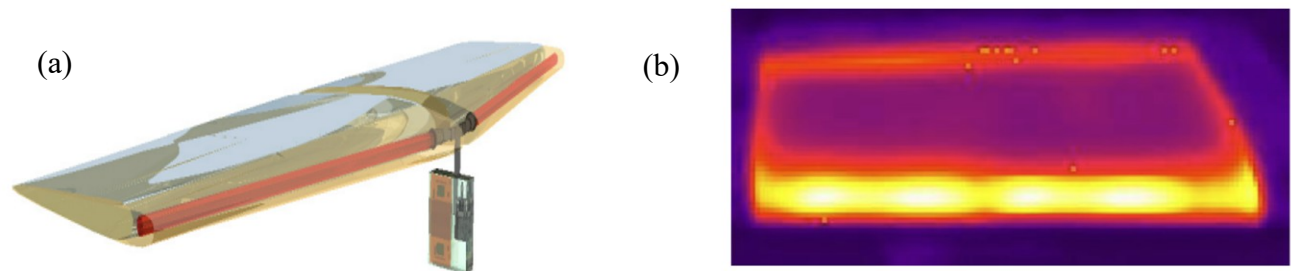


Figure 2.8. (a) MIDAS-Waveguide integration within CFRP-leading edge section (b) A thermal IR-image of the microwave heated airfoil (Feher et al., 2008).

Microwave ice mitigation technique can be more precisely controlled, allowing targeted heating of specific areas susceptible to ice accretion. As a result, energy consumption and the risk of surface overheating is reduced as compared to other thermal heating techniques (Battisti, 2011). In the case of de-icing, the absorption rate of the microwave by the accreted ice is weak leading to the reduction of heat transfer (Madi et al., 2019). To enhance stronger absorption of microwave radiations for de-icing wind turbine blades, Zhang et al. (2018) conducted a numerical simulation on a metamaterial (MA) absorber at 2.46Hz utilizing ANSYS High-frequency and High-speed

Electronics Component Design software. It was found that the MA can effectively absorb the incident microwave and then convert them into heat. Most recently, Dias (2024) investigated the use of microwave energy absorption as an alternative anti-icing solution for wind turbine blades in cold climates. A microwave-absorbing layer embedded in the blade laminate was shown to efficiently convert electromagnetic energy into heat, achieving 98.5% absorption efficiency at 2.45 GHz. Numerical models developed in COMSOL Multiphysics and Engineering Equation Solver demonstrated that the system met power and temperature constraints while minimally increasing the blade mass. The study also identified Eccosorb BSR-1 as the most effective absorber material and optimized system designs using multiple magnetrons spaced 0.5 m apart, emitting 1.5 kW each. Despite its promising results, the study emphasized the need for further research to improve heat distribution, enhance durability, and conduct risk assessments to establish competitiveness with existing anti-icing technologies. Microwave anti-icing techniques are mostly used in the aircraft industry. However, the implementation of this technique on wind turbines is still in its early stages of development. Therefore, more research and optimization are necessary to improve the efficiency of this technique to be considered for OWT applications (Battisti, 2011; Parent & Ilinca, 2011, Dias, 2024) .

Since appropriate selection of microwave frequency is crucial for maximizing the heating effect on the ice and minimizing energy consumption, the optimal frequency for different environmental conditions, such as varying ice thickness, wind speeds, and ambient temperatures needs to be examined. Conducting both experimental and numerical studies would help identify the most effective microwave frequencies for different ice accretion conditions on wind turbine blades. This research could focus on the interaction between ice structure, microwave absorption, and frequency, aiming to determine the most efficient de-icing configuration for OWTs. Also,

investigating the use of advanced metamaterials or surface treatments that can enhance microwave absorption and improve heat transfer to ice could further optimize this technique. Numerical simulations and experimental tests could focus on optimizing metamaterial absorbers for various ice thicknesses and environmental conditions, ensuring a more efficient and effective de-icing process.

2.2.1.4 Mechanical ice mitigation techniques

In this technique, accumulated ice on blade surfaces is removed through mechanical processes. These processes involve in-flight helicopter fluid jet spraying on blades and the use of flexible boots around the surface of the blade. Although some of these processes including the use of flexible boots have not been implemented in wind turbine applications, it remains essential to review them to assess their potential and feasibility for future use. In the case of flexible boots de-icing, tubes filled with compressed air are used on the surface of the blade's leading edge as shown in Fig. 2.9. When accumulated ice reaches a certain threshold (about 6 to 13mm), the tubes are inflated with compressed air to remove the ice from the surface (Ryerson, 2009; Wei et al., 2020). The ice is removed from the surface of the blade through centrifugal action and aerodynamic gravity. Once accumulated ice on the surface is removed, vacuum is created to ensure the tubes are deflated back to their original shape and position (Ryerson, 2009). One advantage of this technique is that less energy is consumed (Ryerson, 2011). However, the installed rubber tubes on the surface may increase the surface roughness and subsequently affect the aerodynamics of the blade by increasing drag force.

Although significant advances have been made with this technique on aircrafts, its application to OWT remains uncertain as a result of several limitations. Due to the flexible nature of OWT blades, the use of pneumatic de-icing systems can cause uneven stress distribution on the

blade's surface during repeated inflation and deflation cycles. This could lead to micro-cracking and wear of the composite layers over time, compromising the structural integrity of the blade,

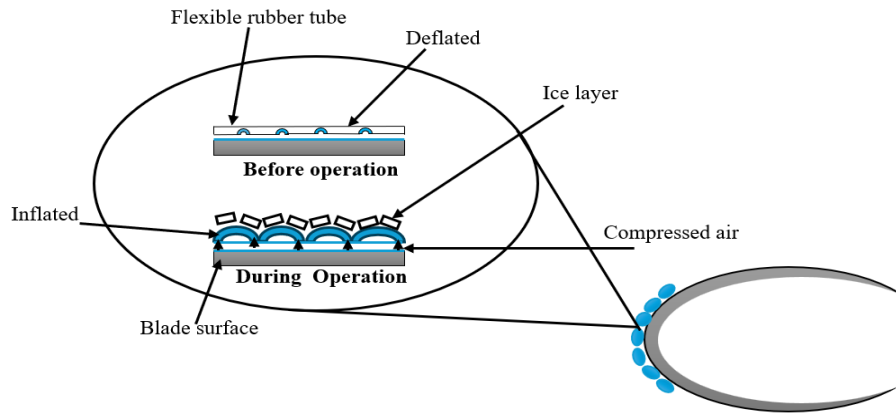


Figure 2.9. Flexible rubber boot de-icing technique (modified from Madi et al. (2019)).

especially in areas near the blade root or near the tips, where the load fluctuations are greatest. Also, pneumatic systems are known to require intensive maintenance, particularly due to perforations or damage that can occur in compressed air tubes as a result of repeated inflation and deflation cycles during their operations. Implementing such systems on OWT would introduce an additional maintenance cost, increasing operational costs and downtime.

Also, the use of helicopters and hot water is another mechanical way of de-icing turbine blades. This process entails evenly spraying hot water onto the blades through nozzles (Hans et al., 2016). The helicopter, equipped with a water tank, pumping systems and hot water ascends to the appropriate height where the blades are located to perform the de-icing. Once hot water gets into contact with the accreted ice, its thermal energy raises the ice's temperature causing it to melt from solid state to liquid. This de-icing approach is particularly useful for offshore wind farms because it allows flexibility in reaching multiple turbines simultaneously. Again, unlike de-icing chemicals, hot water doesn't carry the same risk of corrosion which could harm turbine components over time. As established by Arhin et al. (2024), the effectiveness of de-icing using a high-pressure

water jet depends on the several operational parameters including nozzle geometry, water jet temperature, operating pump pressure and standoff distance. The schematic diagram has been presented in Fig. 2.10. While this investigation was primarily focused on addressing ice accumulation on marine vessels, the principles and methodologies can be extrapolated to the de-icing of OWT blades through the implementation of mechanized and automated systems.

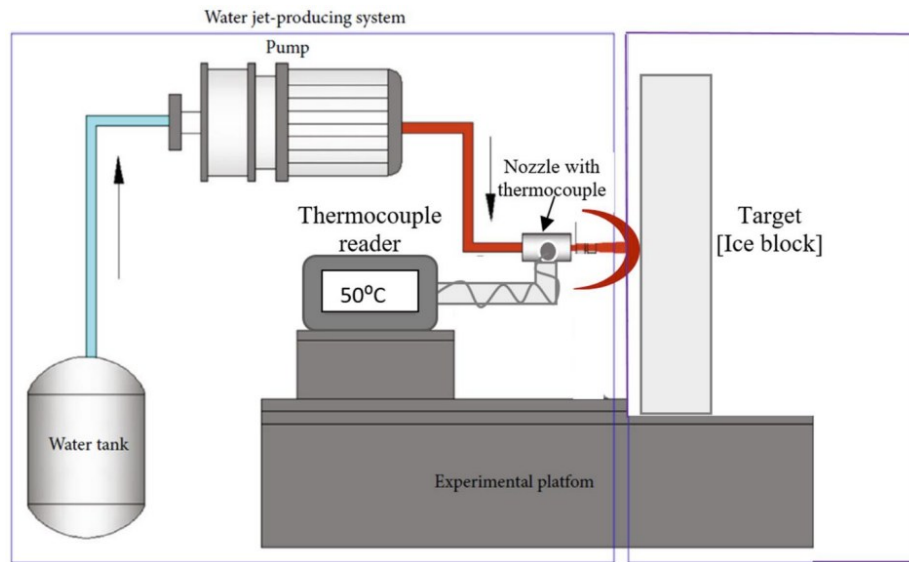


Figure 2.10. Schematic diagram of experimental setup showing the simulated ice block, nozzle geometry and water pump (Arhin, 2023).

2.3 Effect of surface slip on flow dynamics

Over the past few years, several investigations have been conducted on the application of SHC on different surfaces, including flat surfaces, channel walls, bumps, hydrofoils and airfoils. These studies have highlighted the significant effects of SHC on flow dynamics, particularly in relation to the reduction of drag, delay of flow separation, suppression of recirculation bubble and improvement in aerodynamic efficiency. It has been established that the impact of SHC on these surfaces is influenced by several factors, such as Re , α , L_s and surface curvature (C.-H. Choi & Kim, 2006; Daniello et al., 2009; J. Lee et al., 2018; Park et al., 2021). As a result, extensive

experimental and numerical research has been conducted to investigate the effect of SHC on flow dynamics.

Given the importance of these outcomes, extensive experimental and numerical research has been conducted to investigate the impact of SHC on various streamlined surfaces. Lee et al. (2018) conducted an experiment to investigate the effect of SHS on the flow dynamics around a NACA 0012 at low Reynolds numbers ($Re = 0.2-1 \times 10^4$) using particle image velocimetry (PIV). The SHC was developed from nanoparticles and were sprayed on the airfoils to yield different SHS. They observed that the influence of these surfaces on flow dynamics exhibited strong dependence on Re and angle of attack (α). For instance, the coated surface had minimal impact at very low angles of attack ($0^\circ \geq \alpha \leq 2^\circ$) or very high angles ($\alpha \geq 20^\circ$). However, at intermediate angles ($2 > \alpha \leq 10^\circ$), enhanced turbulence over the superhydrophobic surface intensified shear-layer instability, leading to early vortex rollup and shorter vortex formation lengths in the wake. Interestingly, within the transitional range of angles, the effect reverses, slightly delaying vortex rollup in the wake. Sooraj et al. (2019) conducted a PIV experiment to investigate the effect of SHC on a NACA 0015 hydrofoil over a Re range of 6500 – 30,800 at five α ($0^\circ-20^\circ$). Their results revealed a 40% drag reduction, delayed flow separation and reduced vortex strength at $\alpha = 15^\circ$ when a superhydrophobic coated surface was used at $Re = 30,800$ compared to a bare acrylic surface. Sooraj et al. (2020) also investigated the influence of SHS on the wake dynamics around a circular cylinder using PIV. Their results depicted that the onset of vortex shedding was delayed, while early rolling-up of vortices were accelerated, resulting in reduced recirculation lengths in unsteady regimes. Also, the velocity deficit experienced by the superhydrophobic cylinder wake was comparatively less and the effect was more profound in the Re range 300 – 860. Using proper orthogonal decomposition (POD) to examine the wake coherent structures, a larger number of

coherent structures and change in vortex shedding pattern to primary and secondary vortices were observed in the near wake of the superhydrophobic cylinder. Similar PIV results were reported by Kim et al. (2015). Choi et al. (2019) experimentally investigated flow structures generated by a rotor with superhydrophobic coating applied on the blade surface in static water at low $Re = 96000$. Hydrophobic nanoparticles were sprayed to produce a superhydrophobic surface. It was observed that, the SHC can induce 20% reduction in wake turbulent kinetic energy and 6% decrease in streamwise momentum flux and that the superhydrophobic coating applied on the pressure side of the rotor is more effective than that on the suction side in terms of turbulence reduction.

As can be seen from the literature, a wide range of experimental studies has been conducted to investigate drag reduction, vortex propagation, and turbulent structures around SHS. These experiments, often performed on scaled-down models, offer high-fidelity data; however, their applicability to full-scale configurations may be limited due to geometric simplifications and flow scaling effects. To complement these insights, several numerical studies have been undertaken to provide comprehensive understanding of the flow characteristics and vortex dynamics around SHS on more realistic models. You and Moin (2007) numerically studied the effects of hydrophobic surfaces on the drag and lift of a circular cylinder using direct numerical simulation (DNS) and large-eddy simulations (LES) at Re of 300 and 3900 respectively. They observed a reduction in both the mean drag and the root-mean-square lift coefficient values. Also, the drag reduction in the laminar vortex shedding regime was primarily attributed to a decrease in skin friction, whereas in the shear layer transition regime, the reduction was mainly due to a delay in flow separation. Furthermore, Legendre et al. (2009) examined the influence of slip boundary condition on the wake dynamics of a two-dimensional (2D) flow past a circular cylinder. The results showed that

slip significantly delayed the onset of wake recirculation and vortex shedding behind the cylinder. There was also a reduced drag on the cylinder, with drag sensitivity increasing at higher Re . Additionally, Rastan et al. (2019) investigated the effect of streamwise slip on drag force and vortex structures around a symmetrical coated hydrofoil using unsteady Reynolds-Averaged Navier-Stokes (URANS). The results revealed that an increase in L_s enhances the reduction rates of both frictional and pressure drag. Furthermore, a higher L_s was found to increase the amplitude of force fluctuations and the vortex shedding frequency. More recently, Zhu et al. (2024) extensively studied the effects of surface slip on the hydrodynamics around a 2D NACA 0012 using URANS. Three slip positions (both surfaces, upper surface, and lower surface) and eight L_s (1 – 500 μm) were examined at α from 0° to 10° and a $Re = 1.0 \times 10^6$. Their findings revealed that surface slip on both surfaces or the upper surface increased lift and reduced drag by delaying flow transition, suppressing the laminar separation bubble, and delaying flow separation. In contrast, the presence of slip on the lower surface led to an increase in total drag.

2.4 Summary and conclusion of literature

This literature review provides a comprehensive overview of previous research on anti-icing and de-icing techniques, with a specific focus on their operational mechanisms, advantages, disadvantages, and feasibility for offshore wind applications. A thorough analysis of the various methods highlighted the effectiveness of different anti-icing and de-icing strategies, considering their environmental impact, energy consumption, and maintenance requirements.

Among the techniques discussed, SHC for anti-icing emerged as a promising solution due to their numerous advantages. These include their ability to significantly reduce ice adhesion, improve surface water repellency, and enhance self-cleaning properties, making them particularly suitable for the harsh and variable conditions encountered in offshore wind environments.

Researchers have developed SHC of many configurations and have varied operating parameters on different conditions in order to get a better understanding of how the implementation of this method could be optimized. Although extensive research has been conducted to explore the effects of superhydrophobicity on hydrofoils and symmetric airfoils, their unsteady effects on asymmetric airfoils particularly those in offshore wind applications have not been extensively investigated and fully understood. This gap in understanding arises from the complex interactions between flow phenomena, such as flow separation, vortex shedding, and changes in aerodynamic characteristics, which can vary significantly with changes in variation in Re , α , L_s and surface curvature of the airfoil. Besides these phenomena, it is of great importance to examine how surface slip influences both the near-wake and far-wake structures, especially in scenarios where wake impingement may occur, such as wind farms. To address this gap, the present numerical study aims to investigate the influence of surface slip on the unsteady flow dynamics, spectra behaviour of vortices, spatiotemporal characteristics of the dominant structures in the wake and aerodynamic characteristics around a 2D NACA 64-618 airfoil which represents the tip section of the NREL 5MW offshore wind turbine blade.

CHAPTER 3 METHODOLOGY

3.1 Numerical setup

3.1.1 Governing equations and numerical algorithm

The incompressible viscous flow around the 2D NACA 64-618 airfoil was simulated using the finite volume method to discretize and solve the Reynolds-averaged Navier–Stokes (RANS) equations. The governing equations for the mass and momentum conservation are written as:

$$\frac{\partial \bar{u}_i}{\partial x_j} = 0 \quad (3.1)$$

$$\frac{\partial}{\partial t} (\bar{u}_i) + \bar{u}_j \frac{\partial \bar{u}_i}{\partial x_j} = -\frac{1}{\rho} \frac{\partial \bar{p}}{\partial x_i} + \frac{\partial}{\partial x_j} \left(\nu \frac{\partial \bar{u}_i}{\partial x_j} - \overline{u'_i u'_j} \right) \quad (3.2)$$

where \bar{u}_i and \bar{p} are the mean velocity and pressure, respectively. Also, ρ and ν are respectively the density and kinematic viscosity of the fluid and $\overline{u'_i u'_j}$ is the Reynolds stress tensor. In order to close the set of RANS equations, the shear stress transport (SST) $k - \omega$ model was used to model the Reynolds stress tensor and close the system of governing equations. The SST $k - \omega$ model (Eqs. (3.3) and (3.4)) is a two-equation turbulent model developed by combining the $k - \varepsilon$ and the $k - \omega$ models using a blending function (Menter, 1993). It employs the $k - \omega$ near solid walls for improved accuracy in the boundary layer, and switches to the $k - \varepsilon$ in the free stream regions. This hybrid model was adopted considering its wide utilization and acceptance as one of the most commonly used turbulence models for engineering applications for complex flows with adverse pressure gradients and boundary layer separation (Zhu et al., 2024).

$$\frac{\partial(k)}{\partial t} + \bar{u}_j \frac{\partial(k)}{\partial x_j} = P_k - \beta^* k \omega + \frac{\partial}{\partial x_j} \left[(v + \sigma_k v_t) \frac{\partial k}{\partial x_j} \right] \quad (3.3)$$

$$\frac{\partial(\omega)}{\partial t} + \bar{u}_j \frac{\partial(\omega)}{\partial x_j} = \frac{\gamma}{v_t} P - \beta \omega^2 + \frac{\partial}{\partial x_j} \left[(v + \sigma_\omega v_t) \frac{\partial \omega}{\partial x_j} \right] + 2(1 - F_1) \sigma_{\omega 2} \frac{1}{\omega} \frac{\partial k}{\partial x_i} \frac{\partial \omega}{\partial x_i} \quad (3.4)$$

where \bar{u} , k , ω , v , v_t represent the mean velocity, turbulent kinetic energy, specific dissipation rate, kinematic viscosity and turbulent eddy viscosity, respectively. The production term for turbulent kinetic energy is given by $P_k = 2v_t S_{ij} S_{ij}$ where the mean strain-rate tensor (S_{ij}) is defined as:

$$S_{ij} = \frac{1}{2} \left(\frac{\partial \bar{u}_i}{\partial x_j} + \frac{\partial \bar{u}_j}{\partial x_i} \right) \quad (3.5)$$

The turbulent eddy viscosity is computed as:

$$v_t = \frac{a_1 k}{\max(a_1 \omega, \Omega F_2)} \quad (3.6)$$

where Ω is the absolute value of the vorticity, a_1 is a model constant and F_2 is the eddy viscosity blending function which is expressed as:

$$F_2 = \tanh \left(\left[\max \left(\frac{2\sqrt{k}}{\beta^* \omega d}, \frac{500v}{d^2 \omega} \right) \right]^2 \right) \quad (3.7)$$

To accurately capture near-wall effects and enhance prediction in separated flows as well as in the freestream region, the SST $k - \omega$ turbulence model employs the blending function (F_1) as shown in Eq. (3.8). This function activates the $k - \omega$ model near solid boundaries, where it accurately

resolves the viscous sublayer, while enabling a smooth transition to the $k - \varepsilon$ model away from the wall.

$$F_1 = \tanh \left(\left(\min \left[\max \left(\frac{\sqrt{k}}{\beta^* \omega d}, \frac{500\nu}{d^2 \omega} \right), \frac{4\sigma_{\omega 2} k}{CD_{k\omega} d^2} \right] \right)^4 \right) \quad (3.8)$$

$$CD_{k\omega} = \max \left(2\rho\sigma_{\omega 2} \frac{1}{\omega} \frac{\partial k}{\partial x_j} \frac{\partial \omega}{\partial x_j}, 10^{-20} \right) \quad (3.9)$$

where d represents the distance to the closest wall and $CD_{k\omega}$ is the positive portion of the cross-diffusion term. The model constants β , σ_k , σ_ω are computed by a blend from the corresponding constants using:

$$\phi = \phi_1 F_1 + \phi_2 (1 - F_1) \quad (3.10)$$

where ϕ denotes model constant and subscripts 1 and 2 correspond to the $k - \omega$ and $k - \varepsilon$ values, respectively.

3.1.2 Computational domain, grid generation and boundary conditions

The present investigation utilized the NACA 64-618 airfoil which is typically located at the tip section of NREL 5MW baseline OWT blade (see Fig. 3.1) (Jonkman, 2009). This is a 6-series airfoil with maximum thickness of 17.9% located at 34.7% of the chord from the leading edge and a maximum camber of 3.3% at 50% of the chord. The considered airfoil has a chord length, $c = 1$ m located at the center of the computational domain. The domain extends $10c$ from the upstream of the airfoil leading edge, $22c$ downstream from the leading edge and spans $\pm 10c$ in the wall normal direction as shown in Fig. 3.2(a-b). This flow domain was used for the simulation to accurately capture wake dynamics, vortex shedding and prevent flow reversal at the outlet.

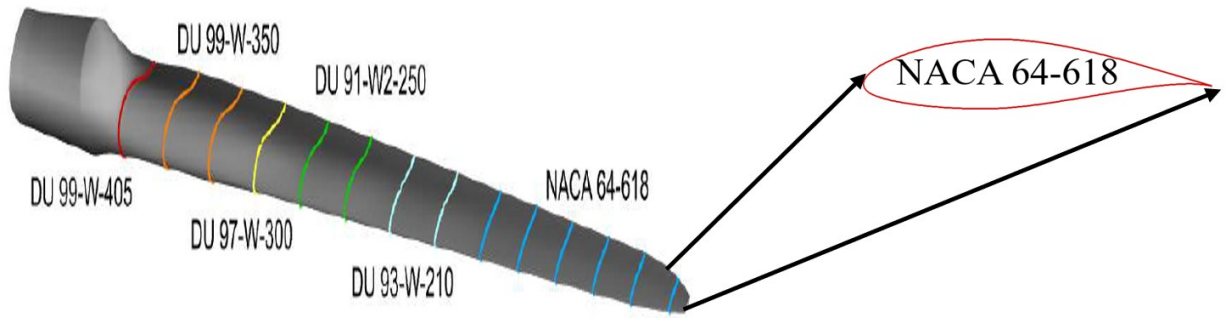


Figure 3.1. Schematic of the NREL 5-MW offshore wind turbine blade showing the distribution of airfoil profiles along the span.

The domain was discretized using a fully structured *C*-type mesh around the airfoil as illustrated in Fig. 3.2(c). To capture regions with high velocity gradients and strong shear forces on the wall of the airfoil, the first node was placed 0.002 mm. A cell growth ratio of 1.2 was applied in the wall-normal direction to ensure a smooth transition through the boundary layer. Automatic wall treatment was employed to handle near-wall boundary layer modeling, allowing accurate resolution based on the local mesh resolution. The mesh quality was evaluated for skewness and orthogonality with all values within acceptable limits to ensure a well-conditioned grid for accurate simulation results. The maximum skewness recorded was 0.7, and the orthogonality quality was 0.8, both of which are considered well within acceptable ranges for reliable and stable simulation.

Air at 15 °C with density of $\rho_{\text{air}} = 1.225 \text{ kgm}^{-3}$ and constant dynamic viscosity of $\mu_{\text{air}} = 1.789 \times 10^{-5} \text{ Pa/s}$ was used as a working fluid for the simulation. In terms of boundary conditions, a Dirichlet boundary condition prescribing a uniform velocity, $U_e = 20 \text{ m/s}$ was applied at the inlet, while a constant relative pressure of 0 Pa was imposed at the outlet. Free slip were also applied at the top and bottom surfaces of the computational domain. Since the focus of this study is to investigate the effect of slip on the wall of the airfoil at $\alpha = 12^\circ$, two boundary conditions were used with varying inlet velocity direction. Initially, a no-slip boundary condition was assigned to

the wall surfaces, specifying zero velocity at the fluid-solid interface as shown in Fig. 3.2(a). Consequently, a slip surface boundary condition was modeled on the wall (Fig. 3.2(b)) using the Navier slip boundary condition as shown in Eq. (2.5) to assume a SHS. As a result, a UDF script was written and compiled using the in-built compiler in FLUENT software. It is interesting to note that the U_s on the surface was obtained by iteratively executing the equation with low relaxation factor in each iteration. The U_s obtained was used to modify the airfoil wall boundary condition in the software.

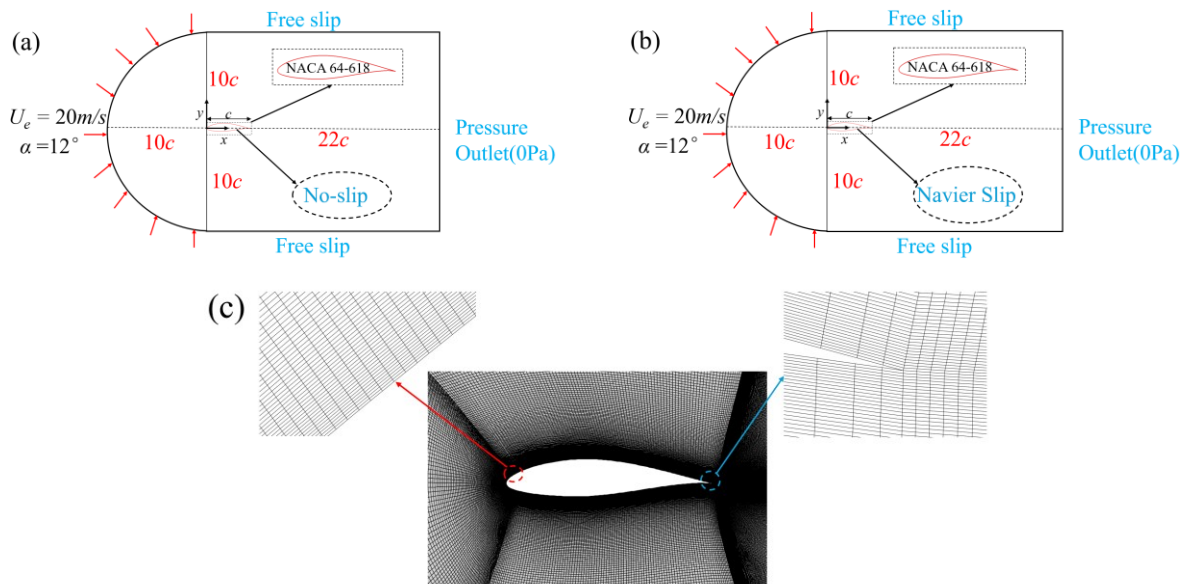


Figure 3.2. Schematic diagram of the (a-b) computational domain with their respective boundary conditions and (c) mesh distribution around the airfoil model.

3.1.3 Numerical settings

All numerical simulations were performed using ANSYS Fluent 2024 R1, a finite volume solver employed to discretize the incompressible Navier-Stokes equations. The simulations were conducted utilizing a second-order implicit temporal scheme to ensure enhanced accuracy in capturing time-dependent flow dynamics. Spatial terms discretization utilized a second-order

upwind scheme to minimize numerical diffusion and improve the resolution of flow structures. Pressure-velocity coupling was performed by the SIMPLE algorithm ensuring robust convergence for the incompressible flow solver. The time-step size was set to $\Delta t = 3 \times 10^{-4}$ s. To maintain numerical stability and accuracy, the maximum Courant-Friedrichs-Lewy (CFL = $u\Delta t/\Delta x$) number was constrained to 1 throughout the simulation. The convergence criterion for solving the momentum and continuity (Poisson) equations was defined to be 1×10^{-6} based on the maximum residual difference in each velocity component. All the computations were performed using a high-performance computing cluster ACENET-Beluga equipped with Intel Gold 6148 Skylake 2.4 GHz chip technology. The total computing time spent on solving the entire flow field and collecting the statistics averaged around 300 CPU hours. Prior to collecting flow statistics, it was essential to ensure that the flow had reached a statistically stationary state. To achieve this, the simulation was initially run for 10 flow-through times (FFT) to allow the flow field to fully develop. Subsequently, flow statistics were gathered over a period of approximately 5.5 FFT.

3.2 Mesh independence study and Validation

Four different mesh sensitivity analysis (M_1, M_2, M_3, M_4) were developed around the NACA 64–618 airfoil at $Re_c = 1.3 \times 10^6$ and $\alpha = 0^\circ$ with URANS. The corresponding results for the lift coefficient ($C_L = \frac{F_L}{0.5\rho U_e^2 A}$), drag coefficient ($C_D = \frac{F_D}{0.5\rho U_e^2 A}$) and pressure coefficient ($C_P = \frac{P - P_\infty}{0.5\rho U_e^2}$), are presented in Table 1 and Fig. 3.3(a). The mesh sensitivity analysis revealed that the relative error in C_l and C_d between M_3 and M_4 was less than 1%, indicating that further mesh refinement had a negligible impact on the aerodynamic coefficients. Moreover, C_p distribution across the airfoil surface showed convergence with increasing mesh resolution. Since we aim to reduce computational cost, and the differences in key aerodynamic parameters between M_3 and M_4 remain insignificant, M_3 was selected for further validation and analysis.

Table 3.1. Mesh sensitivity analysis

Mesh	Number of elements	y_{max}^+	C_l	C_d
M_1	250,000	5	0.458	0.0025
M_2	500,000	2	0.455	0.0028
M_3	750,000	0.6	0.452	0.0029
M_4	1,000,000	0.3	0.451	0.0030

Since no direct reference data is available for the coated NACA 64-618 airfoil, a comparative analysis was conducted using published results for the non-coated airfoil (Abbott & Von Doenhoff, 2012; Romani et al., 2018). The comparison includes the C_l at different $\alpha = 0^\circ, 4^\circ, 8^\circ,$ and 12° and the C_p distribution along the airfoil at $\alpha = -0.88^\circ$. Figure 3.3(b) illustrates the variation of C_p along the normalized chord length (x/c) at $\alpha = -0.88^\circ$. The numerical results from the present study show good agreement with experimental data across most of the chord length. However, a small discrepancy is observed in the suction region near the airfoil's upper surface ($x/c = 0.6$) where the numerical prediction slightly underestimates the experimental data with a relative error of approximately 15%. Figure 3.3(c) represents the variation of C_l as a function of α . The numerical predictions align closely with the wind tunnel results from Abbott and Von Doenhoff (2012) demonstrating a consistent trend across the range of angles considered. The C_l increases steadily with α , with a noticeable nonlinear growth at higher angles, particularly near $\alpha = 12^\circ$. This behavior indicates the onset of flow separation effects at high α , which are well captured by the present numerical approach. The overall agreement between the numerical and experimental results confirms the reliability and accuracy of the simulation framework for further analysis.

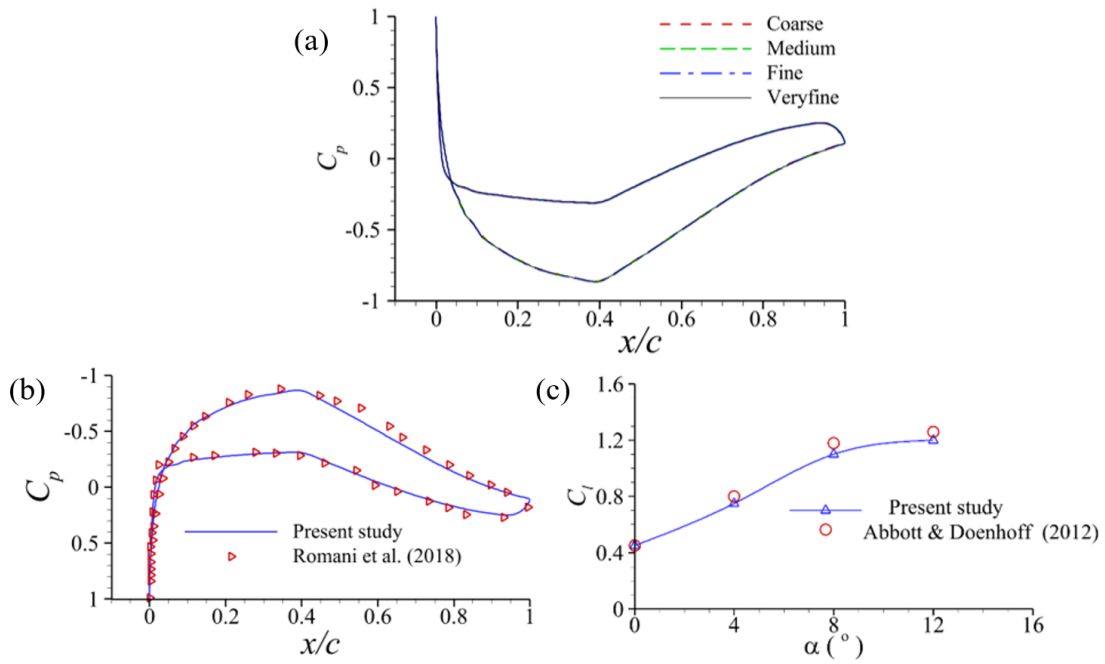


Figure 3.3. (a) Distribution of mean pressure coefficient on the upper and lower surface of NACA 64-618 at $\alpha = 0^\circ$ for the four meshes (b-c) Comparison of mean pressure and lift coefficient of the present study with experimental data for no-slip boundary condition.

CHAPTER 4 RESULTS AND DISCUSSIONS

4.1 Instantaneous flow fields

The unsteady flow around the airfoil is examined using the instantaneous spanwise vorticity flow fields under both baseline no-slip and slip conditions. The instantaneous spanwise vorticity, computed from $\omega_z = \left| \frac{\partial v}{\partial x} - \frac{\partial u}{\partial y} \right|$, are shown in Fig. 4.1 for both conditions. Generally, the instantaneous vorticity field is characterized by a counter-rotating vortex pair. Notably, the flow topology reveals alternating vortex shedding from the upper and lower surfaces of the airfoil, flanked by regions of high vorticity magnitudes (red and blue). This vortex shedding arises from the shear layer instabilities at the interface comparable to the Kelvin-Helmholtz (KH) type.

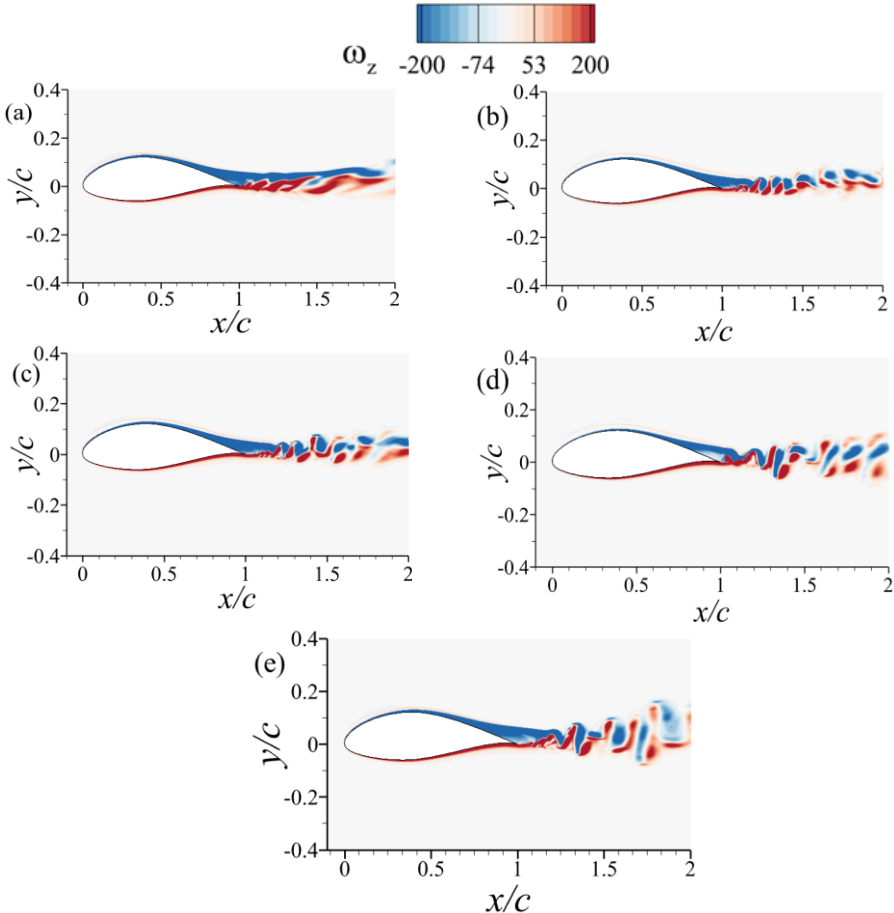


Figure 4.1. Contours of instantaneous vorticity for (a) no-slip (b) $L_s = 100 \mu\text{m}$ (c) $L_s = 140 \mu\text{m}$ (d) $L_s = 185 \mu\text{m}$ (e) $L_s = 400 \mu\text{m}$.

The KH-type instabilities at the interface amplifies small perturbations that subsequently grow and roll into vortices creating wave-like structures similar to the von Kármán vortex. The prominence of the KH and rollup vortices suggests the existence of varying length and time scales of the turbulent structures embedded within the wake region. The onset of vortex shedding and the rolling-up of vortices in the wake region is strongly influenced by the surface treatment and α . To compare the effect of slip on the flow field, snapshots of the vorticity field for the different test cases have been presented in Fig. 4.1 (a-e). The snapshots were captured after a one flow through cycle for all cases. As expected, flow separation is clearly observed at the trailing edge with earlier detachment of the boundary layer on the upper surface due to the adverse pressure gradient. In both cases, the instability within the shear layers intensifies, eventually forcing the layers to roll up into Kármán vortex-type structures in the near wake region. However, the onset of these roll-up vortices is not prominent in the baseline case. As observed, the shear layer elongates and moves further downstream before the roll-up begins. This is consistent with results from Sooraj et al. (2020) on the flow field around a smooth cylinder. Upon introducing slip, modifications of the wake structure become apparent. In all slip cases, the slip effect promotes the early roll up of these vortices in the near and far wake, as they convect downstream shown in Fig. 4.1(b-e). This early roll-up of the vortex can be attributed to reduction in the recirculation region at the trailing edge of the airfoil which eventually leads to flow acceleration in the wake. This finding aligns with earlier studies conducted by Sooraj et al. (2020) and Kim et al. (2015).

4.2 Mean flow field

4.2.1 Mean flow contours

The contours of the normalized streamwise mean velocities (U/U_e) for all test cases are presented in Fig. 4.2 (a-e) to examine the mean flow features around the airfoil. Generally, the flow topology revealed flow deceleration at the leading edge, acceleration at the suction surface

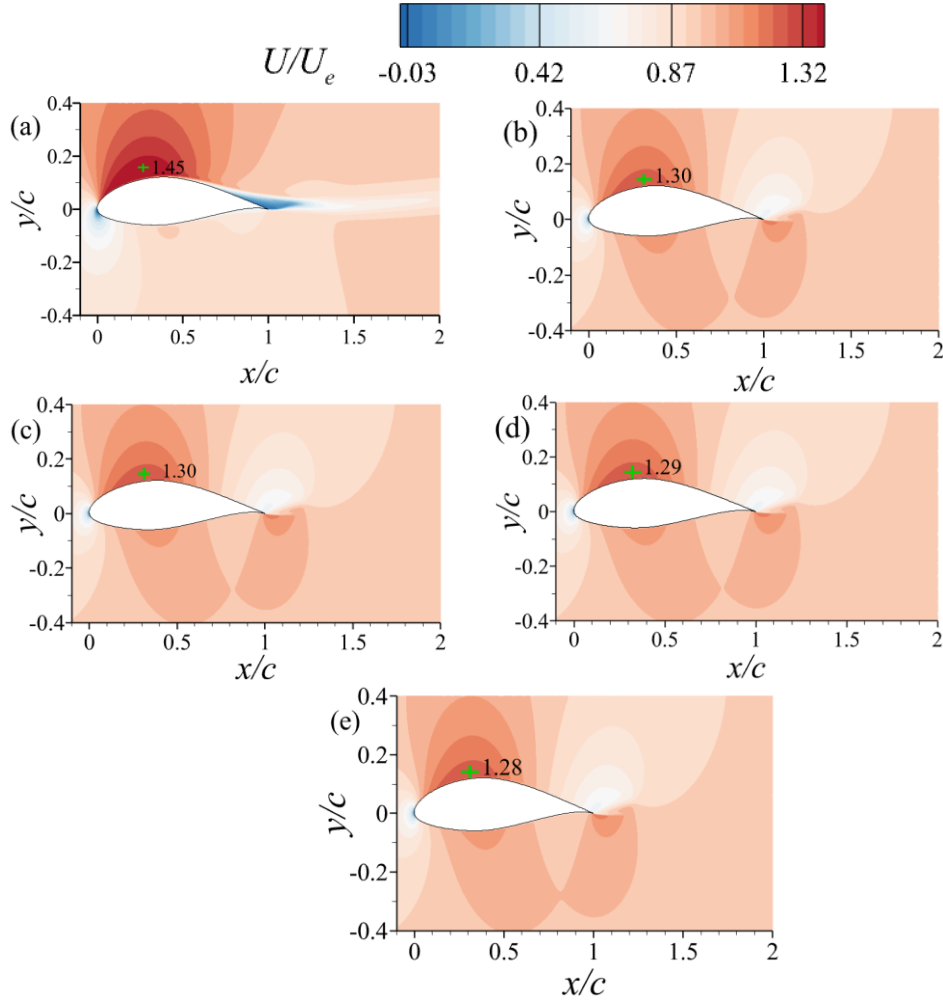


Figure 4.2. Contours of mean streamwise velocities for (a) no-slip (b) $L_s = 100 \mu\text{m}$ (c) $L_s = 140 \mu\text{m}$ (d) $L_s = 185 \mu\text{m}$ (e) $L_s = 400 \mu\text{m}$. The location (green '+' symbol) and magnitudes of peak values are also indicated.

of the airfoil and separation at the trailing edge due to adverse pressure gradient similar to reports by Gautam et al. (2024). For the no-slip case shown in Fig. 4.2(a), a distinct reverse flow region ($U < 0$) at the suction surface near trailing edge is observed indicating the presence of a recirculation bubble. However, it is interesting to note that the boundary layer remains attached to the surface for the slip cases as shown in Fig. 4.2(b-e). This means that the slip induced a non-zero slip velocity which overcame the adverse pressure gradient thereby suppressing of the

separation bubble. This observation is consistent with PIV measurements over a SHC NACA 0015 reported by Sooraj et al. (2019) as well as studies on flow around a circular cylinder by Kim et al. (2015), both of which demonstrated reduced separation under slip conditions. Also, compared to the no-slip case, flow acceleration and faster velocity recovery in the wake region were observed for the slip cases.

To further explore the flow dynamics around the airfoil, the maximum streamwise velocity (U_{max}/U_e) was identified for all test cases, along with their corresponding magnitudes. Notably, in all configurations, the peak velocities were located along the suction side of the airfoil. The highest peak velocity was observed for the no-slip configuration, with $U_{max}/U_e = 1.45$. When the slip was introduced, a progressive reduction in the peak velocity was observed. Specifically, U_{max}/U_e decreased to 1.28 for the largest slip length, $L_s = 400 \mu\text{m}$ representing a relative reduction of approximately 11.72% compared to the no-slip case. This monotonic reduction in U_{max}/U_e with increasing L_s reflects a fundamental alteration in boundary layer dynamics induced by the slip condition. The reduction in peak velocity can be attributed to the presence of finite slip at the wall, which decreases the wall shear stress and introduces a non-zero slip velocity at the fluid–solid interface. This reduction in near-wall shear leads to a more gradual acceleration along the suction surface and, consequently, a moderated pressure recovery downstream of the velocity peak. The resulting weakening of the adverse pressure gradient reduces the decelerating effect on the low-momentum fluid near the wall, thereby enhancing boundary layer stability and decreasing the occurrence of flow separation.

4.2.2 Variation in time-averaged wake velocity characteristics

To further investigate the evolution of mean flow field in the wake region of the airfoil, the normalized streamwise velocity along the airfoil centerline spanning from $x/c \in [0.96, 2.00]$ was

examined for the different conditions and presented in Fig. 4.3 (a-f). As can be seen from the no-slip condition, the velocity exhibits a pronounced deficit immediately downstream of the trailing edge, characterized by a region of reversed flow with negative velocity values ($U < 0$). This behavior is indicative of the presence of a recirculation bubble as previously discussed for Fig. 4.2(a). The streamwise velocity remains significantly below the U_e until $x/c = 1.06$, beyond which a sharp recovery is initiated. This rapid increase persists until $U/U_e \approx 0.65$, after which the velocity continues to rise more gradually downstream. In contrast, the introduction of the surface slip demonstrated a progressive reduction in the size and strength of the recirculation region following an earlier initiation of velocity recovery corresponding to increasing slip lengths. Among the slip configurations, the cases with $L_s = 100 \mu\text{m}$, $L_s = 140 \mu\text{m}$ and $L_s = 185 \mu\text{m}$, exhibited similar characteristics. Despite their similarity, each case demonstrates a measurable reduction in the initial streamwise velocity deficit immediately downstream of the trailing edge relative to the no-slip condition, indicating a consistent reduction of near-wake momentum loss across this range of slip lengths. The effect becomes more pronounced for the case with $L_s = 400 \mu\text{m}$. This configuration yields faster velocity recovery reaching $U/U_e \approx 1$ earlier than in the other cases specially between $x/c = 1.06$ to $x/c = 1.28$. This can be attributed to a substantial reduction in shear-induced energy loss due to the enhanced slip effect as a result of strong entrainment of freestream fluid through the shear layers. Similar trends in wake recovery and entrainment enhancement were also reported by Lee et al. (2018) and Hasheminasab et al. (2021).

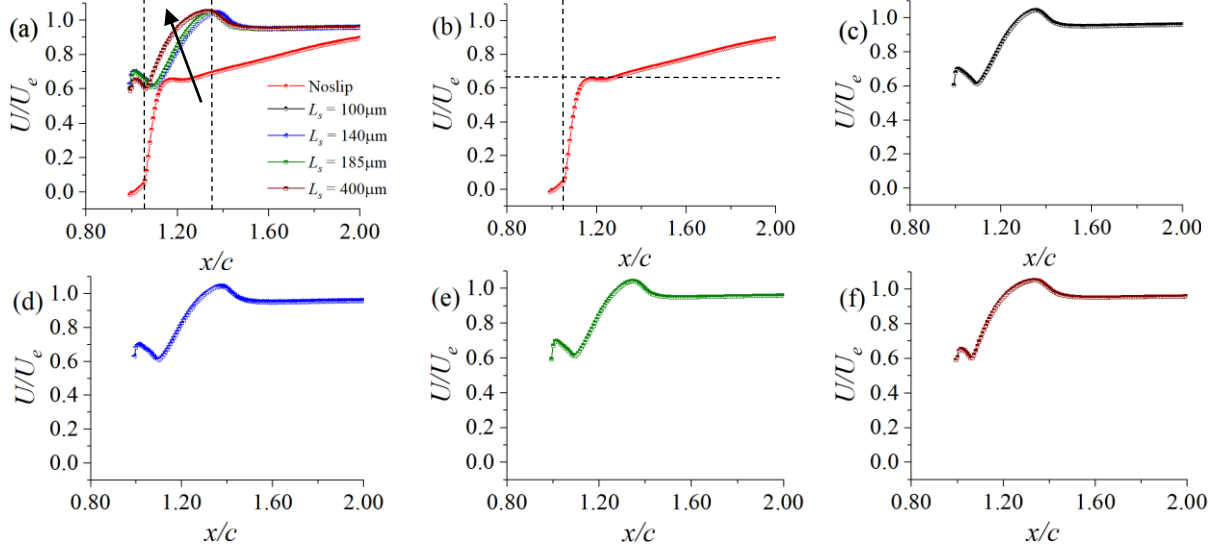


Figure 4.3. Velocity profiles downstream the trailing edge of the airfoil for (a) all conditions (b) no-slip (c) $L_s = 100 \mu\text{m}$ (d) $L_s = 140 \mu\text{m}$ (e) $L_s = 185 \mu\text{m}$ (f) $L_s = 400 \mu\text{m}$. The centerline profiles were extracted at $y/c = 0.02$ and spans $x/c \in [0.96, 2.00]$.

4.3 Power spectral density analysis on the separated shear layer

To investigate the influence of surface slip on the unsteady dynamics of the shear layer, a set of pointwise velocity probes were strategically positioned above the suction surface of the airfoil, as illustrated in Fig. 4.4. The probe locations, denoted P_1 through P_6 , span along the shear layer, beginning near the expected separation point and extending downstream into the near wake. Each probe records the instantaneous streamwise velocity component $u(t)$ at a fixed spatial location. These time-resolved signals serve as the basis for computing the power spectral density (PSD), thereby allowing the identification of characteristic frequencies associated with shear layer instabilities and their modulation under both the no-slip baseline case and the various slip-modified configurations. This comparison will facilitate a detailed examination of how wall slip alters the spectral content of the separated flow, particularly the dominant shedding frequencies and energy distribution across scales.

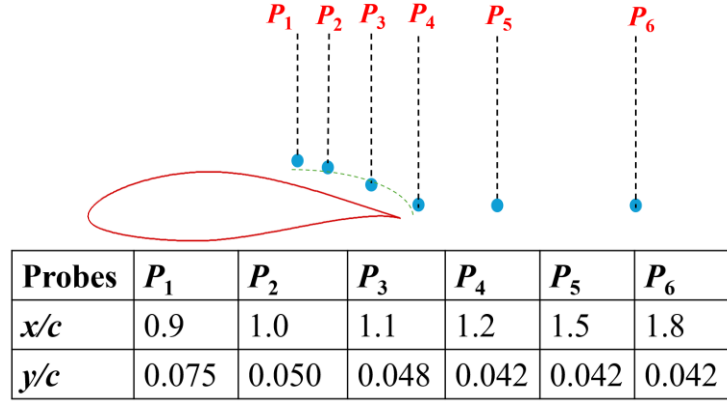


Figure 4.4. Schematic of probe locations for extracting instantaneous streamwise velocity signals.

The PSD was determined by applying a fast-Fourier transformation to the temporally oscillating instantaneous velocity signals measured at the probe locations. A Hanning windowing technique was employed to minimize discontinuities at the signal boundaries, ensuring clearer resolution of dominant frequency components. To further improve the clarity of the spectra, smoothing was also performed to suppress random noise and enhance the visibility of persistent spectral features. All the spectra exhibited multiple peaks at certain Strouhal (St) numbers defined as $St = \frac{fc}{U_e}$ where f is the frequency. Typically, the flow along the shear layer is dominated by energetic vortical structures that contain varying energy levels at different frequencies. A careful examination of Figs. 4.5(a-f) and 4.6(a-f) reveal three characteristic subranges in the energy spectra for all locations. The low-frequency region is associated with large-scale, energy-containing eddies that govern the initial stages of turbulence production, whereas the high-frequency range corresponds to the dissipation of smaller-scale structures through viscous effects (Gautam et al., 2024; Hasheminasab et al., 2021; Hossen et al., 2025; Saeedi et al., 2024). The inertial subrange is characterized by the $-5/3$ slope, which is consistent with Kolmogorov's K41 theory (Pope, 2001). As an initial step, the spectral analysis was performed for the no-slip baseline

case to characterize the evolution of the dominant flow dynamics along the separated shear layer as illustrated in Fig. 4.5(a-f).

At P_1 , the spectral energy content ($<10^{-4}$) was low and broadly distributed, with no distinct peak frequency. This indicates the initial onset of instability where the shear layer is still in a state of linear disturbance growth. At this stage, the energy was diffusely distributed across a wide range of high frequencies, indicating the absence of organized vortical structures. Further downstream, P_2 exhibited a noticeable elevation in energy ($>10^{-4}$) particularly in the low frequency range. This suggests the amplification of shear-layer instabilities as the separated flow begins to organize into larger-scale structures. However, while the energy levels increased, the associated spectral peaks at lower $St = 0.35$, and 0.40 were not dominant throughout the flow. Instead, they vary in strength, indicating a transitional regime where unsteady motions begin to emerge but have not yet fully saturated into a coherent, global shedding mode. It is interesting to note that, across P_3 through P_6 , a strong narrowband peak is consistently observed at $St \in [0.85, 1.00]$ denoted here as St_{vk} corresponding to the primary vortex shedding frequency. Broadband peaks corresponding to the Kelvin-Helmholtz (KH) frequencies are also observed at $St_{kh} = 1.90$, $St_{kh} = 2.00$, $St_{kh} = 2.00$ and $St_{kh} = 2.00$, $St_{kh} = 6.50$ for P_3 , P_4 , P_5 , P_6 respectively. These frequencies reflect small-scale convective instabilities that develop as the separated shear layer evolves and transitions toward turbulence (Kumahor & Tachie, 2023; Moore et al., 2019).

To understand the influence of slip on the shear layer evolution, Fig. 4.6 (a-f) presents a comparison of the PSD of the streamwise instantaneous velocity between the no-slip baseline and the slip-modified cases at the same probe locations considered earlier. The PSD curves are superimposed to facilitate direct comparison of the spectral modulation introduced by surface slip. A notable feature observed is the downstream migration of the dominant shedding frequency to

lower St , particularly for the $L_s = 400\mu\text{m}$. This behavior contrasts with the no-slip baseline spectra and offers insight into the influence of surface slip on the shear layer development. At P_3 , downstream the separation point, the dominant vortex shedding frequency for the no-slip case occurs around $St_{vk} = 0.96$, whereas the corresponding peak for the $L_s = 400\mu\text{m}$ migrates to $St_{vk} = 0.80$. This migration towards lower frequencies suggests the early onset of small-scale vortex pairing and fluid entrainment, leading to the formation of larger-scale coherent structures downstream. As vortices entrain more surrounding fluid, their frequency decreases due to the

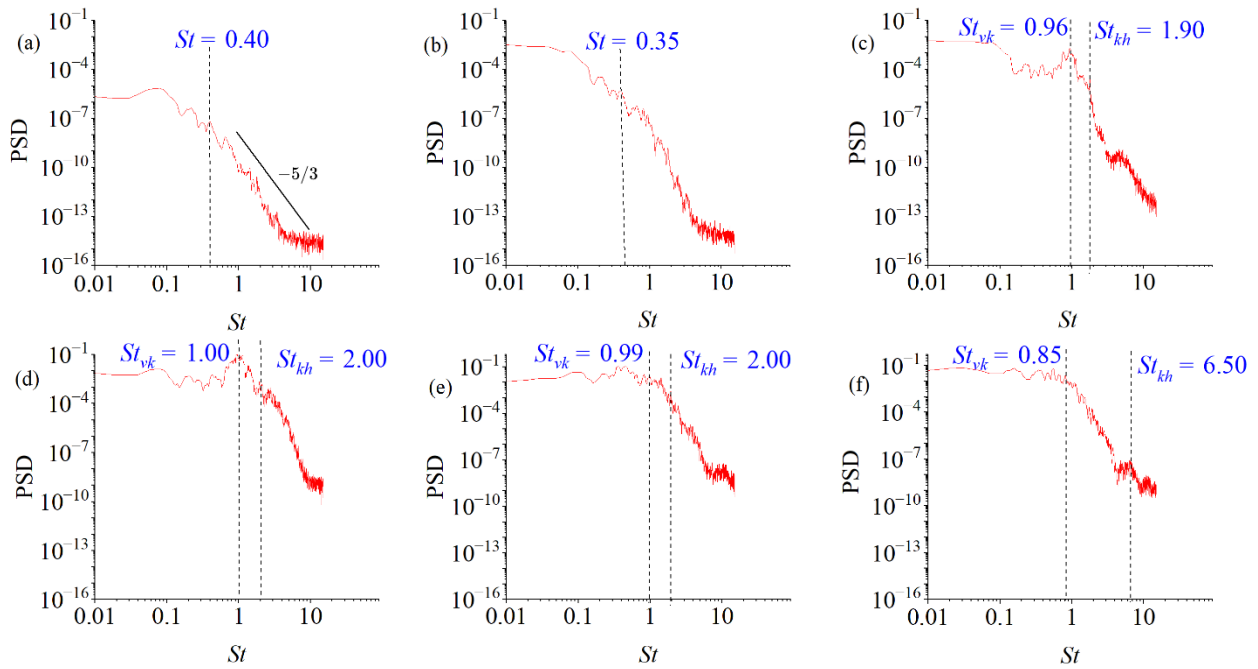


Figure 4.5. Power spectral density of streamwise instantaneous velocity signal measured along the separated shear layer for the no-slip baseline case at the selected probe locations.

increased effective mass and scale, resulting in a lower St . At P_4 , the shedding frequency remains relatively consistent between slip and no-slip conditions, implying a localized equilibrium in instability growth. However, at P_5 , the dominant frequency migrated from $St_{vk} = 0.99$ to $St_{vk} = 0.80$. This repeated frequency decrease downstream is indicative of continued entrainment, vortex merging. Although P_6 exhibits similar frequencies in both configurations, the earlier migration to

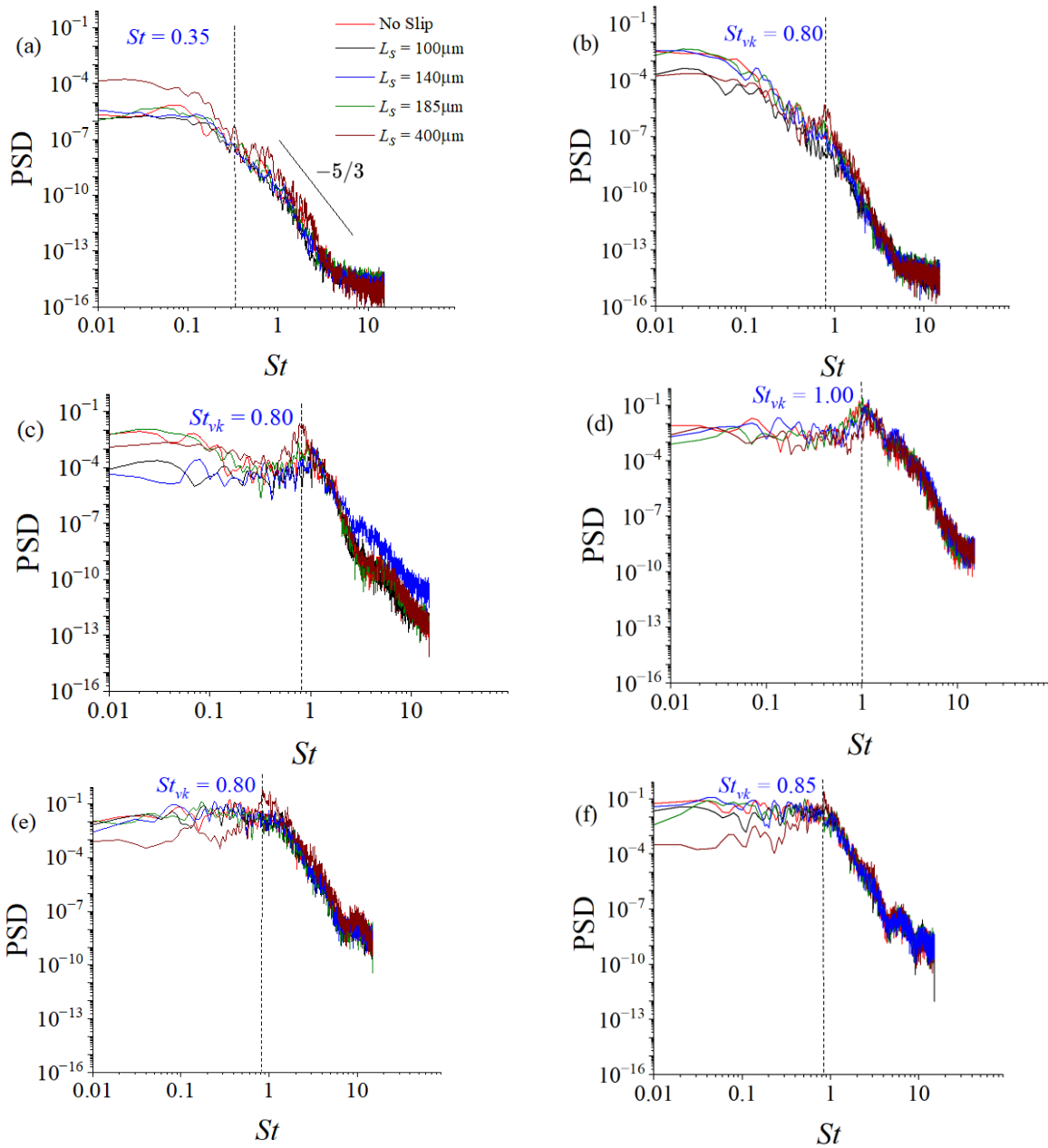


Figure 4.6. Comparison of the spectral characteristics of the streamwise instantaneous velocity along the separated shear layer between the no-slip baseline and varying slip conditions at the selected probe locations.

lower frequencies in the slip cases reflects a clear change in the downstream evolution of the separated shear layer. These shifts provide spectral evidence of entrainment and vortex merging,

which are consistent with observations in the mean flow field and highlight the role of slip in influencing vortex dynamics and the scale of unsteady motions in the wake.

4.4 Proper orthogonal decomposition

The POD technique, originally introduced by Lumley (1967), is employed to perform modal analysis of the fluctuating velocity field. Since its introduction, the POD technique has been applied to investigate coherent structures in turbulent jet flows (Nyantekyi-Kwakye et al., 2016) and separated flows (Agyei-Agyemang et al., 2024; Israel et al., 2025; Kumahor & Tachie, 2023). In the present study, the snapshot method proposed by (Sirovich, 1987) was used to decompose the fluctuating velocity vector field $u'(\mathbf{x}, t)$ into a combination of spatial modes and their respective temporal coefficients using Eq. (4.1).

$$u(\mathbf{x}, t) = \sum_{n=1}^N a_n(t) \Phi_n(\mathbf{x}) \quad (4.1)$$

where N is the number of snapshots, Φ_n is the spatial POD mode magnitude and $a_n(t)$ the temporal coefficients for the modes. The POD analysis was performed over the flow field spanning $x/d \in [-0.99, 1.8]$ and $y/d \in [-0.2, 0.2]$. This area was chosen to encompass the evolution of vortices in the wake region. Since the accuracy of the POD analysis is dependent on the number of snapshots, a convergence of the POD results was evaluated by computing the fractional turbulent kinetic energy associated with the first mode for increasing N . Results of the energy convergence for all test cases were qualitatively similar as shown in Table 4.1. The energy fraction for the first mode decreased with increasing N until a threshold value was attained where the fractional energy became independent of N . For instance, in all cases, increasing N from 2500 to 3000 yielded fractional turbulent kinetic energy errors of 5.1%, 2.7%, 3.2% and 2.6% for no-slip, $L_s = 100 \mu\text{m}$,

$L_s = 140 \mu\text{m}$ and $L_s = 185 \mu\text{m}$ respectively as shown in Table 2. Based on these observations, it was determined that $N = 3000$ was sufficient to perform the POD analysis.

Table 4.1. Convergence test

Snapshots	No-slip		$L_s = 100 \mu\text{m}$		$L_s = 140 \mu\text{m}$		$L_s = 185 \mu\text{m}$	
	Energy	Error	Energy	Error	Energy	Error	Energy	Error
100	0.191	---	0.159	---	0.209	---	0.217	---
500	0.111	72.1	0.117	35.9	0.131	59.5	0.109	99.1
1000	0.113	1.8	0.118	0.9	0.128	2.3	0.107	1.9
1500	0.107	5.6	0.111	6.3	0.122	4.9	0.115	6.9
2000	0.102	4.9	0.105	5.7	0.125	2.4	0.116	0.9
2500	0.103	1.0	0.110	4.6	0.123	1.6	0.113	2.7
3000	0.098	5.1	0.113	2.7	0.127	3.2	0.116	2.6

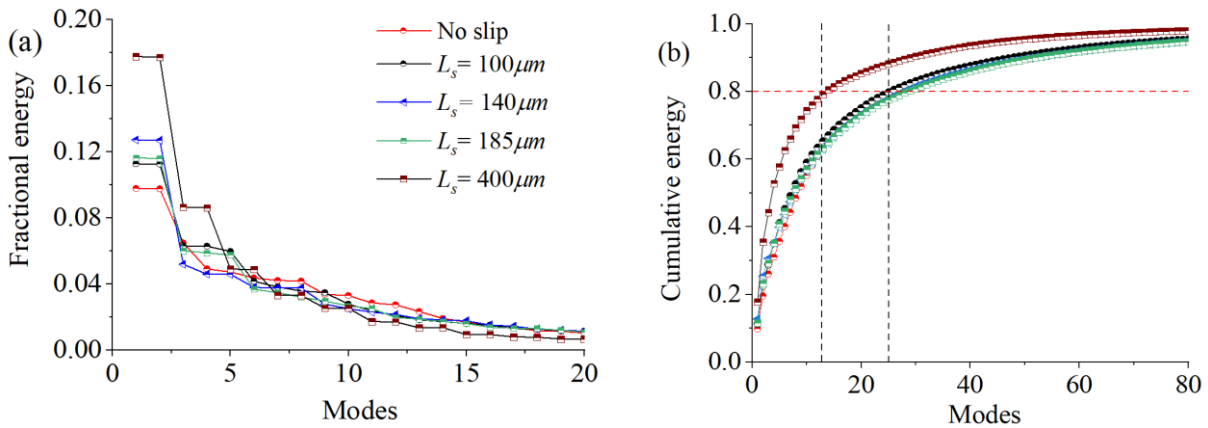


Figure 4.7. Fractional mode energy distribution for (a) first 20 modes and (b) cumulative energy distributions for baseline no-slip, $L_s = 100 \mu\text{m}$, $L_s = 140 \mu\text{m}$ and $L_s = 185 \mu\text{m}$, $L_s = 400 \mu\text{m}$.

Figure 4.7(a) shows fractional energy contribution over the first 20 POD modes. The first modes contributed 9.9%, 11.3%, 13%, 11.8% and 17% of the total kinetic energy for no-slip, $L_s = 100 \mu\text{m}$, $L_s = 140 \mu\text{m}$, $L_s = 185 \mu\text{m}$ and $L_s = 400 \mu\text{m}$ respectively. It is interesting to note that, for the slip cases, modes 1 and 2, 3 and 4 contain approximately the same energy content (see Fig. 4.7(a)), indicating that they potentially represent mode pair. An exception is observed in the $L_s = 140 \mu\text{m}$ where the mode 3 and 4 showed slight differences in energy. Additionally, the cumulative energy distribution over the first 80 POD modes, as shown in Fig. 4.7(b), indicates that

approximately 80% of the total energy is captured by the first 14 modes for the $L_s = 400 \mu\text{m}$ case, whereas about 25 modes are required to reach the same energy threshold in the no-slip, $L_s = 100 \mu\text{m}$, $L_s = 140 \mu\text{m}$ and $L_s = 185 \mu\text{m}$ cases, which exhibit similar energy distribution characteristics. In general, this highlights a shift in the energy distribution of the modes for the slip case especially $L_s = 400 \mu\text{m}$ and the potential for stronger contributions from coherent structures. This finding supports the notion that slip generally modifies the dissipative small scales close to the surface while promoting the formation of organized convective large-scale structures. These observations are consistent with earlier work by Sooraj et al. (2020) despite difference in Re and energy content.

To show a typical pattern and the flow behavior associated with the convective structures within the wake, Figs. (4.8 - 4.12) displays the first four spatial POD modes for no-slip, $L_s = 100 \mu\text{m}$, $L_s = 140 \mu\text{m}$, $L_s = 185 \mu\text{m}$ and $L_s = 400 \mu\text{m}$. It is interesting to note that, the first two spatial patterns for all cases showed a strong mode pair indicative of the similar energy content. To further confirm, Riches et al. (2018) states that besides the similarity in energy content of the mode pairs, the spatial modes must be shifted by one quarter wavelength ($\lambda/4$) of the convective structures. Additionally, the associated mode coefficients must be phase shifted by 90° ensuring that their phase portraits in space exhibit discernible circular patterns. The local wavelength (λ) of the convective structures is defined here as the distance between successive peaks of same-signed structures depicted in the POD spatial modes. As will be shown subsequently, the other two conditions are also satisfied, confirming that the dynamics of the convective structures related to the von-Kármán shedding process are effectively captured in the first mode pair. The vertical line on the spatial modes signifies the streamwise distance between adjacent peaks of opposite-signed structures used to represent one-half the wavelength ($\lambda/2$) of the convective structures and the results are summarised in Table 4.2. The wavelengths are all within $\lambda/2 = 0.06c \pm 0.01c$.

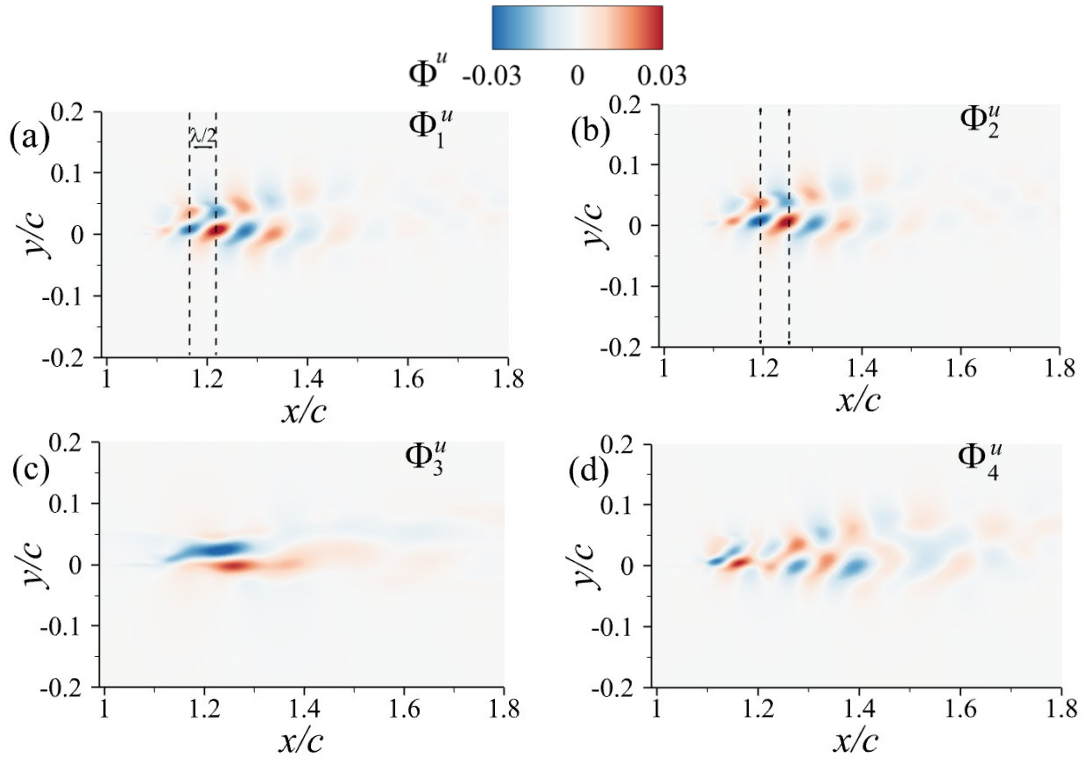


Figure 4.8. Contours of first four POD modes ($\Phi_{(j)}^u$) obtained from the streamwise velocity fluctuations for the baseline no-slip case.

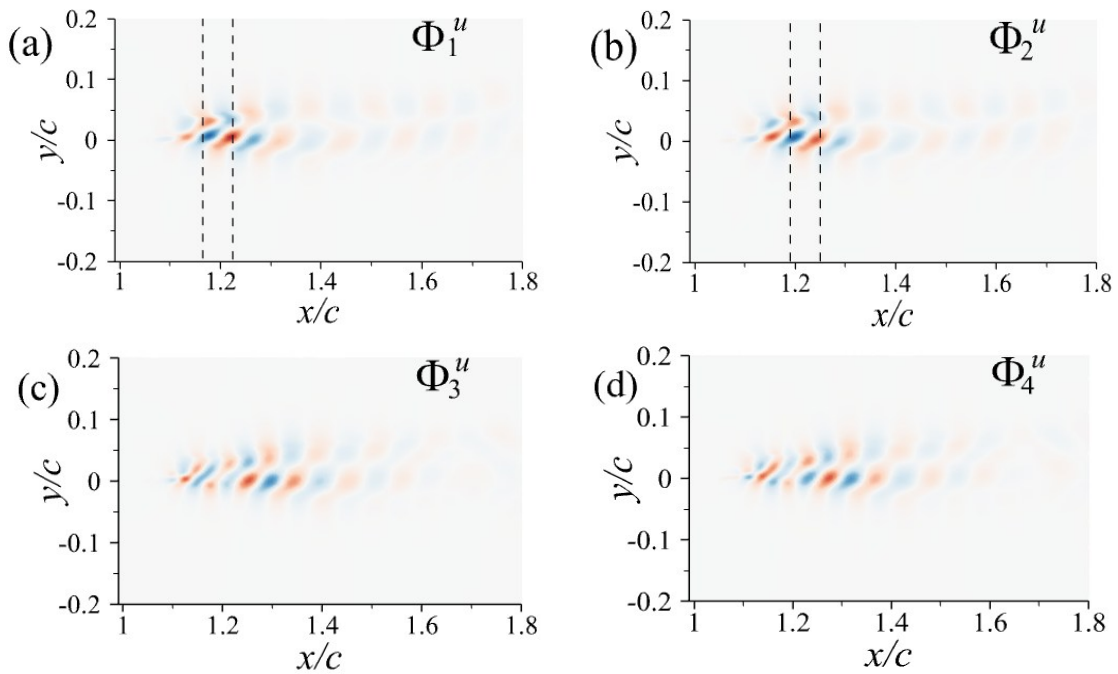


Figure 4.9. Contours of first four POD modes ($\Phi_{(j)}^u$) obtained from the streamwise velocity fluctuations for $L_s = 100 \mu\text{m}$.

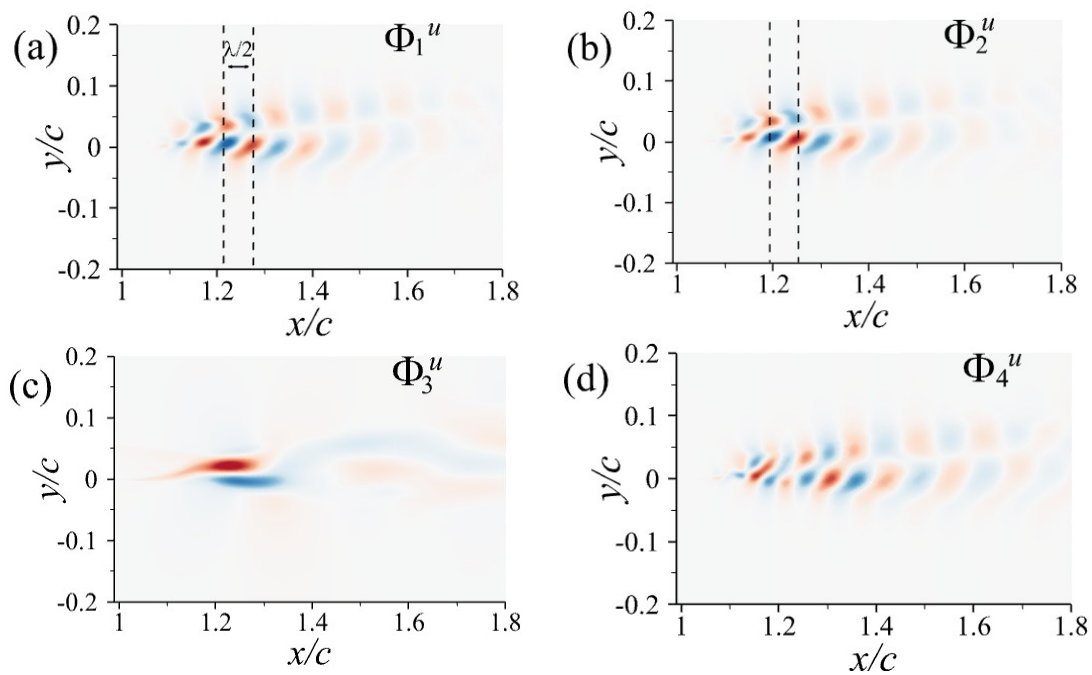


Figure 4.10. Contours of first four POD modes ($\Phi_{(j)}$) obtained from the streamwise velocity fluctuations for $L_s = 140 \mu\text{m}$.

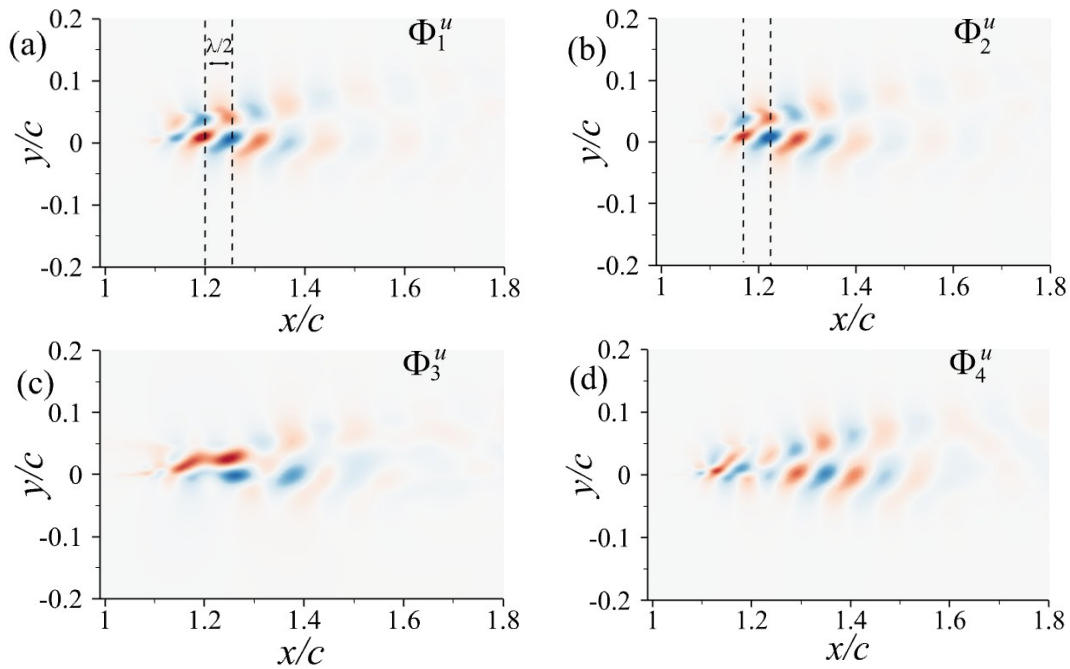


Figure 4.11. Contours of first four POD modes ($\Phi_{(j)}$) obtained from the streamwise velocity fluctuations for $L_s = 185 \mu\text{m}$.

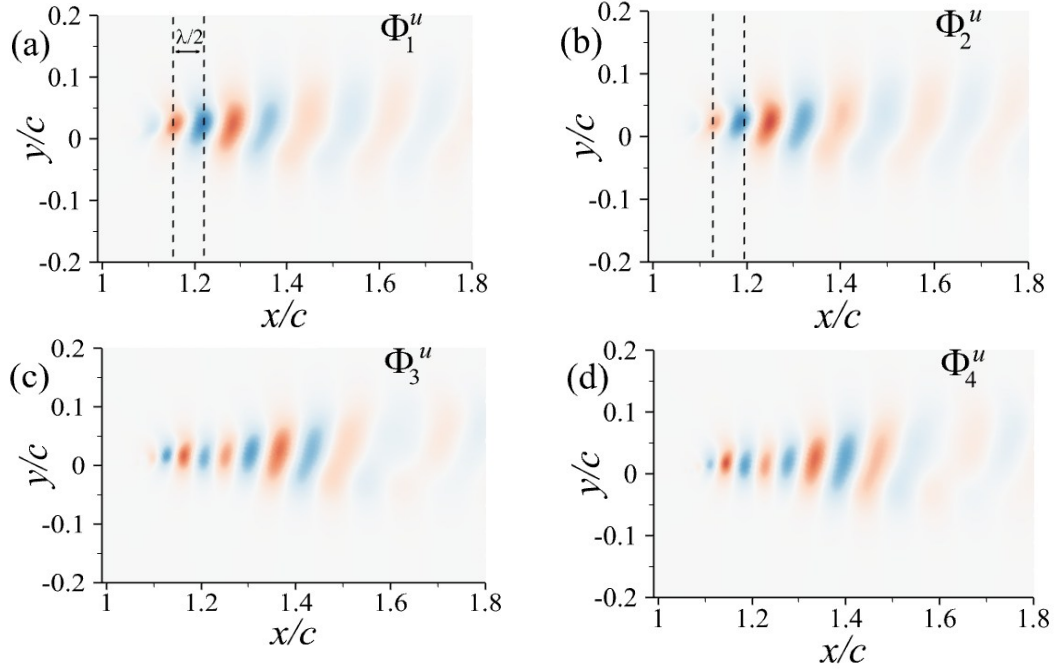


Figure 4.12. Contours of first four POD modes ($\Phi_{(j)}$) obtained from the streamwise velocity fluctuations for $L_s = 400 \mu\text{m}$.

Table 4.2. Summary of wavelengths for the different cases

Case	No-slip	$L_s = 100 \mu\text{m}$	$L_s = 140 \mu\text{m}$	$L_s = 185 \mu\text{m}$	$L_s = 400 \mu\text{m}$
$\lambda/2c$	0.06	0.05	0.06	0.06	0.07

The time evolution ($t^* = \frac{tU_e}{c}$) of the corresponding temporal coefficients ($a_{(j)}(t)$) associated with each mode along with their PSD and a phase portrait are presented in Figs. (4.13 - 4.17) for no-slip and all the slip cases respectively. The t^* and frequency spectra for a_1 and a_2 are found to be similar in all cases. The spectra exhibited dominant peaks around $St = 1$, highlighted by a vertical dashed line. Although slight differences in the frequency values are observed, these peaks are analogous to vortex shedding frequency as previously identified in the pointwise spectra of the instantaneous streamwise velocities. Additionally, as shown in the phase portraits, the relationship between a_1 and a_2 follows a circular trajectory in phase space. Also, a_1 and a_2 exhibited a sinusoidal

response with modulation in the amplitude over a time scale. This behavior is reflected in the phase portraits, where the points remain close to the origin, indicating a stable oscillatory nature.

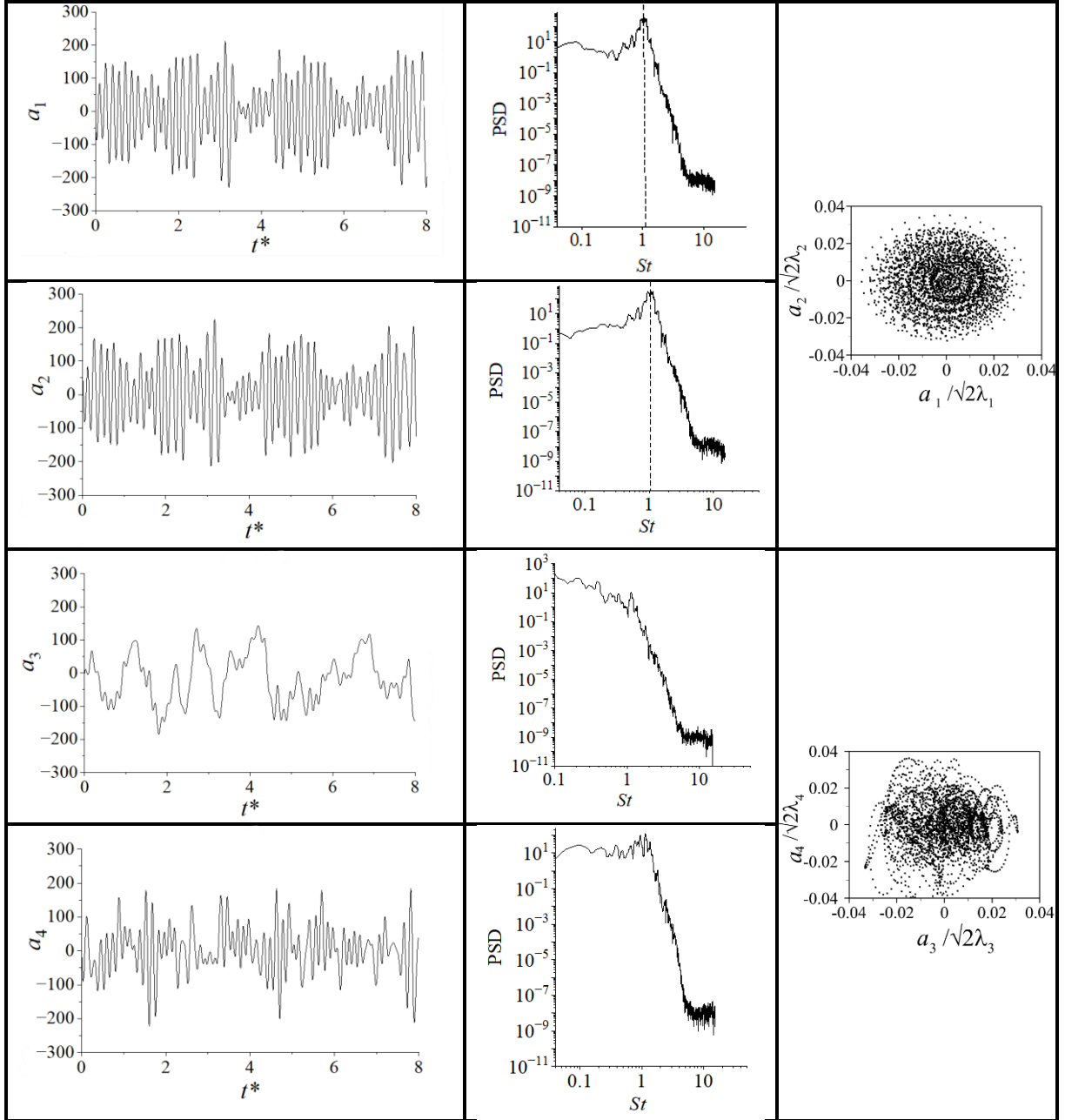


Figure 4.13. Time series history, frequency spectra and phase portrait of the temporal coefficients ($a_{(j)}(t)$) for baseline no-slip case.

In contrast, the dynamical characteristics underwent a qualitative shift for the third and fourth modes in all cases. The Φ_3'' and Φ_4'' , represents higher-order flow structures that contribute to secondary instabilities in the wake. In the baseline no-slip case, modes Φ_3'' and Φ_4'' fail to satisfy the criteria for mode pairing as previously defined. The PSD corresponding to a_3 and a_4 lack distinct peaks and instead display a broadband frequency distribution, suggesting the absence of a single dominant temporal scale. Moreover, the phase portrait is highly scattered, with no discernible geometric structure, which contrasts sharply with the coherent circular trajectory observed for the first two modes. However, a mode pair was observed in $L_s = 100 \mu\text{m}$. The contrast occurred for $L_s = 140 \mu\text{m}$ where a mode pair was not observed. This discrepancy suggests that at this specific slip length, the imposed slip condition did not induce the necessary flow organization to form a stable mode pair. Unlike the $L_s = 100 \mu\text{m}$ configuration, where sinusoidal amplitude modulation was evident, the $L_s = 140 \mu\text{m}$ case exhibited a more disordered dynamic behavior, with no clear modulation of the temporal coefficients. Given the relatively low energy contribution, the physical interpretation of these modes is left for future study.

The behavior of the Φ_3'' and Φ_4'' observed for $L_s = 185 \mu\text{m}$ and $L_s = 400 \mu\text{m}$ shows a notable flow organization compared to the cases with $L_s = 140 \mu\text{m}$. As shown in Fig. 4.16 and Fig. 4.17, the a_3 and a_4 for these slip lengths exhibit clearer amplitude modulation, and their PSD reveal distinct, well-defined peaks around the $St = 1.0$, which is characteristic of vortex shedding frequencies. This suggests a significant shift towards organized, periodic flow dynamics in the higher slip length cases. It is interesting to note that, the spatial patterns for $L_s = 400 \mu\text{m}$ changed to an elongated train of irregular lobe shapes indicating the emergence of larger-scale convective structures likely resulting from vortex pairing and strong entrainment processes. Such behavior is beneficial, as it promotes momentum exchange and can help delay boundary layer separation.

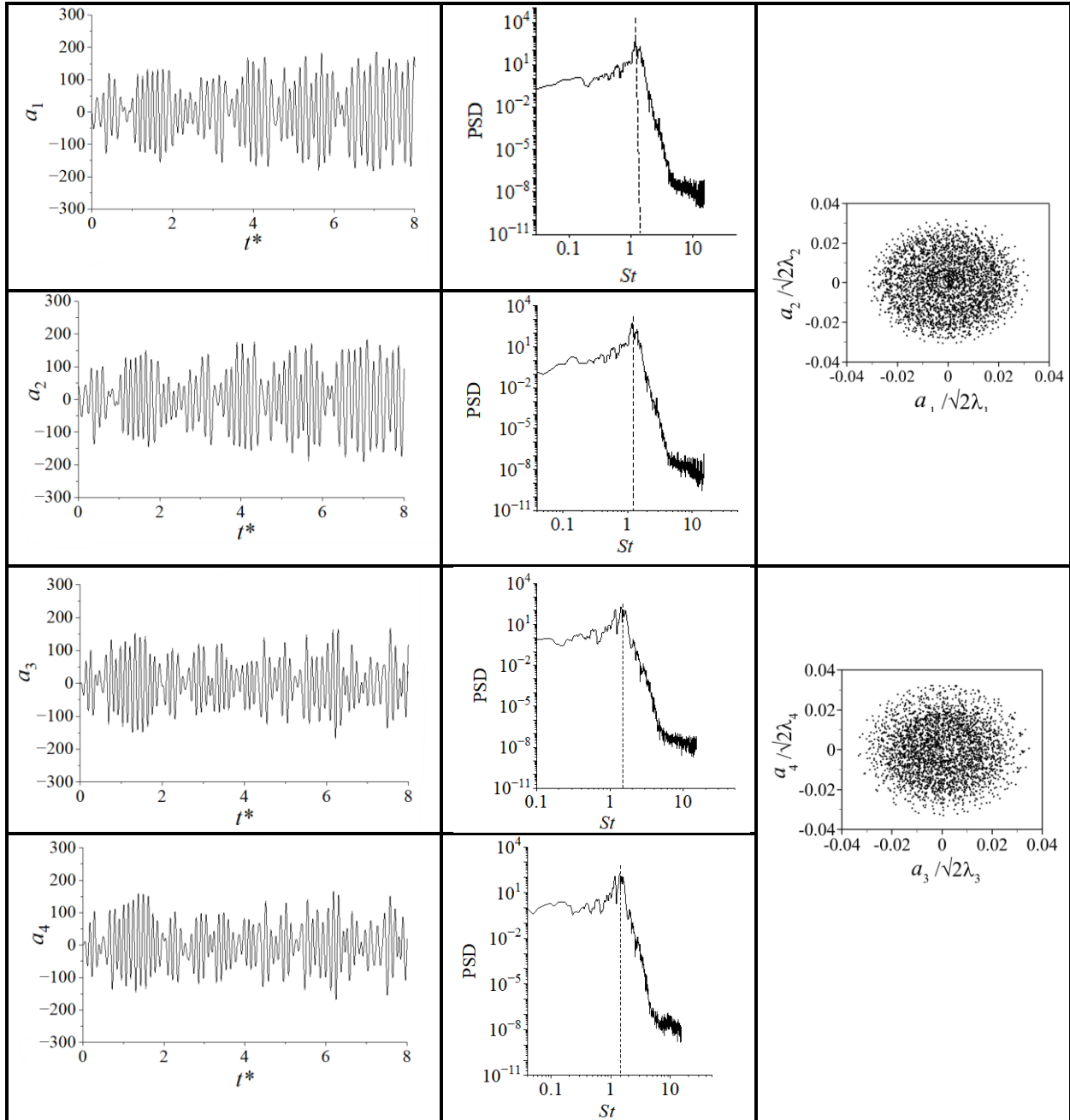


Figure 4.14. Time series history, frequency spectra and phase portrait of the temporal coefficients $(a_{(j)}(t))$ for $L_s = 100 \mu\text{m}$.

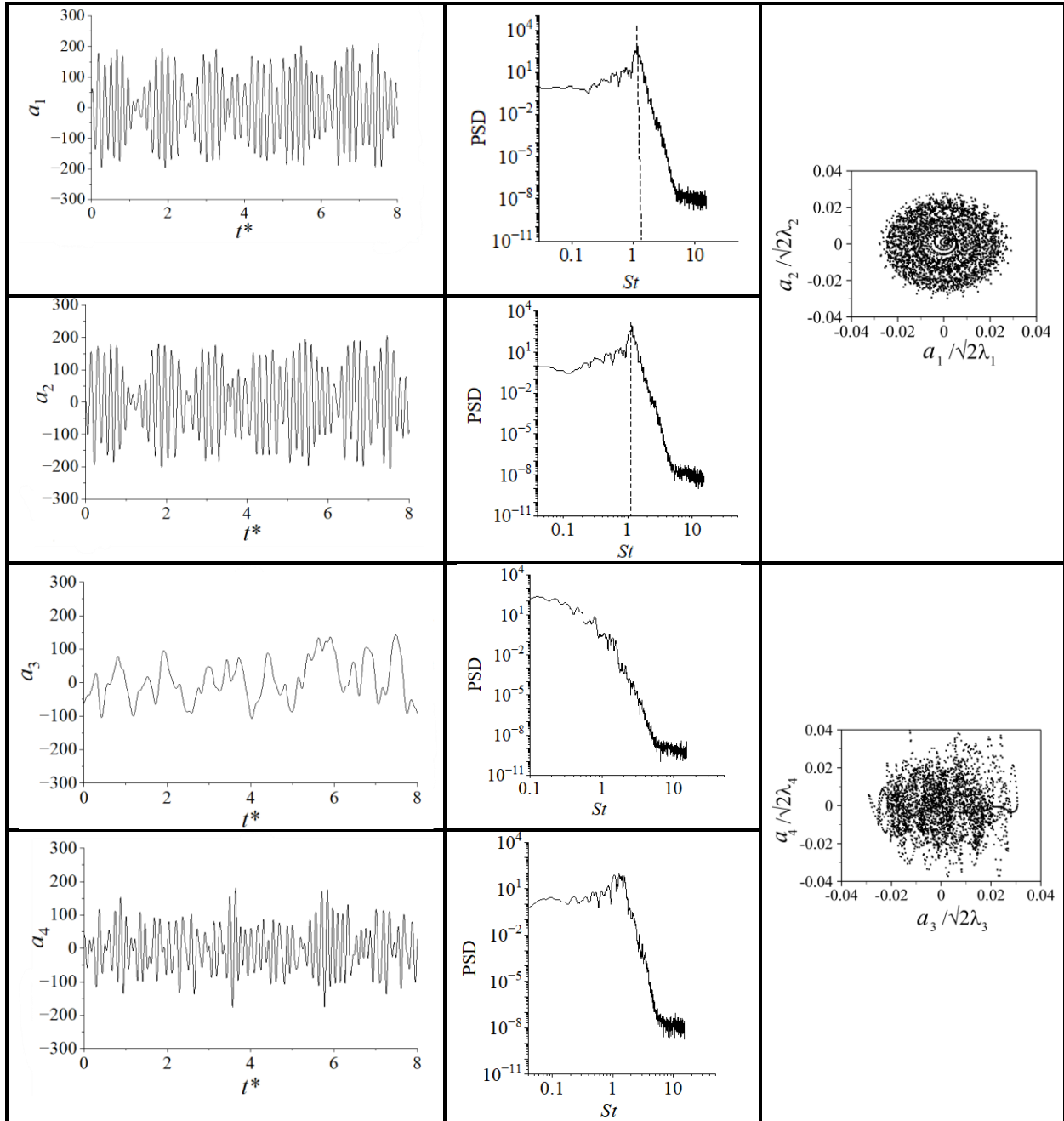


Figure 4.15. Time series history, frequency spectra and phase portrait of the temporal coefficients ($a_{ij}(t)$) $L_s = 140 \mu\text{m}$.

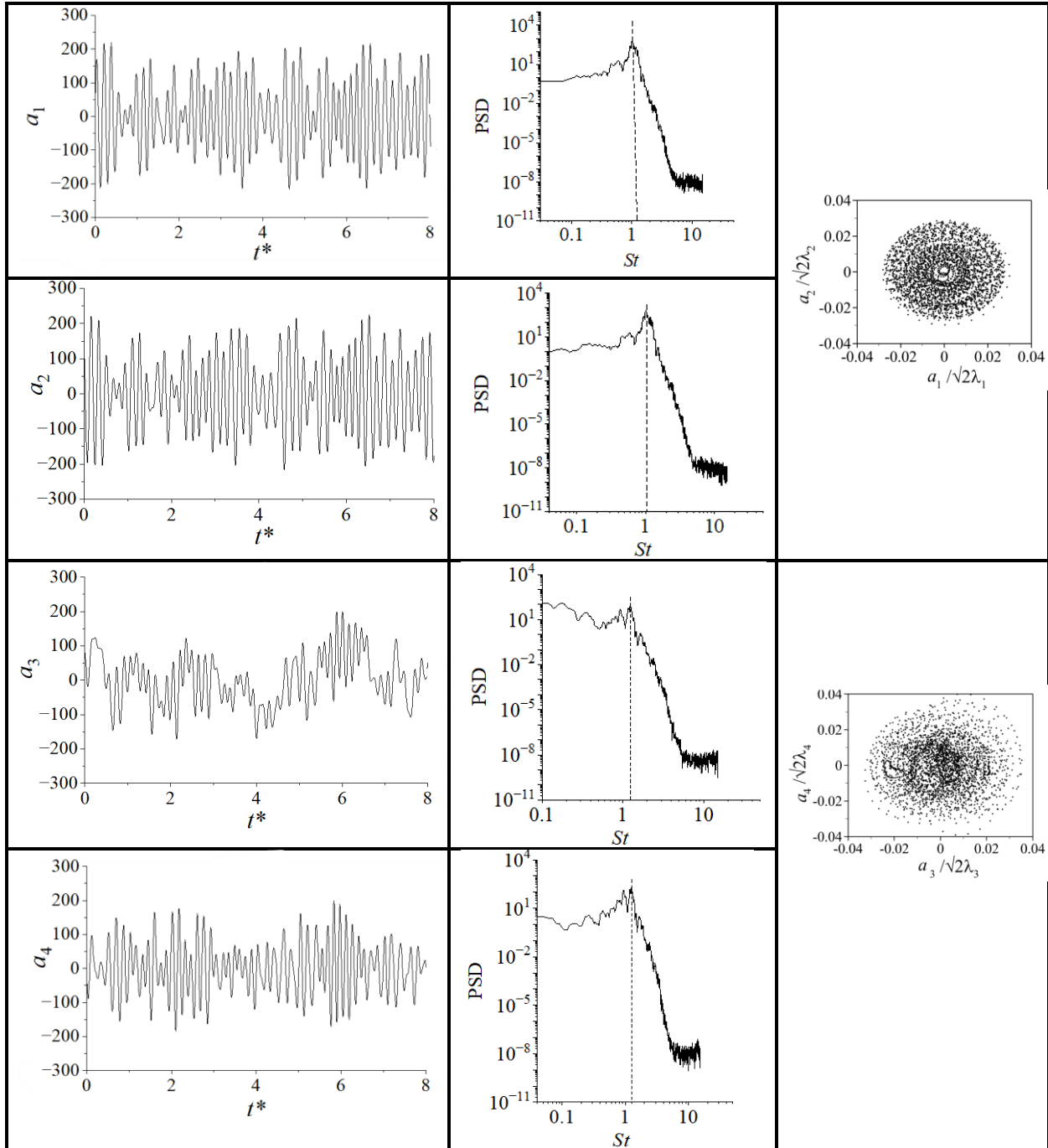


Figure 4.16. Time series history, frequency spectra and phase portrait of the temporal coefficients $(a_j(t))$ $L_s = 185 \mu\text{m}$.

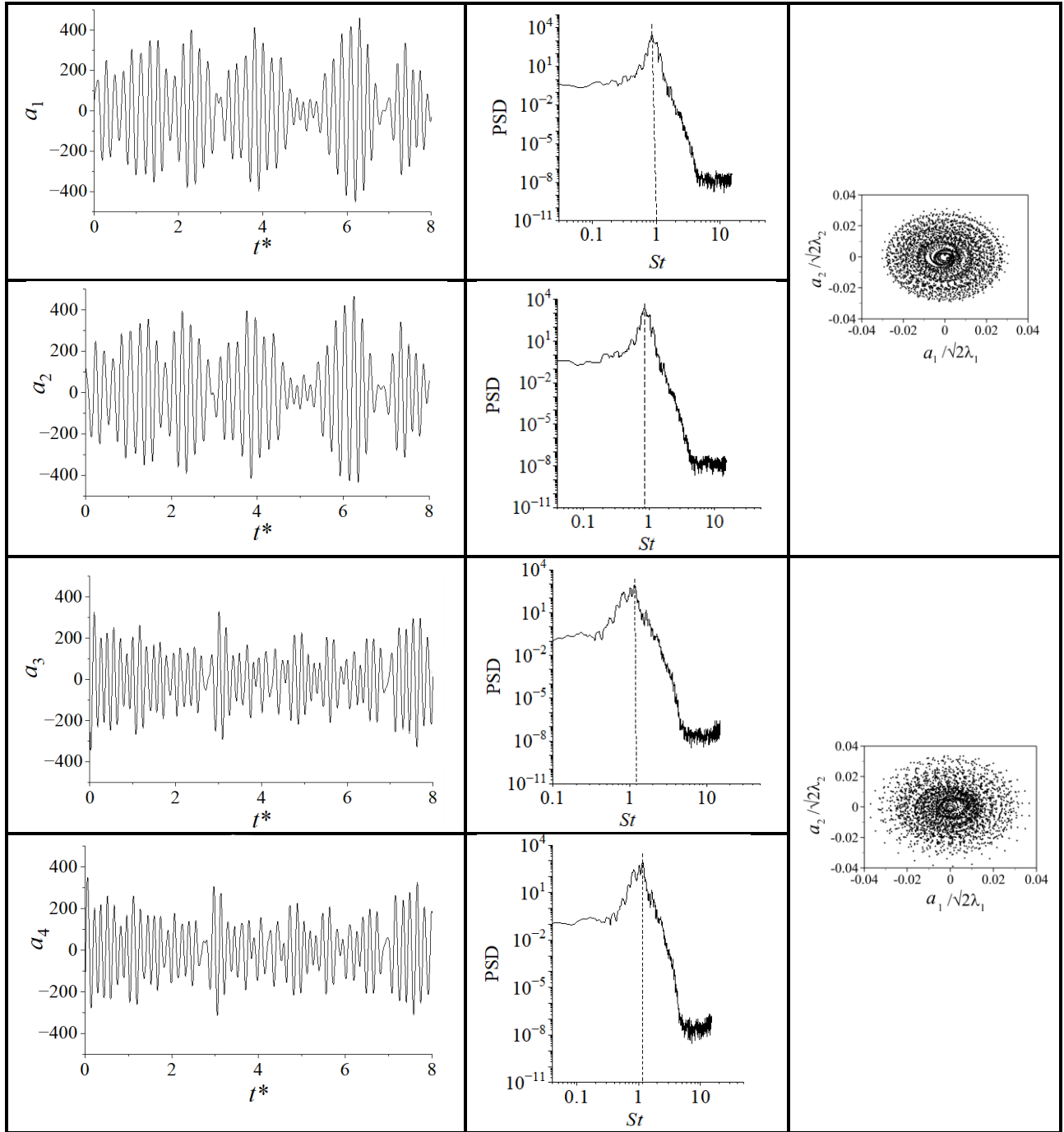


Figure 4.17. Time series history, frequency spectra and phase portrait of the temporal coefficients ($a_j(t)$) for $L_s = 400 \mu\text{m}$.

CHAPTER 5 CONCLUSIONS AND FUTURE WORK

This study provides a comprehensive numerical investigation of the effect of surface slip on turbulent flow dynamics around a NACA 64-618 airfoil at high Reynolds number ($Re = 1.3 \times 10^6$). The use of SHC, modeled using the Navier-slip boundary condition, was explored at varying slip lengths ($L_s = 100 \mu\text{m}$, $L_s = 140 \mu\text{m}$, $L_s = 185 \mu\text{m}$, $L_s = 400 \mu\text{m}$) to assess their impact on flow characteristics and unsteady vortex dynamics. A reference no-slip simulation was conducted on the airfoil under same flow conditions to facilitate comparison between the different flow configurations.

The instantaneous vorticity analysis revealed that in the baseline no-slip case, vortex roll-up was delayed. However, with the introduction of slip, the vortex roll-up occurred earlier, leading to a more rapid formation of vortices in the wake and enhanced flow acceleration. Also, the mean flow topology revealed distinct separation bubbles at the trailing edge in the baseline no-slip case. Regardless of the slip length considered, suppression of the separation bubble was observed, resulting in greater acceleration of the flow in the wake region. The centerline velocity profiles in the wake region further showed faster velocity recovery for the slip cases particularly for $L_s = 400 \mu\text{m}$ where the recovery reached $U/U_e \approx 1$ earlier, especially between $x/c = 1.06$ to $x/c = 1.28$. In the context to setting up offshore wind farms, such wake recovery can be a contributing factor in optimizing turbine spacing and improving overall farm efficiency.

The frequency spectra along the separated shear layer revealed the dominant shedding frequency migrated to lower St , particularly for $L_s = 400 \mu\text{m}$, indicating vortex pairing and fluid entrainment, which led to the formation of larger-scale convective structures in the POD modes. The POD analysis revealed that as the L_s increased, the fractional energy contribution from the first mode also increased. Specifically, the first mode contributed 9.9%, 11.3%, 13%, 11.8%, and

17% of the total energy for no-slip, $L_s = 100 \mu\text{m}$, $L_s = 140 \mu\text{m}$, $L_s = 185 \mu\text{m}$ and $L_s = 400 \mu\text{m}$ respectively. In all cases, the first two spatial patterns showed a strong mode pair, suggesting they shared similar energy content. However, in the baseline no-slip case, modes Φ_3'' and Φ_4'' failed to satisfy the criteria for mode pairing. The phase portrait was scattered and lacked a clear geometric structure, contrasting sharply with the coherent circular trajectory seen in the first two modes. A mode pair was observed for $L_s = 100 \mu\text{m}$ but at $L_s = 140 \mu\text{m}$, no such pairing was evident. The spatial patterns for $L_s = 400 \mu\text{m}$ evolved to an elongated train of irregular lobe shapes indicating the emergence of larger-scale convective structures likely driven by vortex pairing and strong fluid entrainment. Ultimately, these findings suggest that surface slip encourages the formation of more organized, large-scale convective structures, with larger slip lengths facilitating stronger vortex pairing and more coherent wake dynamics. In the context of OWT blades, where SHC are explored as a passive solution, this improved flow organization can help maintain aerodynamic performance and limit conditions that promote ice accumulation.

5.1 Recommendations for future studies

Although this study provided valuable insights into the effect of surface slip on unsteady vortex dynamics around a NACA 64-618 airfoil, several recommendations for future research can further enhance the understanding of flow physics in the presence of surface slip. These recommendations are summarized below:

- (i) Extend the current study to a 3D blade model to investigate the flow dynamics in the spanwise direction. This will help understand the interaction of vortices across the blade span and the overall impact of surface slip on the aerodynamic performance of rotating blades in practical applications.

- (ii) Implement turbulence models such as LES or DES to capture the detailed turbulence structures in the wake region. These models could provide a deeper understanding of the shear-layer instability and vortex interactions under surface slip conditions.

REFERENCES

1. Abbott, I. H., & Von Doenhoff, A. E. (2012). *Theory of wing sections: including a summary of airfoil data*. Courier Corporation.
2. Agyei-Agyemang, K. H., Essel, E. E., & Tachie, M. F. (2024). Effects of aspect ratio on flow characteristics on free surface-mounted rectangular cylinders. *International Journal of Heat and Fluid Flow*, *109*, 109535. <https://doi.org/https://doi.org/10.1016/j.ijheatfluidflow.2024.109535>
3. Antonini, C., Innocenti, M., Horn, T., Marengo, M., & Amirfazli, A. (2011). Understanding the effect of superhydrophobic coatings on energy reduction in anti-icing systems. *Cold Regions Science and Technology*, *67*(1), 58–67. <https://doi.org/https://doi.org/10.1016/j.coldregions.2011.02.006>
4. Arhin, E. J., Muzychka, Y., & Nyantekyi-Kwakye, B. (2024). Investigating the effect of deicing parameters using high-pressure water jet. *Cold Regions Science and Technology*, *226*, 104277. <https://doi.org/https://doi.org/10.1016/j.coldregions.2024.104277>
5. Arhin, J. E. (2023). *Experimental Investigation of Ice Cutting by High-Pressure Water Jet: Deicing on Marine Vessels*. Memorial University of Newfoundland.
6. Bakhtiari, E., Gharali, K., Chini, F., Al-Haq, A., & Nathwani, J. (2023). Slip influence on a blade performance under different pitch-oscillating motion. *Renewable and Sustainable Energy Reviews*, *188*, 113853. <https://doi.org/https://doi.org/10.1016/j.rser.2023.113853>
7. Bao, J., He, J., Chen, B., Yang, H., Jie, J., Wang, R., & Zhang, S. (2021). Multi-scale superhydrophobic anti-icing coating for wind turbine blades. *Energy Eng*, *118*, 947–959.
8. Battisti, L. (2011). Optimising wind turbine design for operation in cold climates. In *Wind energy systems* (pp. 388–460). Elsevier.
9. Battisti, L., Baggio, P., & Fedrizzi, R. (2006). Warm-Air Intermittent De-Icing System for Wind Turbines. *Wind Engineering*, *30*(5), 361–374. <https://doi.org/10.1260/030952406779502713>
10. Borgioli, F., Galvanetto, E., & Bacci, T. (2014). Influence of surface morphology and roughness on water wetting properties of low temperature nitrided austenitic stainless steels. *Materials Characterization*, *95*, 278–284. <https://doi.org/https://doi.org/10.1016/j.matchar.2014.07.006>

11. Bravo Jimenez, I. (2018). *Detection and removal of wind turbine ice: Method review and a CFD simulation test.*
12. Byun, D., Kim, J., Ko, H. S., & Park, H. C. (2008). Direct measurement of slip flows in superhydrophobic microchannels with transverse grooves. *Physics of Fluids*, *20*(11).
13. Cassie, A. B. D., & Baxter, S. (1944). Wettability of porous surfaces. *Transactions of Faraday Society*, *40*, 546–551.
14. Chi, H., Tong, G., Yang, S., Li, Y., Guo, W., & Feng, F. (2024). A de-icing experimental investigation of blade airfoil for wind turbines based on external hot air method. *Applied Thermal Engineering*, *241*, 122353. <https://doi.org/10.1016/j.applthermaleng.2024.122353>
15. Choi, C.-H., & Kim, C.-J. (2006). Large slip of aqueous liquid flow over a nanoengineered superhydrophobic surface. *Physical Review Letters*, *96*(6), 066001.
16. Choi, H., Lee, J., & Park, H. (2019). Wake structures behind a rotor with superhydrophobic-coated blades at low Reynolds number. *Physics of Fluids*, *31*(1).
17. Dalili, N., Edrisy, A., & Carriveau, R. (2009). A review of surface engineering issues critical to wind turbine performance. *Renewable and Sustainable Energy Reviews*, *13*(2), 428–438. <https://doi.org/10.1016/J.RSER.2007.11.009>
18. Daniello, R. J., Waterhouse, N. E., & Rothstein, J. P. (2009). Drag reduction in turbulent flows over superhydrophobic surfaces. *Physics of Fluids*, *21*(8).
19. Du, Y., Hu, L., Dong, L., Du, S., & Xu, D. (2023). Experimental study on anti-icing of robust TiO₂/polyurea superhydrophobic coating. *Coatings*, *13*(7), 1162.
20. Erdoğan, B. (2008). *Production and development of de-/anti icing fluids for aircraft.* Middle East Technical University.
21. Fakorede, O., Feger, Z., Ibrahim, H., Ilinca, A., Perron, J., & Masson, C. (2016). Ice protection systems for wind turbines in cold climate: characteristics, comparisons and analysis. *Renewable and Sustainable Energy Reviews*, *65*, 662–675. <https://doi.org/10.1016/j.rser.2016.06.080>
22. Feher, L., V. Nuss, & T Seitz. (2008). Microwave de-/anti-icing using the midas-technology. *Journal of Microwave Power and Electromagnetic Energy*, *43*(1), 56–59.

23. Fronk, B. M., Neal, R., & Srigrarimella, N. (2010). Evolution of the transition to a world driven by renewable energy. *Journal of Energy Resources Technology, Transactions of the ASME*, 132(2), 0210091–0210097. <https://doi.org/10.1115/1.4001574/451057>
24. Fu, P., & Farzaneh, M. (2010). A CFD approach for modeling the rime-ice accretion process on a horizontal-axis wind turbine. *Journal of Wind Engineering and Industrial Aerodynamics*, 98(4–5), 181–188.
25. Fu, X., Shen, Y., Zhu, W., He, Z., & Xiong, W. (2024). Introduction and State of the Art of Anti/De-icing Technologies. *Icephobic Materials for Anti/De-Icing Technologies*, 1–28.
26. Gantasala, S., Luneno, J.-C., & Aidanpaa, J.-O. (2016). Detection of ice mass based on the natural frequencies of wind turbine blade. *Wind Energy Science Discussions*, 2016, 1–17.
27. Gao, L., Liu, Y., Ma, L., & Hu, H. (2019). A hybrid strategy combining minimized leading-edge electric-heating and superhydrophobic surface coating for wind turbine icing mitigation. *Renewable Energy*, 140, 943–956. <https://doi.org/https://doi.org/10.1016/j.renene.2019.03.112>
28. Gao, T., Luo, Z. B., Zhou, Y., & Yang, S. K. (2021). A novel de-icing strategy combining electric-heating with plasma synthetic jet actuator. *Proceedings of the Institution of Mechanical Engineers, Part G: Journal of Aerospace Engineering*, 235(4), 513–522.
29. Gautam, S., Nyantekyi-Kwakye, B., & Pope, K. (2024). Turbulent flow around submerged foundation arrays for ocean energy. *Ocean Engineering*, 305, 117830. <https://doi.org/https://doi.org/10.1016/j.oceaneng.2024.117830>
30. Gedda Hans, Gedda Ida, & Widgren Mats. (2016). *Airborne de-icing solutions for wind turbines*. www.energiforsk.se
31. Getz, D., & Palacios, J. (2021). Design procedures and experimental verification of an electro-thermal deicing system for wind turbines. *Wind Energy Science*, 6(5), 1291–1309.
32. Gruncell, B. R. K., Sandham, N. D., & McHale, G. (2013). Simulations of laminar flow past a superhydrophobic sphere with drag reduction and separation delay. *Physics of Fluids*, 25(4).
33. Hansman Jr, R. J. (1982). *Microwave ice prevention system*. Google Patents.

34. Hasheminasab, S. M., Karimian, S. M. H., Noori, S., Saeedi, M., & Morton, C. (2021). Experimental investigation of the wake dynamics for a NACA0012 airfoil with a cut-in serrated trailing-edge. *Physics of Fluids*, 33(5).
35. Homola, M. C., Nicklasson, P. J., & Sundsbø, P. A. (2006). Ice sensors for wind turbines. *Cold Regions Science and Technology*, 46(2), 125–131.
36. Homola, M. C., Virk, M. S., Wallenius, T., Nicklasson, P. J., & Sundsbø, P. A. (2010). Effect of atmospheric temperature and droplet size variation on ice accretion of wind turbine blades. *Journal of Wind Engineering and Industrial Aerodynamics*, 98(12), 724–729.
37. Hossen, M. K., Asgari, E., Saeedi, M., & Nyantekyi-Kwakye, B. (2025). Flow characteristics of three-dimensional offset jet over surface-mounted ribs using large-eddy simulation. *Physics of Fluids*, 37(5).
38. Hu, Q., Yang, H., Jiang, X., Shu, L., & Yang, X. (2022). Investigation on one-step preparation and anti-icing experiments of robust super-hydrophobic surface on wind turbine blades. *Cold Regions Science and Technology*, 195, 103484. <https://doi.org/https://doi.org/10.1016/j.coldregions.2022.103484>
39. Huang, H., Liu, M., Gu, H., Li, X., Wu, X., & Sun, F. (2018). Effect of the slip length on the flow over a hydrophobic circular cylinder. *Fluid Dynamics Research*, 50(2), 025515.
40. Ilinca, A. (2011). Analysis and mitigation of icing effects on wind turbines. *Wind Turbines*, 4(4), 183–214.
41. IRENA, I. (2023). *World energy transitions outlook 2023: 1.5° C pathway*. International Renewable Energy Agency Abu Dhabi.
42. Israel, M. K., Dow, K., Clark, S. P., & Tachie, M. F. (2025). Spatiotemporal Characteristics of Turbulent Flows Around Partially Submerged Circular Cylinders. *Flow, Turbulence and Combustion*, 114(3), 995–1015.
43. Jasinski, W. J., Noe, S. C., Selig, M. S., & Bragg, M. B. (1998). Wind Turbine Performance Under Icing Conditions. *Journal of Solar Energy Engineering*, 120(1), 60–65. <https://doi.org/10.1115/1.2888048>
44. Jeffs, K., Maynes, D., & Webb, B. W. (2010). Prediction of turbulent channel flow with superhydrophobic walls consisting of micro-ribs and cavities oriented parallel to the flow direction. *International Journal of Heat and Mass Transfer*, 53(4), 786–796. <https://doi.org/https://doi.org/10.1016/j.ijheatmasstransfer.2009.09.033>

45. Jiang, G., Chen, L., Zhang, S., & Huang, H. (2018). Superhydrophobic SiC/CNTs Coatings with Photothermal Deicing and Passive Anti-Icing Properties. *ACS Applied Materials & Interfaces*, 10(42), 36505–36511. <https://doi.org/10.1021/acsami.8b11201>
46. Jonkman, J. (2009). Definition of a 5-MW Reference Wind Turbine for Offshore System Development. *National Renewable Energy Laboratory*.
47. Karmouch, R., & Ross, G. G. (2010). Superhydrophobic wind turbine blade surfaces obtained by a simple deposition of silica nanoparticles embedded in epoxy. *Applied Surface Science*, 257(3), 665–669. <https://doi.org/https://doi.org/10.1016/j.apsusc.2010.07.041>
48. Kim, N., Kim, H., & Park, H. (2015). An experimental study on the effects of rough hydrophobic surfaces on the flow around a circular cylinder. *Physics of Fluids*, 27(8).
49. Kim, P., Wong, T.-S., Alvarenga, J., Kreder, M. J., Adorno-Martinez, W. E., & Aizenberg, J. (2012). Liquid-Infused Nanostructured Surfaces with Extreme Anti-Ice and Anti-Frost Performance. *ACS Nano*, 6(8), 6569–6577. <https://doi.org/10.1021/nn302310q>
50. Kraj, A. G., & Bibeau, E. L. (2010). Phases of icing on wind turbine blades characterized by ice accumulation. *Renewable Energy*, 35(5), 966–972. <https://doi.org/https://doi.org/10.1016/j.renene.2009.09.013>
51. Kumahor, S., & Tachie, M. F. (2023). Effects of streamwise aspect ratio on the spatio-temporal characteristics of flow around rectangular cylinders. *International Journal of Heat and Fluid Flow*, 101, 109133. <https://doi.org/https://doi.org/10.1016/j.ijheatfluidflow.2023.109133>
52. Laakso, T., Baring-Gould, I., Durstewitz, M., Horbaty, R., Lacroix, A., Peltola, E., Ronsten, G., Tallhaug, L., & Wallenius, T. (2010). State-of-The-art of wind energy in cold climates. *English*, 152.
53. Lamraoui, F., Fortin, G., Benoit, R., Perron, J., & Masson, C. (2014). *Atmospheric icing impact on wind turbine production*. <https://doi.org/10.1016/j.coldregions.2013.12.008>
54. Lathe, S. S., Sutar, R. S., Bhosale, A. K., Nagappan, S., Ha, C.-S., Sadasivuni, K. K., Liu, S., & Xing, R. (2019). Recent developments in air-trapped superhydrophobic and liquid-infused slippery surfaces for anti-icing application. *Progress in Organic Coatings*, 137, 105373. <https://doi.org/https://doi.org/10.1016/j.porgcoat.2019.105373>

55. Lee, C., Choi, C.-H., & Kim, C.-J. “CJ.” (2008). Structured surfaces for a giant liquid slip. *Physical Review Letters*, *101*(6), 064501.
56. Lee, C., & Kim, C.-J. “CJ.” (2009). Maximizing the giant liquid slip on superhydrophobic microstructures by nanostructuring their sidewalls. *Langmuir*, *25*(21), 12812–12818.
57. Lee, J., Kim, H., & Park, H. (2018). Effects of superhydrophobic surfaces on the flow around an NACA0012 hydrofoil at low Reynolds numbers. *Experiments in Fluids*, *59*, 1–18.
58. Legendre, D., Lauga, E., & Magnaudet, J. (2009). Influence of slip on the dynamics of two-dimensional wakes. *Journal of Fluid Mechanics*, *633*, 437–447.
59. Lehtomäki, V., Rissanen, S., Wadham-Gagnon, M., Sandel, K., Moser, W., & Jacob, D. (2016). Fatigue loads of iced turbines: Two case studies. *Journal of Wind Engineering and Industrial Aerodynamics*, *158*, 37–50. <https://doi.org/10.1016/j.jweia.2016.09.002>
60. Lei, S., Wang, F., Fang, X., Ou, J., & Li, W. (2019). Icing behavior of water droplets impinging on cold superhydrophobic surface. *Surface and Coatings Technology*, *363*, 362–368. <https://doi.org/10.1016/j.surfcoat.2019.02.035>
61. Li, B., He, L., Liu, Y., Luo, J., & Zhang, G. (2019). Influences of key factors in hot-air deicing for live substation equipment. *Cold Regions Science and Technology*, *160*, 89–96.
62. Li, C., Qiu, H., Ma, J., & Wang, Y. (2023). Numerical study on the performance of mixed flow blood pump with superhydrophobic surface. *Medical & Biological Engineering & Computing*, *61*(11), 3103–3121.
63. Li, H., Hu, Q., Jiang, X., Yu, Z., Shu, L., Li, C., & Qiu, Z. (2022). Review on Anti-icing and De-icing Techniques of Wind Turbine Blades. *System*, *14*, 15.
64. Li, W., Zhan, Y., & Yu, S. (2021). Applications of superhydrophobic coatings in anti-icing: Theory, mechanisms, impact factors, challenges and perspectives. *Progress in Organic Coatings*, *152*, 106117. <https://doi.org/10.1016/j.porgcoat.2020.106117>
65. Li, X., Chi, H., Li, Y., Xu, Z., Guo, W., & Feng, F. (2024). An Experimental Study on Blade Surface De-Icing Characteristics for Wind Turbines in Rime Ice Condition by Electro-Thermal Heating. *Coatings*, *14*(1), 94.

66. Li, X., Li, X., Mu, Z., Li, Y., & Feng, F. (2023). An Experimental Study on Biochar/Polypyrrole Coating for Blade Anti-Icing of Wind Turbines. *Coatings*, 13(4). <https://doi.org/10.3390/coatings13040759>
67. Liu, B., Liu, Z., Li, Y., & Feng, F. (2023). A Wind Tunnel Test of the Anti-Icing Properties of MoS₂/ZnO Hydrophobic Nano-Coatings for Wind Turbine Blades. *Coatings*, 13(4), 686.
68. Lumley, J. L. (1967). Similarity and the turbulent energy spectrum. *The Physics of Fluids*, 10(4), 855–858.
69. Madi, E., Pope, K., Huang, W., & Iqbal, T. (2019). A review of integrating ice detection and mitigation for wind turbine blades. *Renewable and Sustainable Energy Reviews*, 103, 269–281. <https://doi.org/https://doi.org/10.1016/j.rser.2018.12.019>
70. Maissan, J. F. (2001). Wind power development in sub-arctic conditions with severe rime icing. *Northern Review*, 24.
71. Mayer, C., Ilinca, A., Fortin, G., & Perron, J. (2007). Wind tunnel study of electro-thermal de-icing of wind turbine blades. *International Journal of Offshore and Polar Engineering*, 17(03).
72. Menter, F. (1993). Zonal two equation kw turbulence models for aerodynamic flows. *23rd Fluid Dynamics, Plasmadynamics, and Lasers Conference*, 2906.
73. Min, T., & Kim, J. (2004). Effects of hydrophobic surface on skin-friction drag. *Physics of Fluids*, 16(7), L55–L58.
74. Mokhatab, S. (2007). Energy: Technology and Directions for the Future. *Journal of Energy Resources Technology*, 129(1), 79–79. <https://doi.org/10.1115/1.2424966>
75. Moore, D. M., Letchford, C. W., & Amitay, M. (2019). Energetic scales in a bluff body shear layer. *Journal of Fluid Mechanics*, 875, 543–575.
76. Najafi, E., Nejat, A., & Chini, S. F. (2017). Effect of superhydrophobic surface on drag coefficient of SD7003 foil: a numerical approach. *Modares Mechanical Engineering*, 17(2), 126–134.
77. Nine, M. J., Chizhova, A., Maher, S., Tripathy, A., Mazinani, A., Dadkhah, M., Hassan, K., Yap, P. L., Tung, T. T., & Losic, D. (2023). Ice-fouling on superhydrophobic and slippery surfaces textured by 3D printing: revealing key limiting factors. *Surfaces and Interfaces*, 40, 103005. <https://doi.org/https://doi.org/10.1016/j.surfin.2023.103005>

78. Nouri, N. M., Bakhsh, M. S., & Sekhavat, S. (2013). Analysis of shear rate effects on drag reduction in turbulent channel flow with superhydrophobic wall. *Journal of Hydrodynamics*, Ser. B, 25(6), 944–953. [https://doi.org/https://doi.org/10.1016/S1001-6058\(13\)60444-8](https://doi.org/https://doi.org/10.1016/S1001-6058(13)60444-8)
79. Nyantekyi-Kwakye, B., Tachie, M. F., & Clark, S. P. (2016). Flow characteristics of an offset jet over a surface mounted square rib. *Journal of Turbulence*, 17(8), 727–757.
80. Oberli, L., Caruso, D., Hall, C., Fabretto, M., Murphy, P. J., & Evans, D. (2014). Condensation and freezing of droplets on superhydrophobic surfaces. *Advances in Colloid and Interface Science*, 210, 47–57. <https://doi.org/https://doi.org/10.1016/j.cis.2013.10.018>
81. Ou, J., Perot, B., & Rothstein, J. P. (2004). Laminar drag reduction in microchannels using ultrahydrophobic surfaces. *Physics of Fluids*, 16(12), 4635–4643.
82. Parent, O., & Ilinca, A. (2011). Anti-icing and de-icing techniques for wind turbines: Critical review. *Cold Regions Science and Technology*, 65(1), 88–96. <https://doi.org/https://doi.org/10.1016/j.coldregions.2010.01.005>
83. Park, H., Choi, C.-H., & Kim, C.-J. (2021). Superhydrophobic drag reduction in turbulent flows: A critical review. *Experiments in Fluids*, 62, 1–29.
84. Park, H., Park, H., & Kim, J. (2013). A numerical study of the effects of superhydrophobic surface on skin-friction drag in turbulent channel flow. *Physics of Fluids*, 25(11).
85. Peng, C., Xing, S., Yuan, Z., Xiao, J., Wang, C., & Zeng, J. (2012). Preparation and anti-icing of superhydrophobic PVDF coating on a wind turbine blade. *Applied Surface Science*, 259, 764–768. <https://doi.org/https://doi.org/10.1016/j.apsusc.2012.07.118>
86. Peter Suke, B. (2014). *Analysis of heating systems to mitigate ice accretion on wind turbine blades*.
87. Petrenko, V. (2006). *Methods for modifying friction between an object and ice or snow*. Google Patents.
88. Pope, S. B. (2001). Turbulent flows. *Measurement Science and Technology*, 12(11), 2020–2021.
89. Pourbagian, M., & Habashi, W. G. (2024). Numerical Optimization of Electrothermal Anti-icing and De-icing Systems via Reduced Order Models. In W. G. Habashi (Ed.), *Handbook of Numerical Simulation of In-Flight Icing* (pp. 1159–1211). Springer International Publishing. https://doi.org/10.1007/978-3-031-33845-8_17

90. Press, E., Popkostova, Y., Van de Graaf, T., Rath, E., & Tagoe, G. (2024). *Geopolitics of the energy transition: Energy security*.
91. Qiu, G. (2018). Electro-thermal de-icing process and its numerical simulation of wind turbine. *Chongqing University*.
92. Quayson-Sackey, E., Nyantekyi-Kwakye, B., & Ayetor, G. K. (2024). Technological advancements for anti-icing and de-icing offshore wind turbine blades. *Cold Regions Science and Technology*, 104400.
93. Quéré, D., & Reyssat, M. (2008). Non-adhesive lotus and other hydrophobic materials. *Philosophical Transactions of the Royal Society A: Mathematical, Physical and Engineering Sciences*, 366(1870), 1539–1556.
94. Rastan, M. R., Foshat, S., & Sekhavat, S. (2019). High-reynolds number flow around coated symmetrical hydrofoil: effect of streamwise slip on drag force and vortex structures. *Journal of Marine Science and Technology*, 24, 500–511.
95. Rekuviene, R., Saeidiharzand, S., Mažeika, L., Samaitis, V., Jankauskas, A., Sadaghiani, A. K., Gharib, G., Munganlı, Z., & Koşar, A. (2024). A review on passive and active anti-icing and de-icing technologies. In *Applied Thermal Engineering* (Vol. 250). Elsevier Ltd. <https://doi.org/10.1016/j.applthermaleng.2024.123474>
96. Riches, G., Martinuzzi, R., & Morton, C. (2018). Proper orthogonal decomposition analysis of a circular cylinder undergoing vortex-induced vibrations. *Physics of Fluids*, 30(10).
97. Rindeskär, E. (2010). *Modelling of icing for wind farms in cold climate: A comparison between measured and modelled data for reproducing and predicting ice accretion*.
98. Romani, G., van der Velden, W. C., & Casalino, D. (2018). Deterministic and statistical analysis of trailing-edge noise mechanisms with and without serrations. *2018 AIAA/CEAS Aeroacoustics Conference*, 3129.
99. Rowin, W. A., & Ghaemi, S. (2019). Streamwise and spanwise slip over a superhydrophobic surface. *Journal of Fluid Mechanics*, 870, 1127–1157.
100. Ruan, M., Li, W., Wang, B., Deng, B., Ma, F., & Yu, Z. (2013). Preparation and anti-icing behavior of superhydrophobic surfaces on aluminum alloy substrates. *Langmuir*, 29(27), 8482–8491.
101. Ryerson, C. C. (2009). *Assessment of superstructure ice protection as applied to offshore oil operations safety*.

102. Ryerson, C. C. (2011). Ice protection of offshore platforms. *Cold Regions Science and Technology*, 65(1), 97–110.
103. Ryerson, C. C. (2013). *Icing Management for Coast Guard Assets*. <https://apps.dtic.mil/sti/citations/ADA583017>
104. Rykaczewski, K., Anand, S., Subramanyam, S. B., & Varanasi, K. K. (2013). Mechanism of Frost Formation on Lubricant-Impregnated Surfaces. *Langmuir*, 29(17), 5230–5238. <https://doi.org/10.1021/la400801s>
105. Sabatier, J., Lanusse, P., Feytout, B., & Gracia, S. (2016). CRONE control based anti-icing/deicing system for wind turbine blades. *Control Engineering Practice*, 56, 200–209.
106. Saeedi, M., LePoudre, P. P., & Wang, B.-C. (2014). Direct numerical simulation of turbulent wake behind a surface-mounted square cylinder. *Journal of Fluids and Structures*, 51, 20–39. <https://doi.org/https://doi.org/10.1016/j.jfluidstructs.2014.06.021>
107. Saeedi, M., Nyantekyi-Kwakye, B., & Asgari, E. (2024). Energy and frequency analysis in the wake of a heavy-duty truck model using large-eddy simulation. *Journal of Wind Engineering and Industrial Aerodynamics*, 253, 105854. <https://doi.org/https://doi.org/10.1016/j.jweia.2024.105854>
108. Seifert, H. (2005). Technical requirements for rotor blades operating in cold climate. *DEWI-Magazin*.
109. Shahsavari, A., Nejat, A., Climent, E., & Chini, S. F. (2023). Unexpected trends of lift for hydrofoils with superhydrophobic coating. *European Journal of Mechanics - B/Fluids*, 101, 219–226. <https://doi.org/https://doi.org/10.1016/j.euromechflu.2023.05.004>
110. Shajiee, S., Pao, L. Y., Wagner, P. N., Moore, E. D., & McLeod, R. R. (2013). Direct ice sensing and localized closed-loop heating for active de-icing of wind turbine blades. *2013 American Control Conference*, 634–639.
111. Shirtcliffe, N. J., McHale, G., Atherton, S., & Newton, M. I. (2010). An introduction to superhydrophobicity. *Advances in Colloid and Interface Science*, 161(1–2), 124–138.
112. Shohag, M. A. S., Hammel, E. C., Olawale, D. O., & Okoli, O. I. (2017). Damage mitigation techniques in wind turbine blades: A review. *Wind Engineering*, 41(3), 185–210.
113. Shu, L., Qi, J., & Hu, Q. (2017). Anti-icing model and sectionalized anti-icing method by electrical heating for wind turbine blades. *Proc. CSEE*, 37(5), 1448–1455.

114. Sirovich, L. (1987). Turbulence and the dynamics of coherent structure. part i, ii, iii. *Quat. Appl. Math.*, 3, 583.
115. Sooraj, P., Jain, S., & Agrawal, A. (2019). Flow over hydrofoils with varying hydrophobicity. *Experimental Thermal and Fluid Science*, 102, 479–492.
116. Sooraj, P., Ramagya, M. S., Khan, M. H., Sharma, A., & Agrawal, A. (2020). Effect of superhydrophobicity on the flow past a circular cylinder in various flow regimes. *Journal of Fluid Mechanics*, 897, A21.
117. Sotoude Haghghi, M. H., Mirghavami, S. M., Ghorani, M. M., Riasi, A., & Chini, S. F. (2020). A numerical study on the performance of a superhydrophobic coated very low head (VLH) axial hydraulic turbine using entropy generation method. *Renewable Energy*, 147, 409–422. <https://doi.org/https://doi.org/10.1016/j.renene.2019.09.003>
118. Strobl, T., Storm, S., & Ameduri, S. (2018). Synergic effects of passive and active ice protection systems. In *Morphing Wing Technologies* (pp. 841–864). Elsevier.
119. Subramanyam, S. B., Rykaczewski, K., & Varanasi, K. K. (2013). Ice Adhesion on Lubricant-Impregnated Textured Surfaces. *Langmuir*, 29(44), 13414–13418. <https://doi.org/10.1021/la402456c>
120. Sunden, B., & Wu, Z. (2015). On Icing and Icing Mitigation of Wind Turbine Blades in Cold Climate. *Journal of Energy Resources Technology*, 137(5). <https://doi.org/10.1115/1.4030352>
121. Thomas, S. K., Cassoni, R. P., & MacArthur, C. D. (1996). Aircraft anti-icing and de-icing techniques and modeling. *Journal of Aircraft*, 33(5), 841–854.
122. Wang, K., Yang, L., Yu, Y., & Hou, G. (2018). Influence of slip boundary on the hydrofoil with a curved slip boundary condition for the lattice Boltzmann method. *Physics of Fluids*, 30(12).
123. Wang, T., Zheng, Y., Raji, A.-R. O., Li, Y., Sikkema, W. K. A., & Tour, J. M. (2016). Passive anti-icing and active deicing films. *ACS Applied Materials & Interfaces*, 8(22), 14169–14173.
124. Wang, Z.-J., Kwon, D.-J., Lawrence DeVries, K., & Park, J.-M. (2015). Frost formation and anti-icing performance of a hydrophobic coating on aluminum. *Experimental Thermal and Fluid Science*, 60, 132–137. <https://doi.org/https://doi.org/10.1016/j.expthermflusci.2014.09.003>

125. Wei, K., Yang, Y., Zuo, H., & Zhong, D. (2020). A review on ice detection technology and ice elimination technology for wind turbine. *Wind Energy*, 23(3), 433–457. <https://doi.org/https://doi.org/10.1002/we.2427>
126. Weis, T., & Maissan, J. (2003). *The effects of black blades on surface temperatures for wind turbines*. <https://doi.org/https://doi.org/>
127. Wenzel, R. N. (1936). Resistance of solid surfaces to wetting by water. *Industrial & Engineering Chemistry*, 28(8), 988–994.
128. Xie, T., Dong, J., Chen, H., Jiang, Y., & Yao, Y. (2016). Experimental investigation of deicing characteristics using hot air as heat source. *Applied Thermal Engineering*, 107, 681–688.
129. Xie, Z., Wang, H., Geng, Y., Li, M., Deng, Q., Tian, Y., Chen, R., Zhu, X., & Liao, Q. (2021). Carbon-based photothermal superhydrophobic materials with hierarchical structure enhances the anti-icing and photothermal deicing properties. *ACS Applied Materials & Interfaces*, 13(40), 48308–48321.
130. Xu, K., Hu, J., Jiang, X., Meng, W., Lan, B., & Shu, L. (2018). Anti-Icing performance of hydrophobic silicone–acrylate resin coatings on wind blades. *Coatings*, 8(4), 151.
131. Yang, X., Bai, X., & Cao, H. (2022). Influence analysis of rime icing on aerodynamic performance and output power of offshore floating wind turbine. *Ocean Engineering*, 258, 111725. <https://doi.org/10.1016/J.OCEANENG.2022.111725>
132. Yin, L., Zhu, L., Wang, Q., Ding, J., & Chen, Q. (2011). Superhydrophobicity of Natural and Artificial Surfaces under Controlled Condensation Conditions. *ACS Applied Materials & Interfaces*, 3(4), 1254–1260. <https://doi.org/10.1021/am200061t>
133. You, D., & Moin, P. (2007). Effects of hydrophobic surfaces on the drag and lift of a circular cylinder. *Physics of Fluids*, 19(8).
134. Young, T. (1805). III. An essay on the cohesion of fluids. *Philosophical Transactions of the Royal Society of London*, 95, 65–87. <https://doi.org/10.1098/rstl.1805.0005>
135. Zhang, Y., Guo, W., Li, Y., Chi, H., Zhao, P., & Tagawa, K. (2023). An experimental study of icing distribution on a symmetrical airfoil for wind turbine blade in the offshore environmental condition. *Ocean Engineering*, 273. <https://doi.org/10.1016/j.oceaneng.2023.113960>
136. Zhang, Z., Wang, J., Ling, J., & Yuan, Y. (2018). A metamaterial absorber for microwave de-icing of wind turbine blades and its electromagnetic and thermal properties. *Proceedings of the Second International Conference on Materials Chemistry and Environmental Protection (MEEP 2018), Sanya City, China*, 23–25.

137. Zhu, M., Huang, W., Ma, L., & Luo, J. (2024). Influence of surface slip on hydrodynamics and flow field around a two-dimensional hydrofoil at a moderate Reynolds number. *Physics of Fluids*, 36(5).
138. Zhu, T., Cheng, Y., Huang, J., Xiong, J., Ge, M., Mao, J., Liu, Z., Dong, X., Chen, Z., & Lai, Y. (2020). A transparent superhydrophobic coating with mechanochemical robustness for anti-icing, photocatalysis and self-cleaning. *Chemical Engineering Journal*, 399, 125746. <https://doi.org/10.1016/j.cej.2020.125746>

APPENDIX A: AIRFOIL COORDINATES

#group	#point	#x	#y	#z
1	1	1000	0	0
1	2	950.56	13.44	0
1	3	901.15	26.46	0
1	4	851.61	39.63	0
1	5	801.91	52.7	0
1	6	752.03	65.44	0
1	7	701.96	77.54	0
1	8	651.71	88.7	0
1	9	601.29	98.7	0
1	10	550.71	107.3	0
1	11	500	114.23	0
1	12	449.17	119.15	0
1	13	398.27	121.63	0
1	14	347.35	120.65	0
1	15	296.45	116.98	0
1	16	245.6	110.65	0
1	17	194.86	101.53	0
1	18	144.27	89.37	0
1	19	93.95	73.22	0
1	20	68.95	63.12	0
1	21	44.17	50.93	0
1	22	19.82	35.18	0
1	23	8.05	24.52	0
1	24	3.59	18.85	0
1	25	1.5	15.34	0
1	26	0	0	0
1	27	8.5	-12.34	0
1	28	11.41	-14.65	0
1	29	16.95	-18.1	0
1	30	30.18	-24.02	0
1	31	55.83	-31.97	0
1	32	81.05	-37.69	0
1	33	106.05	-42.2	0
1	34	155.73	-48.99	0
1	35	205.14	-53.77	0
1	36	254.4	-56.95	0
1	37	303.55	-58.66	0
1	38	352.65	-58.85	0
1	39	401.73	-57.37	0
1	40	450.83	-53.45	0

#group	#point	#x	#y	#z
1	41	500	-48.05	0
1	42	549.29	-41.6	0
1	43	598.71	-34.44	0
1	44	648.29	-26.9	0
1	45	698.04	-19.22	0
1	46	747.97	-11.74	0
1	47	798.09	-4.94	0
1	48	848.39	0.75	0
1	49	898.85	4.56	0
1	50	949.44	5.52	0
1	0			

APPENDIX B: SLIP UDF CODE

```
#include "udf.h"
#include "sg_mem.h"
#include "dynamesh_tools.h"
#include "f_wall.h"
#include "mem.h"
#include "sg.h" /* needed for the secondary gradient source macro */

//-----
-----
DEFINE_PROFILE(Wall_slip_velocity_x,face_thread,i)
// x velocity
{
face_t f;
cell_t neig;
Thread *cell_thread;
Domain *domain = Get_Domain(1);
real slip_length = 0.0001;
real R=0.1;
real NV_VEC(A);
real normal_magnitude, velocity_differential_x, x_vector_mag, velocity_differential_y,
velocity_mag, n1, n2;

// Defining cell thread.....
cell_thread=THREAD_T0(face_thread);

// Defining slip velocity for wall.....
begin_f_loop(f,face_thread)
{
neig=F_C0(f,face_thread);
F_AREA(A,f,face_thread);
velocity_mag= pow(pow(F_U(f, face_thread), 2) + pow(F_V(f, face_thread), 2), 0.5);
normal_magnitude=pow(pow(A[0],2)+pow(A[1],2),0.5);
n1 = A[0] / normal_magnitude;
n2 = A[1] / normal_magnitude;
F_PROFILE(f,face_thread,i)=(1-R)*F_U(f, face_thread) +R*slip_length*n2*(2*n1*n2*(-
C_DUDX(neig, cell_thread)+C_DVDY(neig, cell_thread))+((pow(n1,2)-
pow(n2,2)))*(C_DUDY(neig, cell_thread)+C_DVDX(neig, cell_thread)));
}
}
```

```

end_f_loop(f,face_thread)
}

//-----
-----
DEFINE_PROFILE(Wall_slip_velocity_y,face_thread,i)
// y velocity
{
    face_t f;
    cell_t neig;
    Thread *cell_thread;
    Domain *domain = Get_Domain(1);
    real slip_length = 0.0001;
    real R=0.1;
    real NV_VEC(A);
    real normal_magnitude, velocity_differential_x, y_vector_mag, velocity_differential_y,
    velocity_mag, n1, n2;

    // Defining cell thread.....
    cell_thread = THREAD_T0(face_thread);

    // Defining slip velocity for
    wall.....
    begin_f_loop(f, face_thread)
    {
        neig = F_C0(f, face_thread);
        F_AREA(A, f, face_thread);
        velocity_mag= pow(pow(F_U(f, face_thread), 2) + pow(F_V(f, face_thread), 2), 0.5);
        normal_magnitude = pow(pow(A[0], 2) + pow(A[1], 2), 0.5);
        n1 = A[0] / normal_magnitude;
        n2 = A[1] / normal_magnitude;
        F_PROFILE(f,face_thread,i)=(1-R)*F_V(f, face_thread)-R*slip_length*n1*(2*n1*n2*(-
        C_DUDX(neig, cell_thread)+C_DVDY(neig, cell_thread))+((pow(n1,2)-
        pow(n2,2)))*(C_DUDY(neig, cell_thread)+C_DVDX(neig, cell_thread)));
        //F_PROFILE(f,face_thread,i)=(1-R)*F_V(f, face_thread)+R*slip_length*n1;
    }
    end_f_loop(f, face_thread)
}

```